QUANTUM MECHANICS AND EXPERIMENTAL SOLID-STATE NUCLEAR MAGNETIC RESONANCE ANALYSIS OF STRAINED MOLECULAR SYSTEMS

by

Merrill David Halling

A dissertation submitted to the faculty of
The University of Utah
in partial fulfillment of the requirements for the degree of

Doctor of Philosophy

Department of Chemistry

The University of Utah

December 2011

The University of Utah Graduate School

STATEMENT OF DISSERTATION APPROVAL

The dissertation of **Merrill David Halling**

has been approved by the following supervisory committee members:

Ronald J. Pugmire	, Chair	**7/14/2011** Date Approved
Michael H. Bartl	, Member	**7/14/2011** Date Approved
Peter F. Flynn	, Member	**7/14/2011** Date Approved
Edward M. Eyring	, Member	**7/14/2011** Date Approved
Brian Saam	, Member	**7/14/2011** Date Approved

and by **Henry S. White** , Chair of the Department of **Chemistry**

and by Charles A. Wight, Dean of The Graduate School.

ABSTRACT

In this work ^{13}C solid-state NMR and quantum mechanical studies of strained molecular systems are discussed. The chemical shift tensor values reported in this document were obtained using the FIREMAT method. Theoretical analyses of chemical shielding tensors were performed through the computer nodes operated by the Utah Center for High Performance Computing. Analyses were performed on sumanene, indenofluoranthene, tetrathiafulvalene, tetrathiafulvalene dimer, [2,2]paracyclophane, and 1,8-dioxa[8](2,7)pyrenophane.

The FIREMAT data were fit using the TIGER data processing technique. TIGER provides a means to fit the FIREMAT data, accommodating its unique phase and relaxation characteristics. The details of the FIREMAT experiment are discussed in Chapter 1. The experimentally obtained chemical shift data were compared with calculated chemical shielding data. For these molecular systems, density functional theory was used along with the B3LYP exchange and correlation functionals. Multiple basis sets were used and relatively low errors are reported, between 2.0 ppm and 4.2 ppm. The errors reflect the difference between experimental and theoretical results. The relatively small errors are consistent with those of other polycyclic aromatic hydrocarbons (PAHs) and similar molecular systems. Chapter 2 discusses the three-dimensional aspect of tensor error analysis and how it is used in determining the errors associated with comparing two chemical shift tensors, i.e., theoretically derived and

experimentally determined tensors. All error values reported and discussed in this dissertation are determined using this error analysis method.

Molecular conformation may be explored by variation in chemical shift tensor principal values. The ring strain in curved polycyclic aromatic hydrocarbons can be associated with downfield shifts in the δ_{33} component of the chemical shift tensor. This is discussed in Chapters 3 and 5, as it relates to sumanene, indenofluoranthene, [2,2]paracyclophane, 1,8-dioxa[8](2,7)pyrenophane and how they compare to C_{60}. Theoretical energy and NMR calculations, when compared with experimental solid-state NMR data, may also be used to refine X-ray crystal structures. This is useful in predicting the location of Hydrogen atoms in X-ray structures. Long bonding interactions are discussed in Chapter 4 regarding TTF and $[TTF]_2^{2+}$ dimers.

TABLE OF CONTENTS

ABSTRACT……...iii

LIST OF TABLES…….……vii

LIST OF FIGURES……...……..ix

ACKNOWLEDGMENTS……..… xii

Chapter

1. INTRODUCTION……1

Chemical Shift Tensors……..…..1
Five π-Replicated Magic Angle Turning Experiment…… 6
Theoretical NMR Calculations……..…… 13

2. THE USE OF METRIC SPACES IN NMR CRYSTALLOGRAPHY…..…..…...16

Introduction……16
The Chemical Shift Tensor Discussion…….....18
Examples of Metrics for Chemical-Shift Representations with Principal Axis Components…….....44
Summary……56

3. SOLID-STATE ^{13}C NMR INVESTIGATIONS OF 4,7-DIHYDRO-1H-TRICYCLOPENTA [*DEF,JKL,PQR*]TRIPHENYLENE (SUMANENE) AND INDENO[1,2,3-*CD*]FLUORANTHENE: BUCKMINSTERFULLERENE MOIETIES……59

Introduction……59
Experimental……..65
Results and Discussion…….. 69
Conclusion…… 84

4. SOLID-STATE NMR SPECTRA AND LONG, INTRADIMER BONDING IN THE π-$[TTF]_2^{2+}$ (TTF = TETRATHIAFULVALENE) DICATION…… 86

Introduction……..... 86
Methods……. 91
Results and Discussion…….. 93
Conclusion……111

5. SOLID-STATE ^{13}C NMR INVESTIGATIONS OF CYCLOPHANES: [2,2]PARAYCYCLOPHANE AND 1,8-DIOXA[8](2,7)PYRENOPHANE……...121

Introduction……..121
Experimental……124
Results and Discussion…… 127
Conclusion……..... 137

REFERENCES…… 138

LIST OF TABLES

Table		Page
1.	Irreducible or related spherical tensors……	40
2.	The database used in the examples……..	46
3.	Single crystal vs. FIREMAT data……	51
4.	Theory vs. FIREMAT data……..	55
5.	Experimental and theoretical CSA results for sumanene……	73
6.	Experimental and theoretical CSA results for indenofluoranthene…….	74
7.	The relationship between θ_p, the change in energy associated with curved sumanene from a flat conformation to its curved conformations, and the NMR errors for each conformation……..	80
8.	The relationship between θ_p, the change in energy associated with bending indenofluoranthene from a flat conformation to its curved conformations, and the NMR errors for each conformation……..	82
9.	TTF chemical shift tensor data……..	96
10.	$[TTF]_2^{2+}$ chemical shift tensor data……	97
11.	TTF^+ theoretical chemical shift tensor data……...	103
12.	Molecular orbitals and the contribution to chemical shift…….	112
13.	Comparison between calculated and experimental chemical shifts in TTF…..	115
14.	Calculated chemical shifts of TTF^+……...	117
15.	Comparison between calculated and experimental chemical shift tensors of $[TTF]_2^{2+}$……	118

16. (2,2)Paracyclophane chemical shift tensor data…… 130

17. 1,8-Dioxa[8](2,7)pyrenophane chemical shift tensor data…… 131

LIST OF FIGURES

Figure — Page

1. Chemical shift anisotropy due to the orientation of the molecule within the magnetic field, B_0……. 2

2. Chemical shift tensor values…… 3

3. 5π pulse sequence…… 7

4. Graphical example of Gan's P2DSS replication scheme……. 9

5. A graphical example of the creation of a FIREMAT 2D FID from a 5π 2D FID... 10

6. FIREMAT spectrum of 4,7-di-t-butylacenaphthene…… 12

7. The schematic icosahedral basis of this representation embeds the molecular frame into the object on the left hand side……... 28

8. Schema for *p*-Dimethoxybenzene…… 45

9. Comparison of single crystal and FIREMAT powder data……. 49

10. A principal value plot of theory vs. experiment uses only the δ_{11}, δ_{22}, and δ_{33} terms……. 53

11. Energy difference (in kcal/mol) versus the variance (ppm^2) between experimental chemical shifts and theoretical shielding principal values……. 58

12. Depiction of POAV pyramidalization angle, θ_p, where $\theta_p = \theta_{\sigma\pi} - 90°$and 1, 2, and 3 represent the adjacent atoms bonded to the sp2 hybridized carbon atom at the vertex of the pyramid……..... 62

13. The structures of (a) sumanene and (b) indenofluoranthene……... 64

14. C_{60} with its structural moieties, (a) sumanene and (b) indenofluoranthene illustrating how they can be traced upon its surface……..... 66

15. The numbering schemes for (a) sumanene and (b) indenofluoranthene…….. 70

16. The FIREMAT spectrum of sumanene…… 71

17. The FIREMAT spectrum of indenofluoranthene……. 72

18. Correlation between theoretical chemical shielding and experimentally derived chemical shift for sumanene and indenofluoranthene……. 75

19. The experimental ^{13}C chemical shift principal values of the nonprotonated carbon atoms in indenofluoranthene, sumanene, corannulene, and C_{60} are plotted systematically……... 77

20. Curves consisting of various structural conformations of sumanene associated with inversion bending including (a) the change in energy (kJ/mol) vs. θ_p (Degrees) and (b) the NMR errors (ppm) vs. θ_p (Degrees)……. 79

21. Curves consisting of various structural conformations of indenofluoranthene associated with inversion bending including (a) the change in energy (kJ/mol) vs. θ_p (Degrees) and (b) the NMR errors (ppm) vs. θ_p (Degrees)..…….... 81

22. The molecular structures of TTF and $[TTF]_2^{2+}$…… 87

23. FIREMAT spectrum of TTF…… 94

24. FIREMAT spectrum of $[TTF]_2^{2+}$……. 95

25. Diagram of the crystal structure used in all calculations for $[TTF]_2^{2+}$ taken directly from X-ray data……... 99

26. Calculated chemical shielding tensor principal values vs. experimentally measured chemical shift principal values in TTF and in $[TTF]_2^{2+}$ dimer dication……. 101

27. Experimental (only theoretical data is represented for TTF^+) and theoretical ethylenic ^{13}C chemical shift principal components of TTF, TTF^+, and $[TTF]_2^{2+}$……. 105

28. Experimental (only theoretical data is represented for TTF^+) and theoretical CH ^{13}C chemical shift principal components of TTF, TTF^+, and $[TTF]_2^{2+}$…… 108

29. The natural atomic charges and Wiberg bond orders for (a) TTF, (b) $[TTF]_2^{2+}$, and (c) intradimer bond orders for $[TTF]_2^{2+}$……... 110

30. [2,2]Paracyclophane……. 123

31. 1,8-Dioxa[8](2,7)pyrenophane (a) single molecule with numbering scheme and (b) unit cell containing four molecules…… 125

32. FIREMAT spectrum of [2,2]paracyclophane…….. 128

33. FIREMAT spectrum of 1,8-dioxa[8](2,7)pyrenophane……... 129

34. Correlation between theoretical chemical shielding and experimentally derived chemical shift for [2,2]paracyclophane and 1,8-dioxa[8](2,7)pyrenophane…… 133

35. Experimental (—) and theoretical (----) ^{13}C chemical shift principal components for the nonprotonated carbon atoms in [2,2]paracyclophane and 1,8-dioxa[8](2,7)pyrenophane, as well as corresponding chemical shift components for benzene and pyrene given for a basis of comparison……. 134

ACKNOWLEDGMENTS

For the completion of this work, I am indebted to Professor Ronald J. Pugmire, my research advisor. I am also grateful for Professor David M. Grant, my grandfather, who has supported and encouraged me throughout my entire life to pursue my interest in science. I am grateful for the countless hours these two men have spent in aiding and encouraging me along the way. I thank all of the members of the Grant and Pugmire research group for their friendship and assistance during my time at the University of Utah. I am especially indebted to my beautiful wife, Lindsay, for her undying support of my seemingly endless academic pursuits. She has been the light of my life and gives me purpose to each new day.

Funds for this work were provided by the National Institutes of Health (Grant # NCRR I S10 RR17214-01), the US National Science Foundation (Grant # EEC03044333), and the General Medical Sciences in the National Institutes of Health (Grant # GM08521-47). The Center for High Performance Computing provided computer resources on its Arches system, which was partially funded by the National Institutes of Health (Grant # NCRR I S10 RR17214-01).

Chapter 2 has previously been published in the *Encyclopedia of Magnetic Resonance* and *Concepts in Magnetic Resonance*. Chapters 3 and 4 have previously been published in *Physical Chemistry Chemical Physics* and the *Journal of Physical Chemistry*

A, respectively. Chapter 5 is presently being prepared for submission to *Physical Chemistry Chemical Physics*.

CHAPTER 1

INTRODUCTION

Chemical Shift Tensors

Many tools are important to molecular structure determination. Nuclear magnetic resonance (NMR) spectroscopy is one of these tools. It can be used to determine molecular structure by analyzing nuclei through the shielding effects of their neighboring electrons.[1] The electron distribution around each nucleus within a molecule is rarely spherically symmetric.[1] The number and character of bonds or other interactions in its vicinity removes the symmetry associated with an isolated atom. The chemical shift describes the dependence of nuclear magnetic energy levels on the electronic environment in a molecule.[1] The value of the chemical shift may vary depending on the orientation of the molecule in the magnetic field.[2] This is shown in Figure 1.

The orientational dependence of the chemical shift is best described in terms of a chemical shift tensor, which is a 3x3 matrix that relates the orientation of the magnetic field to a coordinate system defined relative to atomic positions, the molecular frame, in which the induced electronic currents are generated.[1] An example of a chemical shift tensor, including all of the components discussed in this dissertation, is shown in Figure 2.

The chemical shift tensor can be placed into its principal axis system in which all

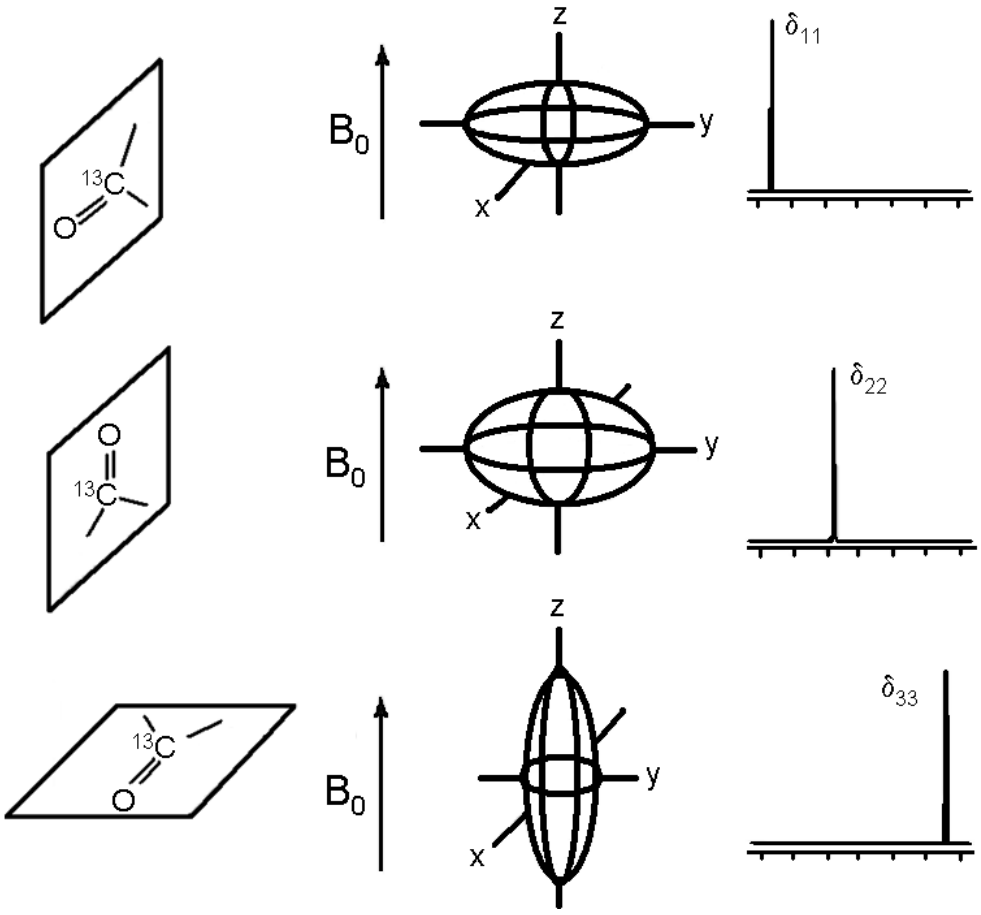

Figure 1. Chemical shift anisotropy due to the orientation of the molecule within the magnetic field, B_0.

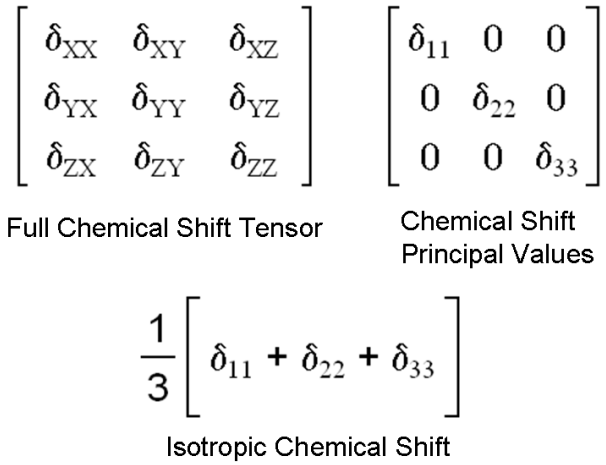

Figure 2. Chemical shift tensor values.[3] (Reprinted with permission from Grant, D. M. "Chemical Shift Tensors", D.M. Grant and R.K. Harris, Eds., *Encyclopedia of NMR*. 1996, *2*, 1303. emrstm 0074)

off-diagonal components are zero.[3] The eigenvalues, or chemical shift principle values, that result are labeled δ_{11}, δ_{22} and δ_{33}.[3] The isotropic chemical shift is one-third of the trace of this diagonalized tensor, where the trace is the sum of the diagonal components.[3] The convention for chemical shift principle value assignment is that $\delta_{33} \leq \delta_{22} \leq \delta_{11}$.[3,4]

The principal values of the chemical shift tensor are associated with specific directions within the molecule, due to the bonding environment surrounding each nucleus.[1] The value of the chemical shift anisotropy can be used to determine conformations of molecules or molecular fragments. Theoretical calculations, such as those performed using the Gaussian03 platform,[5] predict chemical shielding tensors to provide a sensitive probe of electronic structure and can be a useful tool in experimental assignments and analyzing experimental results. The difference between chemical shift and chemical shielding is how they are referenced. Chemical shift is referenced to tetramethylsilane (TMS) and chemical shielding is referenced to a bare nucleus, which is the situation where the diamagnetic shift and the paramagnetic shift are equal to one another.[1,6]

Solid-state NMR spectroscopy produces spectra with broader line widths than solution NMR spectra. This is due to local anisotropic effects experienced by a given nucleus. Line broadening effects are especially pronounced in a static sample, where the resultant spectral line resembles a powder pattern. The powder pattern consists of breakpoints from which the principal values of the chemical shift tensor (δ_{11}, δ_{22}, δ_{33}) can be determined. In a system consisting of multiple spins, the signals often overlap, becoming difficult or impossible to distinguish one powder pattern from another. Therefore, determining the chemical shift principal values in a multispin static system

can be nearly impossible. The use of magic angle spinning has proven to be a useful method of removing many of these complications. As a sample spins, spinning sidebands can be observed. At high spinning speeds, the spinning sidebands of the sample can be spaced out at greater intervals than the measured spectral width. This produces signals that are similar to isotropic spectral lines in solution NMR. Magic angle turning (MAT) experiments utilize slower spinning speeds, 30 – 1000 Hz, in order to include enough spinning sidebands to extract information regarding chemical shift anisotropy for each nucleus, including the chemical shift principal values.

Magic angle spinning and turning experiments involve rotating the sample about an axis tilted at 54.74° referenced to B_0. At the slow spinning speeds in magic angle turning experiments, spinning sideband patterns emerge containing information regarding chemical shift principal values.[3] Magic angle turning experiments began with the magic angle hopping (MAH) experiment developed by Ad Bax.[7] The purpose of MAT and MAH is to preserve and acquire their chemical shift principal value data.[2] These experiments are two dimensional experiments, obtaining isotropic chemical shift information in the evolution dimension and chemical shift anisotropy information in the acquisition dimension.[2] Early work in developing these methods has led to many two dimensional techniques, including the FIve π REplicated Magic Angle Turning (FIREMAT) experiment.[8] The FIREMAT experiment is utilized to extract chemical shift principal values in samples with complicated overlapping spectral peaks.[9-13]

Five π-Replicated Magic Angle Turning (FIREMAT) Experiment [8,13]

The FIREMAT experiment is used to measure chemical shift principal values in powdered solids. It is a sensistive, high resolution two dimensional magic angle turning experiment combining the 5π magic angle turning pulse sequence, a pseudo-2D sideband suppression (P2DSS) experiment, and the technique for importing greater evolution resolution (TIGER).[14,15,16] It requires precise synchronization of the pulses with rotor orientation.

5π Magic Angle Turning Pulse Sequence

The 5π magic angle turning pulse sequence is a phase modulated magic angle turning experiment. This type of phase modulated experiment uses five π-pulses at regular intervals, with respect to one another and with respect to the rotor period, to preserve the phase of the transverse magnetization of the nuclear spins as they precess about B_0 during a single rotor period.[14,15] The timings of the first, third, and fifth π-pulses are variable, allowing phase sampling at different points in the rotor period.[14] Two dimensions are encoded in the resulting FID, isotropic chemical shift information in the evolution dimension and chemical shift anisotropy information in the acquisition dimension.[14] The FIREMAT experiment utilizes this 5π pulse sequence and employs a data rearrangement scheme in order to overcome the resolution limitations of the evolution dimension that are present at higher spinning speeds.[8,13]

The pulse sequence for the 5π experiment is shown in Figure 3. It creates transverse magnetization at t = 0 by conventional cross polarization between the carbon

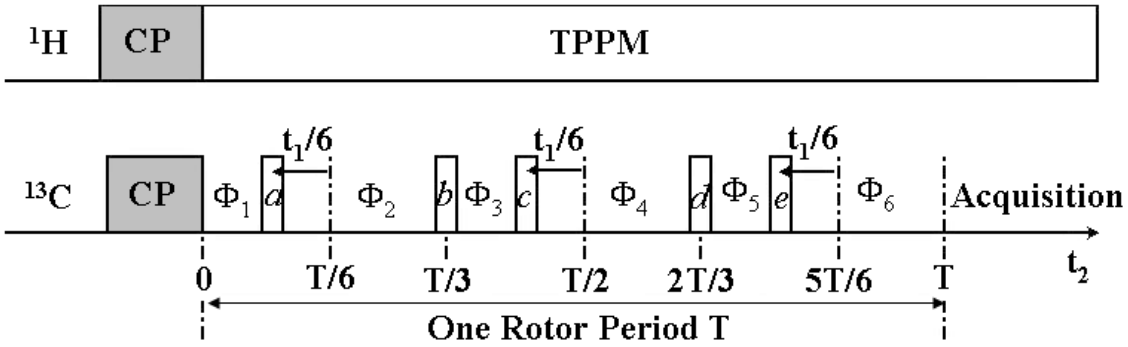

Figure 3. 5π pulse sequence.[8,13] The gray blocks denote the cross polarization step. TPPM is a two pulse phase modulation that is a decoupling scheme. The rectangles with labels *a* – *e* represent 180° pulses. The magnetization precesses in the transverse plane throughout the rotor period and accumulated phases are represented by Φ_i. (Reprinted with permission from Grant, D.M. *Encyclopedia of NMR* eds. Grant, D.M.; Harris, R.K. John Wiley & Sons: Chichester, U.K.,**2002**; Vol. 9; pp 73-90; and Alderman, D.W.; McGeorge, G.; Hu, J.Z.; Pugmire, R.J.; Grant, D.M. *Mol. Phys.* **1998**, *95*, 1113.)

atoms and protons.[13] Five π radiofrequency (RF) pulses, labeled *a* – *e* in Figure 3, cause the magnetization of the carbon atoms to flip 180° before continuing with their normal precession.[8,13] The phase of each RF pulse is aligned with the direction of the initial transverse magnetization.[13] All five of the π pulses are applied during one complete rotor period of duration T.[13] The *a*, *c*, and *e* pulses are applied at variable times T/6–t_1/6, T/2–t_1/6, and 5T/6–t_1/6 in order to allow phase sampling at different points in the rotor period.[13] The *b* and *d* 180° pulses occur at the fixed times T/3 and 2T/3 during the rotor period, T.[13] A two pulse phase modulation (TPPM) proton decoupling scheme is employed to narrow the carbon lines and improve signal to noise.[13]

The 5π pulse sequence produces a complex, phase modulated 2D FID that Fourier transforms to a spectrum with only the isotropic shift expressed in the evolution dimension. Spinning sidebands do not appear in the evolution dimension. The acquisition dimension yields the response characteristics and the principal values of the diagonalized shift tensor.

Pseudo-2D Sideband Suppression

The FIREMAT experiment utilizes a data replication scheme that is based on the P2DSS experiment developed by Gan.[15] A graphic of Gan's data rearrangement scheme is shown in Figure 4.[15] Gan's P2DSS sequence uses the 5π pulse sequence but only samples the acquisition dimension at whole rotor periods, T. The magic angle turning creates rotational echoes, allowing the data rearrangement as shown in Figure 4. The echoes in both dimensions can allow isotropic data tables to be populated solely from acquisition magnetization detected at multiples of T.[8] The resulting FID can subsequently be Fourier transformed into an isotropic chemical shift spectrum similar to a

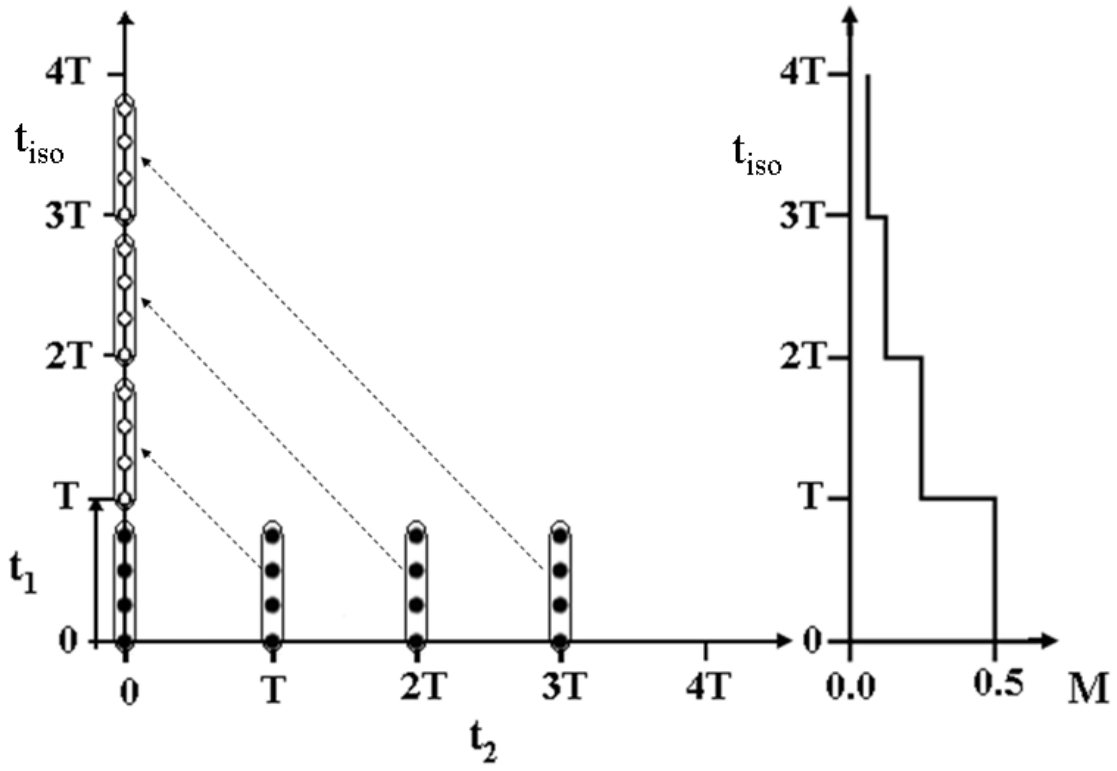

Figure 4. Graphical example of Gan's P2DSS replication scheme. The 2D FID is sampled in the acquisition dimension only at the echo position of the rotor. The solid circles (•) represent the actual data. The open circles (o) are replicated data obtained from the measured data and transported as shown in the figure. The right-hand side of the figure schematically represents the attenuation of the echo intensity due to relaxation during one rotation. This data rearrangement scheme is given in Alderman et al.[13] and in Grant.[8] Grant, D.M. *Encyclopedia of NMR* eds. Grant, D.M.; Harris, R.K. John Wiley & Sons: Chichester, U.K.,**2002**; Vol. 9; pp 73-90; and Alderman, D.W.; McGeorge, G.; Hu, J.Z.; Pugmire, R.J.; Grant, D.M. *Mol. Phys.* **1998**, *95*, 1113.)

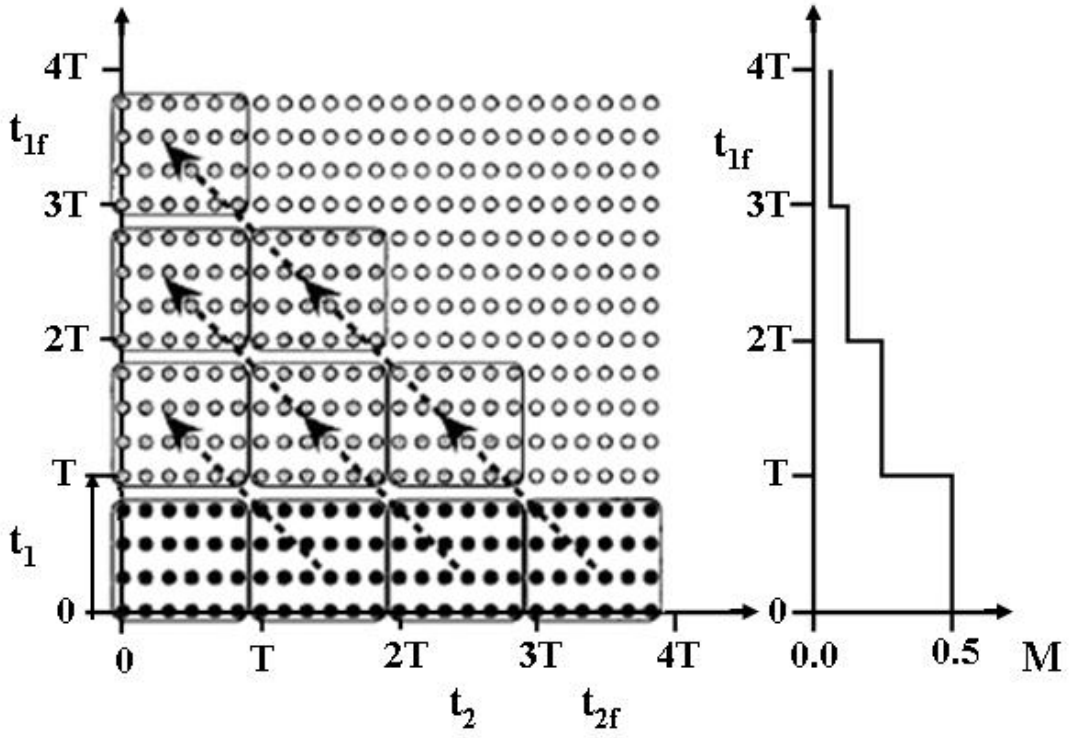

Figure 5. A graphical example of the creation of a FIREMAT 2D FID from a 5π 2D FID. The acquisition (t_2) and evolution (t_1) times are shown on the horizontal and vertical axes respectively. The solid circles (•) represent the points at which the 5π 2D FID is sampled. The open circles (o) represent zero-filled points and the shaded circles (◦) are created by replicating the solid circles in groups of 6 x 4 = 24. The stepped relaxation function that appears in the evolution dimension is plotted on the right. This data rearrangement scheme is given in Alderman et al.[13] The transverse magnetization decays over time as a function of t_1 and t_2.[8] Grant, D.M. *Encyclopedia of NMR* eds. Grant, D.M.; Harris, R.K. John Wiley & Sons: Chichester, U.K.,**2002**; Vol. 9; pp 73-90; and Alderman, D.W.; McGeorge, G.; Hu, J.Z.; Pugmire, R.J.; Grant, D.M. *Mol. Phys.* **1998**, *95*, 1113.)

CP/MAS spectrum.[15] This data replication is possible because of a correspondence between the evolution and acquisition dimensions when the latter is sampled at multiples of whole rotor periods, T.[15] Therefore, by sampling the acquisition dimension for an extended period of time and sampling the evolution dimension often via multiples of its spectral width, the P2DSS experiment improves its signal resolution.[15]

The FIREMAT experiment expands upon the principles of the P2DSS data rearrangement scheme by digitizing data throughout the whole rotor period as shown in Figure 5.[8,13] The FIREMAT replication scheme uses the acquisition dimension data to create its extended evolution dimension.[13] Thus, only positive times are available and the datasets are therefore not hypercomplex.[15]

Data Fitting Protocol

The two dimensional FIREMAT data is then fit using a fitting protocol called *Technique for Importing Greater Evolution Resolution* (TIGER).[16] The TIGER processing technique uses a linear least-squares model derived from a "guide" spectrum to fit the experimental data.[16] The amount of data which must be acquired is significantly reduced, by importing spectral information from the "guide" spectrum.[16] This causes a significant reduction in the amount of time spent analyzing the data.[16] TIGER processing provides phasable data from datasets which are not hypercomplex and significantly reduces analysis time by incorporating evolution information external to the analysis.[16] Since fewer points are needed to develop the evolution dimension in the two dimensional analysis, it is completed in a shorter amount of time. An example of a FIREMAT spectrum that the author has worked on is given in Figure 6.[17]

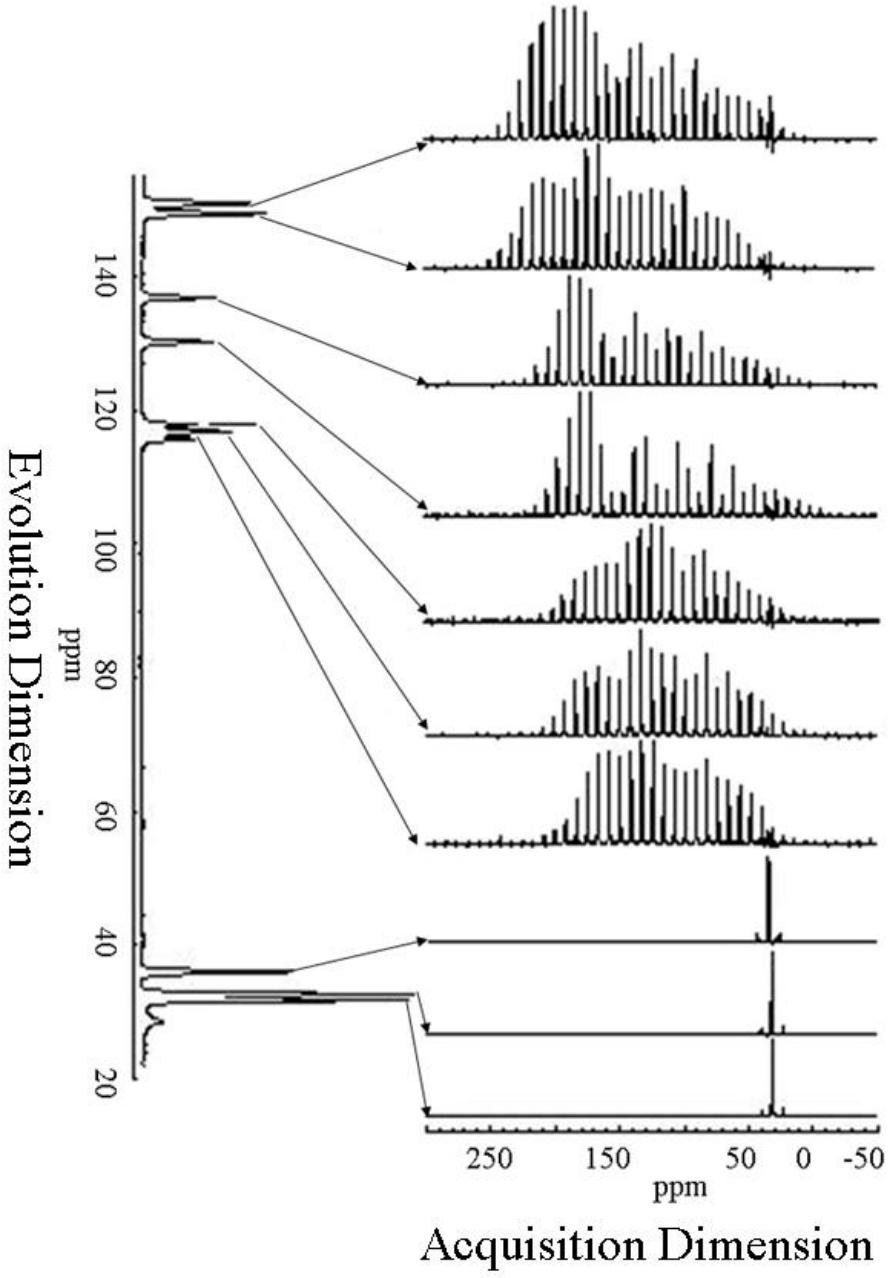

Figure 6. FIREMAT spectrum of 4,7-di-t-butylacenaphthene.[17] (Reprinted with permission from Ma, Z.; Halling, M.D.; Solum, M.S.; Harper, J.K.; Orendt, A.M.; Facelli, J.C.; Pugmire, R.J.; Grant, D.M.; Amick, A.W.; Scott, L.T. *J. Phys. Chem. A.* 2007, *111,* 2020-2027.)

Theoretical NMR Calculations

Computational quantum mechanical methods provide a valuable tool in correlating experimental NMR stereochemistry data with stereochemistry information derived by X-ray diffraction methods. Molecular structure and function can be investigated through various computational methods in a manner unavailable to researchers of even a decade ago. Computational modeling programs utilize quantummechanical descriptions of molecules or solve for the Schrödinger equation ab initio using perturbation methods at varying levels of theory. The advancement of NMR techniques in connection with these computational methods has enabled a more thorough exploration of structural properties. Entire molecular geometries have now been predicted by combining solid-state chemical shift values with ab initio calculations.[18] Structural predictions have also been made using dipolar coupling information combined with computation, and also through the use of spin diffusion models.[19-21] Chemical shift principal values have been used to sort through and select conformers found through X-ray powder diffraction (XRPD) procedures.[22] These studies set a precedent for the use of solid-state NMR spectroscopy in analyzing solids that would be inaccessible using conventional methods.

Density functional theory is a computational method that utilizes the electron density to provide useful information regarding the magnetic properties of molecules. As seen in Chapters two through five, along with various other studies mentioned and referenced throughout this dissertation, this has been done to a high degree of agreement with experimental data. Density functional theory treats nuclei as point charges with their positions corresponding to local maxima in the electron density. By starting with

the electron density, the Schrödinger equation can be solved; and wavefunctions and corresponding eigenvalues may be determined.

When analyzing and contrasting chemical shift tensors it is extremely useful to have a quantitative measure of the difference between two tensors. For instance, a computational model may be fit to experimental data by adjusting the parameters of the model to minimize the differences between the computed and measured tensor values.[23] Chemical shift tensors also provide a means for comparing polymorphs on an atom-by-atom basis.[23] An appropriate measurement of contrast and fit is a scalar "distance" between the tensors.[23] The distance between two tensors is a variance calculation and provides useful information about three-dimensional differences between two chemical shift tensors.[23]

The discussion of the components of the chemical shift tensor and the distance between tensors usually takes place in Cartesian space. Chemical shift principal values are conventionally reported in literature in the Cartesian basis with the chemical shift tensor characterized by a 3x3 Cartesian matrix with nine independent elements with the three components of the diagonalized matrix being the chemical shift principal values.[23]

There is a problem comparing two tensors when they are described solely by their chemical shift principal values.[23] By neglecting the orientational Euler angles, α, β, and γ, relating the two tensors, it becomes impossible to determine whether two tensors are identical or merely congruent.[23] Two tensors are identical if their principal values and the spatial orientation of their principal axes agree completely. They are congruent only if they share the same set of principal values but the orientations of the principal axes differ. This situation is commonly encountered in solid-state NMR and the idea of

comparing two tensors is complicated.[23] Comparing two different tensors described with mixed parameters, and the statistical comparison of these tensors, requires weighting matrices.[23] This set of weighting matrices including a detailed discussion and derivation of the distance matrices in the three separate bases: Cartesian, Irreducible Spherical, and Icosahedral, is provided in Chapter 2, which is also double published in the journal *Concepts of Magnetic Resonance* and in the *Encyclopedia of Magnetic Resonance*.

CHAPTER 2

THE USE OF METRIC SPACES IN NMR CRYSTALLOGRAPHY*

Introduction

Chemical structural information may be obtained from direct dipolar couplings that depend on the inverse cubic interactions (see section ‘‘Use of Dipole Interactions’’). Chemical shift tensors also provide high quality structural information by comparing these experimental values with theoretical calculations of nuclear shielding tensor quantities derived from Quantum Mechanical models of various molecular or lattice structures (see section ‘‘Use of Chemical Shift-Tensors’’). To make these calculations representation-invariant, a metric expression must be implemented that will provide the statistical weighting factors for treating the tensor component differences of the experimental and theoretical quantities (see section ‘‘The Mean Squared Deviation, d^2, in Metric Space’’). Three tensor representations are discussed, i.e., the traditional Cartesian (see section ‘‘The Cartesian Chemical-Shift Representation’’), the irreducible spherical (see section ‘‘The Irreducible Spherical Representation’’), and the Icosahedral (see section The Icosahedral (or it’s directly related Dodecahedron) Symmetry

---

* Reprinted with permission from Grant, D. M.; Halling, M. D. "Metric spaces in NMR crystallography" in "Encyclopedia of Magnetic Resonance", eds.-in-chief R.K. Harris & R.E. Wasylishen, John Wiley & Sons Ltd. Chichester, DOI: 10.1002/9780470034590.emrstm1063. On-line posting date 15 September **2009**; Grant, D. M.; Halling, M. D. *Concepts in Magn. Reson. A.* **2009**, *34A (4)*, 217-237.

Representation'') that is also an irreducible geometric metric. The Cartesian metric tensor is a reducible matrix that lacks the orthogonal properties of the two irreducible tensors. Derivations of expressions and illustrations of the use are provided herein.

Use of Dipole Interactions[21,24-31]

Dipolar measurements on solid samples provide an excellent approach to determine crystal structures in both single crystals and microcrystalline solid powders. Lattice separations between nuclei affect the dipole-dipole coupling constants, where the magnitude of the couplings attenuate with an inverse cubic law (i.e., $1/r^3$). Hence, these methods exhibit high relative sensitivity upon intra-nuclear distances. These dipolar structural parameters are complementary to chemical shift correlations with molecular structural models that are central to this review. These two interactions constitute the primary methods used in NMR Crystallography.

Use of Chemical Shift-Tensors[7-13, 21,32-54]

This review deals with the use of chemical shift tensors and their relation to structural determinations. The shift/structure relationship involves modeling the structural dependence of chemical-shift tensors using modern chemical quantum mechanical (CQM) methods. In this approach the wave functions are usually optimized by minimizing the molecular energy to provide a trial structure in a molecular Cartesian frame. The grid-search algorithm of Heider et al. [32] also may be employed to explore structural conformation angles or intra-molecular repulsions (note: the CQM and grid-search approaches usually yield similar molecular structures). The structure associated with the most favorable statistical measure of the theoretical/experimental tensor

agreement is taken to be the most promising structure. Consequently, chemical shift tensor methods need a reliable statistical package for distinguishing among alternative molecular structures. Critical weighting factors based on metric considerations are used to optimize the relative importance of various shift-tensor components. It is important to make measurements, which are invariant to the mathematical representations used for expressing a chemical-shift tensor. These useful weighting matrices[55] (designated as metric tensors, metric matrices, or simply transformation matrices in metric space) use standard Riemann metric techniques[56] to create the relationships. The metric space, used herein to compare two related chemical shift components, is based on mean squared deviations or so-called mean squared distances (d^2) between a pair of tensors. The spatial integrals over the domain of d^2 in metric space render the d^2 invariant for different representations of the chemical-shift tensor.

The Chemical-Shift Tensor Discussion

The Cartesian Chemical-Shift Representation[57]

In Cartesian three-dimensional space, the chemical-shift tensor is defined for the k^{th} nucleus in a molecular frame as follows:

$$\begin{aligned}\delta_{\text{Cart}}(k) &= \begin{pmatrix} c_x & c_y & c_z \end{pmatrix} \begin{pmatrix} \delta_{xx}(k) & \delta_{xy}(k) & \delta_{xz}(k) \\ \delta_{yx}(k) & \delta_{yy}(k) & \delta_{yz}(k) \\ \delta_{zx}(k) & \delta_{zy}(k) & \delta_{zz}(k) \end{pmatrix} \begin{pmatrix} c_x \\ c_y \\ c_z \end{pmatrix} \\ &= c_x{}^2\delta_{xx}(k) + c_y{}^2\delta_{yy}(k) + c_z{}^2\delta_{zz}(k) \\ &\quad + 2c_xc_y\delta_{xy}(k) + 2c_yc_z\delta_{yz}(k) + 2c_zc_x\delta_{zx}(k)\end{aligned} \tag{1}$$

where the orientation of the Cartesian chemical-shift, $\delta_{\text{Cart}}(k)$, on the left-hand side (LHS) of Eq. 1 lies parallel with the magnetic field. The index ***k*** represents various

nuclei (To minimize notational complexity, the index ***k*** is always implied but often omitted), and the chemical-shift components, $\delta_{ij}(k)$, constitute a symmetric tensor, i.e., $\delta_{ij}(k) = \delta_{ji}(k)$. The directional cosines (e.g., c_i or c_j) define the angles between the magnetic field and the three molecular-axis coordinates, i.e., i or j (=*x*,*y*,*z*) that define the molecular frame. Note, $(c_x^2 + c_y^2 + c_z^2) = 1$. A single Cartesian molecular frame is required to model the composite atomic array, which is required to specify the molecular structure with theoretical CQM methods. Unfortunately, multiple principal shift axes in the Cartesian frames[58] are often confused with the single molecular structure Cartesian frame. We reserve the x,y,z labels for atomic structure arrays in molecular crystals and then reserve the 11, 22, 33 notation for principle shift and screening labels.

The Separation of the Full Tensor into Symmetric and Antisymmetric Components

The purpose of this separation is given elsewhere in the encyclopedia.[8] A symmetric tensor includes only the zero-rank and second-rank terms as the first-rank terms produce only insignificant perpendicular perturbations to the magnetic field. Such a feature gives rise to so-called secular approximations that leave the odd rank perturbations unobserved in the Zeeman frame and negate their contribution in the chemical shifts. The zero-rank term is directly related to a scalar quantity, referred to as the isotropic shift, i.e., $\delta_{iso} = \frac{1}{3}\left(\delta_{xx} + \delta_{yy} + \delta_{zz}\right)$. The isotropic chemical shift may be scaled arbitrarily to any reference shift of choice, although tetramethysilane (TMS) is usually the fiducial reference for the ^{1}H and ^{13}C nuclear isotopes. Two other linearly independent combinations of δ_{xx}, δ_{yy}, and δ_{zz} along with the δ_{xy}, δ_{yz}, and δ_{zx} off-diagonal

terms complete the *five* second-rank anisotropic terms in the spherical chemical-shift tensor (see the irreducible spherical representations[59] below).

The Mean Squared Deviation, d^2, in Metric Space[23]

Most of the development in this review depends on Ref. 23 (Most of the development in this review depends on this citation). Mathematically, the mean squared difference between two functions, $f(\omega)$ and $g(\omega)$, is defined as follows:

$$d^2 = \frac{\int [f(\omega) - g(\omega)]^2 \, d\omega}{\int d\omega} \tag{2}$$

where ω specifies the domain variables used in the analysis. This quadratic form for d^2 measures differences due to intrinsic variations, diverse model origins, and measurement errors in the two functions. When one compares two experimental shift tensors, the difference usually reflects random measurement errors, but more important the deviations between experimental and theoretical tensors reflect variations in the molecular structure, the primary topic of interest in this review. The d^2 distance, when due to actual or pseudo random errors correspond to changes in the statistical variance and confidence intervals that can be obtained from variance analysis (e.g., the F-test used in statistical analysis). A comparison of two theoretically modeled tensors may reflect the differences in the CQM methods for computing the tensor quantities or else intrinsic differences in the structural features of the model. If these distributions are systematic and do not follow Gaussian distributions, it may not be possible to obtain a statistical confidence level unless one can assume them to be pseudo-random based on the validity of the basic molecular model or features of the corresponding computation. When one compares simultaneously experimental and theoretical tensor quantities, the experimental

measurement errors combine with computational diversities arising from the CQM methods. In this case the combined error analysis could obscure a clear interpretation.

Mean Squared Distance Between Two Chemical Shift Tensors

Using Eq. 2 the distance for the *k*th nucleus, given by $d^2(k)$ in chemical-shift deviation or error space, is as follows:

$$(k) = \frac{\int \sum_S \left| F_{R,S}(\Omega) - G_{R,S}(\Omega) \right|^2 d\Omega}{\int d\Omega} = \frac{1}{4\pi} \int \sum_S \left| F_{R,S}(\Omega) - G_{R,S}(\Omega) \right|^2 d\Omega \qquad (3)$$

where *R* is one of a variety of shift representations and the *S* indices designate the spatial variables. $F_{R,S}(\Omega)$ and $G_{R,S}(\Omega)$ are two chemical shift tensor functions, involving both shifts and spatial features to be compared over the domain represented by, $\Omega = \Omega(\theta, \phi)$, where θ and ϕ are standard polar angles. The denominator, 4π, in the first term on the right-hand side (RHS) of Eq. 3 normalizes the angular terms for the two tensor functions using the common integral:

$$\int d\Omega = \int_0^{\pi} \int_0^{2\pi} \sin\theta \, d\theta \, d\phi = 4\pi . \qquad (4)$$

The expressions for $F_{R,S}(\Omega)$ and $G_{R,S}(\Omega)$ embody all of the features of Eq. 1 that define both the spatial and nuclear spin characteristics of a shift tensor. The spatial parts of the chemical shift tensors are written in directional cosines that may be easily converted to polar angles. The form of these terms is given as follows:

$$
\begin{aligned}
F_{\mathrm{Cart},\mu}(\Omega) &= \sum_{\mu=xx}^{zx} S_{\mu}(\Omega)\,{}^{1}\delta_{\mu} \\
&= S_{xx}(\Omega)\,{}^{1}\delta_{xx} + S_{yy}(\Omega)\,{}^{1}\delta_{yy} + S_{zz}(\Omega)\,{}^{1}\delta_{zz} + S_{xy}(\Omega)\,{}^{1}\delta_{xy} + S_{yz}(\Omega)\,{}^{1}\delta_{yz} + S_{zx}(\Omega)\,{}^{1}\delta_{zx}. \\
G_{\mathrm{Cart},\eta}(\Omega) &= \sum_{\eta=xx}^{zx} S_{\eta}(\Omega)\,{}^{2}\delta_{\eta} \\
&= S_{xx}(\Omega)\,{}^{2}\delta_{xx} + S_{yy}(\Omega)\,{}^{2}\delta_{yy} + S_{zz}(\Omega)\,{}^{2}\delta_{zz} + S_{xy}(\Omega)\,{}^{2}\delta_{xy} + S_{yz}(\Omega)\,{}^{2}\delta_{yz} + S_{zx}(\Omega)\,{}^{2}\delta_{zx}.
\end{aligned}
\tag{5}
$$

where the shift tensors are given by ${}^{1}\delta_{\mu}$ and ${}^{2}\delta_{\eta}$. The 1 and 2 superscripts on the LHS of the shift symbol designate the two tensor components to be compared. These two tensors identify with $F_{\mathrm{Cart}}(\Omega)$ and $G_{\mathrm{Cart}}(\Omega)$, respectively. In the Cartesian representation found in Eq. 1, only projections of the chemical shift tensor components along the magnetic field are relevant; hence the directional cosines specify this structural feature. The angular spatial terms for the molecular orientation on a sphere of unit radius are given by $S_{\mu}(\Omega)$ and likewise $S_{\eta}(\Omega)$,

$$
\begin{aligned}
S_{xx} &= c_x{}^2 = \sin^2\theta\cos^2\phi; & S_{xy} &= 2c_x c_y = 2\sin^2\theta\cos\phi\sin\phi; \\
S_{yy} &= c_y{}^2 = \sin^2\theta\sin^2\phi; & S_{yz} &= 2c_y c_z = 2\cos\theta\sin\theta\sin\phi; \\
S_{zz} &= c_z{}^2 = \cos^2\theta; & S_{zx} &= 2c_z c_x = 2\cos\theta\sin\theta\cos\phi.
\end{aligned}
\tag{6}
$$

The Expansion of $d^2(k)$ Using Orthogonal Properties of the Spatial Functions, $S_{\mu}(\Omega)$

If the various matrices and vectors are complex the square of the deviation requires complex conjugates to form squared terms. Furthermore, it is the squared difference between ${}^{1}\delta_{\mu}$ and ${}^{2}\delta_{\eta}$ which is the basis of the mathematical expressions and these two tensors must be paired with a Krönecker delta ($K_{\mu,\eta}$) in μ and η specified by the integrals given in Equations 3 and 7 (A Kronecker delta may be used to pair the corresponding components of the compared tensors, but we found that this unduly complicated the

formatting of the equations. This term is understood intuitively but neglected for the sake of simplicity). Hence, the expression for $d^2(k)$ of the k nucleus becomes:

$$d^2(k) = \frac{1}{4\pi}\int \sum_{S,S'} \left|F_{R,S}(\Omega) - G_{R,S'}(\Omega)\right|^2 d\Omega = \frac{1}{4\pi}\int d\Omega \sum_{\mu,\eta} \left|S_\mu(\Omega)\,{}^2\delta_{R,\mu}(k) - S_\eta(\Omega)\,{}^1\delta_{R,\eta}(k)\right|^2$$

$$d^2(k) = \frac{1}{4\pi}\left\{\int d\Omega \sum_{\mu,\eta}\left({}^2\delta^*_{\text{Cart},\mu}(k) - {}^1\delta^*_{\text{Cart},\mu}(k)\right)\left[S^*_\mu(\Omega)S_\eta(\Omega)\right]\left({}^2\delta_{\text{Cart},\eta}(k) - {}^1\delta_{\text{Cart},\eta}(k)\right)\right\} \quad (7)$$

$$d^2(k) = \sum_{\mu,\eta}\left\{\left({}^2\delta^*_{\text{Cart},\mu}(k) - {}^1\delta^*_{\text{Cart},\mu}(k)\right)P_{\text{Cart},\mu,\eta}(\Omega)\left({}^2\delta_{\text{Cart},\eta}(k) - {}^1\delta_{\text{Cart},\eta}(k)\right)\right\}.$$

The metric for the Cartesian matrix is given by:

$$P_{\text{Cart},\mu,\eta}(\Omega) = \frac{1}{4\pi}\int S^*_\mu(\Omega)S_\eta(\Omega)d\Omega. \quad (8)$$

Using the spatial metric, $P_{\text{Cart},\mu\eta}(\Omega)$, the orthogonal relationships may now be exhibited. The integration, over the spherical angles from *0* to π for θ and from *0* to 2π for ϕ, respectively, is easily completed by substituting the polar angles from Eq. 6 into Eq. 8. These integrations correspond to spectroscopic spatial symmetry rules. Twelve metric matrices have spatial terms that leave the spatial functions orthogonal and these matrices have zero magnitudes given in Eq. 9 as follows:

$$\begin{aligned}
&P_{\text{Cart},xx,xy}(\Omega) = P_{\text{Cart},xx,yz}(\Omega) = P_{\text{Cart},xx,zx}(\Omega) = 0\\
&P_{\text{Cart},yy,xy}(\Omega) = P_{\text{Cart},yy,yz}(\Omega) = P_{\text{Cart},yy,zx}(\Omega) = 0\\
&P_{\text{Cart},zz,xy}(\Omega) = P_{\text{Cart},zz,yz}(\Omega) = P_{\text{Cart},zz,zx}(\Omega) = 0\\
&P_{\text{Cart},xy,yz}(\Omega) = P_{\text{Cart},xy,zx}(\Omega) = P_{\text{Cart},yz,zx}(\Omega) = 0.
\end{aligned} \quad (9)$$

Nine of the spatial operators in the metric integrals have numerical values that are given below in Eq. 10.

$$P_{\text{Cart},xx,xx}(\Omega) = 1/4\pi \int S^*_{xx}(\Omega) S_{xx}(\Omega) d\Omega = 1/4\pi \int_0^{\pi} \sin^5\theta d\theta \int_0^{2\pi} \cos^4\phi \, d\phi = 1/5 = 3/15,$$
$$P_{\text{Cart},yy,yy}(\Omega) = 1/4\pi \int S^*_{yy}(\Omega) S_{yy}(\Omega) d\Omega = 1/4\pi \int_0^{\pi} \sin^5\theta d\theta \int_0^{2\pi} \sin^4\phi \, d\phi = 1/5 = 3/15, \quad (10a)$$
$$P_{\text{Cart},zz,zz}(\Omega) = 1/4\pi \int S^*_{zz}(\Omega) S_{zz}(\Omega) d\Omega = 1/4\pi \int_0^{\pi} \cos^4\theta \sin\theta d\theta \int_0^{2\pi} d\phi = 1/5 = 3/15.$$

$$P_{\text{Cart},xx,yy}(\Omega) = 1/4\pi \int S^*_{xx}(\Omega) S_{yy}(\Omega) d\Omega = 1/4\pi \int_0^{\pi} \sin^5\theta d\theta \int_0^{2\pi} \cos^2\phi \sin^2\phi \, d\phi = 1/15,$$
$$P_{\text{Cart},yy,zz}(\Omega) = 1/4\pi \int S^*_{yy}(\Omega) S_{zz}(\Omega) d\Omega = 1/4\pi \int_0^{\pi} \cos^2\theta \sin^3\theta d\theta \int_0^{2\pi} \sin^2\phi \, d\phi = 1/15, \quad (10b)$$
$$P_{\text{Cart},zz,xx}(\Omega) = 1/4\pi \int S^*_{zz}(\Omega) S_{xx}(\Omega) d\Omega = 1/4\pi \int_0^{\pi} \cos^2\theta \sin^3\theta d\theta \int_0^{2\pi} \cos^2\phi \, d\phi = 1/15$$

$$P_{\text{Cart},xy,xy}(\Omega) = 1/4\pi \int S^*_{xy}(\Omega) S_{xy}(\Omega) d\Omega = 1/4\pi \int_0^{\pi} 4\sin^5\theta \, d\theta \int_0^{2\pi} \cos^2\phi \sin^2\phi \, d\phi = 4/15,$$
$$P_{\text{Cart},yz,yz}(\Omega) = 1/4\pi \int S^*_{yz}(\Omega) S_{yz}(\Omega) d\Omega = 1/4\pi \int_0^{\pi} 4\cos^2\theta \sin^3\theta \, d\theta \int_0^{2\pi} \sin^2\phi \, d\phi = 4/15, \quad (10c)$$
$$P_{\text{Cart},zx,zx}(\Omega) = 1/4\pi \int S^*_{zx}(\Omega) S_{zx}(\Omega) d\Omega = 1/4\pi \int_0^{\pi} 4\cos^2\theta \sin^3\theta \, d\theta \int_0^{2\pi} \cos^2\phi \, d\phi = 4/15.$$

The reader may prove these relationships using standard trigonometric functions and the appropriate integral tables (Equations 9 and 10 were derived by the authors using Maple(TM). Maple 11.0. Maplesoft, a division of Waterloo Maple Inc., Waterloo, Ontario). Substituting the integral values of Eq. 9 and 10 into Eq. 8 gives the Cartesian metric matrix as follows:

$$P_{\text{Cart}}(\Omega) = \frac{1}{15} \cdot \begin{pmatrix} \mathbf{3} & \mathbf{1} & \mathbf{1} & \mathbf{0} & \mathbf{0} & \mathbf{0} \\ \mathbf{1} & \mathbf{3} & \mathbf{1} & \mathbf{0} & \mathbf{0} & \mathbf{0} \\ \mathbf{1} & \mathbf{1} & \mathbf{3} & \mathbf{0} & \mathbf{0} & \mathbf{0} \\ \mathbf{0} & \mathbf{0} & \mathbf{0} & \mathbf{4} & \mathbf{0} & \mathbf{0} \\ \mathbf{0} & \mathbf{0} & \mathbf{0} & \mathbf{0} & \mathbf{4} & \mathbf{0} \\ \mathbf{0} & \mathbf{0} & \mathbf{0} & \mathbf{0} & \mathbf{0} & \mathbf{4} \end{pmatrix}. \quad (11)$$

Note, this matrix contains off-diagonal terms for the shift tensor components lying along the diagonal Cartesian tensor. Thus, this tensor yields a reducible representation in the group theory sense and these components (except for δ_{xy}, δ_{yz}, and δ_{zx}) lack

orthogonality. Substituting Eq. 11 into Eq. 7 yields the following expression for $d^2(k)$ in matrix form:

$$d^2(k) = \frac{1}{15}\left(\left[{}^2\delta^*_{xx} - {}^1\delta^*_{xx}\right]\left[{}^2\delta^*_{yy} - {}^1\delta^*_{yy}\right]\left[{}^2\delta^*_{zz} - {}^1\delta^*_{zz}\right]\left[{}^2\delta^*_{xy} - {}^1\delta^*_{xy}\right]\left[{}^2\delta^*_{yz} - {}^1\delta^*_{yz}\right]\left[{}^2\delta^*_{zx} - {}^1\delta^*_{zx}\right]\right)\begin{pmatrix} 3&1&1&0&0&0\\ 1&3&1&0&0&0\\ 1&1&3&0&0&0\\ 0&0&0&4&0&0\\ 0&0&0&0&4&0\\ 0&0&0&0&0&4 \end{pmatrix}\begin{pmatrix} \left[{}^2\delta_{xx} - {}^1\delta_{xx}\right]\\ \left[{}^2\delta_{yy} - {}^1\delta_{yy}\right]\\ \left[{}^2\delta_{zz} - {}^1\delta_{zz}\right]\\ \left[{}^2\delta_{xy} - {}^1\delta_{xy}\right]\\ \left[{}^2\delta_{yz} - {}^1\delta_{yz}\right]\\ \left[{}^2\delta_{zx} - {}^1\delta_{zx}\right] \end{pmatrix} \quad (12)$$

Expanding Eq. 12 yields the following algebraic expression in the molecular frame for $d^2(k)$:

$$d^2(k) = \frac{1}{15}\cdot\left\{\begin{array}{l} 3\left({}^2\delta_{xx} - {}^1\delta_{xx}\right)^2 + 3\left({}^2\delta_{yy} - {}^1\delta_{yy}\right)^2 + 3\left({}^2\delta_{zz} - {}^1\delta_{zz}\right)^2 + \\ 2\left({}^2\delta_{xx} - {}^1\delta_{xx}\right)\left({}^2\delta_{yy} - {}^1\delta_{yy}\right) + 2\left({}^2\delta_{yy} - {}^1\delta_{yy}\right)\left({}^2\delta_{zz} - {}^1\delta_{zz}\right) + 2\left({}^2\delta_{zz} - {}^1\delta_{zz}\right)\left({}^2\delta_{xx} - {}^1\delta_{xx}\right) + \\ 4\left({}^2\delta_{xy} - {}^1\delta_{xy}\right)^2 + 4\left({}^2\delta_{yz} - {}^1\delta_{yz}\right)^2 + 4\left({}^2\delta_{zx} - {}^1\delta_{zx}\right)^2 \end{array}\right\}. \quad (13)$$

Metric Matrices for Other Chemical-Shift Representations

Even though the chemical shift tensor is initially defined in the Cartesian representation, the corresponding shift components, unfortunately, fail to yield an orthogonal basis set. This makes it impossible to model, with statistics, the data with a least-squares line in a plot of theoretical tensor shieldings vs. experimental shifts. Such plots of ${}^{\lambda}\sigma_{\mu} = -\,\mathrm{m}\,{}^{\lambda}\delta_{\mu} + \sigma_{\mu}\,(\mathrm{TMS})$ link molecular structure to chemical shift terms and are validated by a slope, m, of minus unity and establish the relationship between the chemical shift and corresponding nuclear screening references.

Note, the off-diagonal terms in Eq. 11 give rise to cross products shown in the second line of Eq. 13. When these cross terms are neglected the statistical analysis of a linear fit is affected accordingly in chemical-shift structural modeling. This problem with Cartesian tensors was identified over fifty years ago in Rose's book on angular momentum wherein he indicated that tensors are defined by their transformation properties as they change coordinate systems.[60] He also discussed Cartesian tensors and some of the challenges of working with them such as usually appearing in reducible form.[60] The linear combination of irreducible tensors, fortunately, allows one to obtain a least-squared line that yields the best fit structure in the molecular frame.

We now consider two irreducible shift representations (i.e., the symmetrical geometric representation based on the symmetry of an icosahedron and the irreducible spherical basis used extensively for over a half century in the definition of spherical harmonics).[60] These two additional mathematical representations provide metrics that are orthonormal. The Cartesian representation can also yield a third invariant value for $d^2(k)$. Further, computational machinery for moving among different chemical shift representations is also presented.

The Icosahedral (or Its Related Dodecahedron)

Symmetry Representation

Alderman and co-workers[23] developed the metric for this representation. The geometric basis for this representation lies in the six a-polar directions connecting pairs of vertices of an icosahedron. Each unique direction passes through the center of an icosahedron and two vertices possessing inversion symmetry to each other. This symmetry, which places all six unique directions equidistance from one another, is also

identical to the six a-polar directions that pass through the inversion epicenter of a dodecahedron and the twelve external facial planes of a dodecahedron. Haeberlen et al.[61] recently drew the parallel between metric and group theory representations for the icosahedral symmetry basis. This work by Haeberlen and co-workers[61] on ^{1}H shielding tensors illustrates one of the principal benefits of the icosahedral representation. The reader is referred to several papers[22,32-35, 62-66] in the icosahedral representation.

The six unique directions in the three-dimensional icosahedron are exhibited in Figure 7. The icosahedron orientation of the basis relative to the XYZ molecular frame also is given in Figure 7. This basis allows one to express the six symmetry directions in terms of structural directional cosines and tensor components found in Eq. 1 and applied to the icosahedron.

The icosahedral tensor representation is given explicitly by the following:

$$
\begin{aligned}
{}^{\lambda}\delta_{\mathrm{icos},1} &= a^2\,{}^{\lambda}\delta_{xx} + b^2\,{}^{\lambda}\delta_{yy} - 2ab\,{}^{\lambda}\delta_{xy}, & {}^{\lambda}\delta_{\mathrm{icos},2} &= a^2\,{}^{\lambda}\delta_{xx} + b^2\,{}^{\lambda}\delta_{yy} + 2ab\,{}^{\lambda}\delta_{xy},\\
{}^{\lambda}\delta_{\mathrm{icos},3} &= a^2\,{}^{\lambda}\delta_{yy} + b^2\,{}^{\lambda}\delta_{zz} - 2ab\,{}^{\lambda}\delta_{yz}, & {}^{\lambda}\delta_{\mathrm{icos},4} &= a^2\,{}^{\lambda}\delta_{yy} + b^2\,{}^{\lambda}\delta_{zz} + 2ab\,{}^{\lambda}\delta_{yz}, \qquad (14)\\
{}^{\lambda}\delta_{\mathrm{icos},5} &= a^2\,{}^{\lambda}\delta_{zz} + b^2\,{}^{\lambda}\delta_{xx} - 2ab\,{}^{\lambda}\delta_{zx}, & {}^{\lambda}\delta_{\mathrm{icos},6} &= a^2\,{}^{\lambda}\delta_{zz} + b^2\,{}^{\lambda}\delta_{xx} + 2ab\,{}^{\lambda}\delta_{zx}.
\end{aligned}
$$

As before the λ specifies the tensor designation when two or more tensors are to be compared, and the coefficients *a* and *b* are given by: $a = [(5+\sqrt{5})/10]^{1/2}$ and $b = [(5-\sqrt{5})/10]^{1/2}$. Thus, $a^2 = 0.7236$ and $b^2 = 0.2764$. Hence, $a^2 + b^2 = 1$. Furthermore, the angle between any two directions is $\cos^{-1}\sqrt{1/5} \cong 63.4^0$. Using Figure 7 and Eq. 14, the six geometric symmetry shift components for the icosahedrons are given by the transformation matrix *T* from the Cartesian to the icosahedral representations becomes:

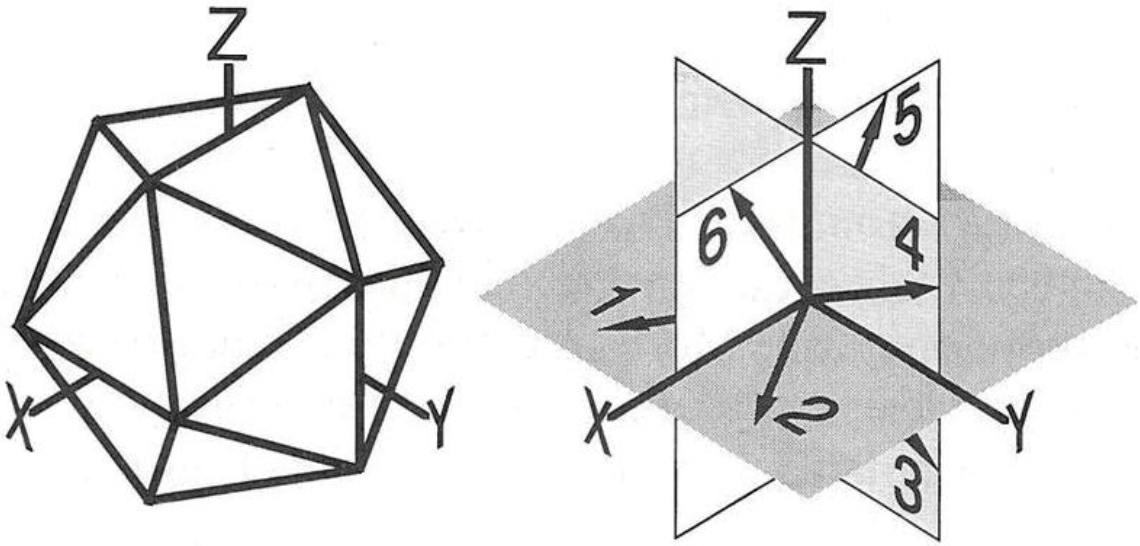

Figure 7. The schematic icosahedral basis of this representation embeds the molecular frame into the object on the left hand side. The right schematic shows the orientation of the various directions relative to the molecular XYZ frame.

$$\begin{pmatrix} {}^{\lambda}\delta_{\text{icosl}} \\ {}^{\lambda}\delta_{\text{icos 2}} \\ {}^{\lambda}\delta_{\text{icos 3}} \\ {}^{\lambda}\delta_{\text{icos 4}} \\ {}^{\lambda}\delta_{\text{icos 5}} \\ {}^{\lambda}\delta_{\text{icos 6}} \end{pmatrix} = T \begin{pmatrix} {}^{\lambda}\delta_{xx} \\ {}^{\lambda}\delta_{yy} \\ {}^{\lambda}\delta_{zz} \\ {}^{\lambda}\delta_{xy} \\ {}^{\lambda}\delta_{yz} \\ {}^{\lambda}\delta_{zx} \end{pmatrix} = \begin{pmatrix} a^2 & b^2 & 0 & -2ab & 0 & 0 \\ a^2 & b^2 & 0 & +2ab & 0 & 0 \\ 0 & a^2 & b^2 & 0 & -2ab & 0 \\ 0 & a^2 & b^2 & 0 & +2ab & 0 \\ b^2 & 0 & a^2 & 0 & 0 & -2ab \\ b^2 & 0 & a^2 & 0 & 0 & +2ab \end{pmatrix} \begin{pmatrix} {}^{\lambda}\delta_{xx} \\ {}^{\lambda}\delta_{yy} \\ {}^{\lambda}\delta_{zz} \\ {}^{\lambda}\delta_{xy} \\ {}^{\lambda}\delta_{yz} \\ {}^{\lambda}\delta_{zx} \end{pmatrix} \tag{15}$$

Note, the icosahedral representation is real and does not require any imaginary terms or complex conjugate manipulations. This representation also avoids the use of phase factors and other complexities found in the irreducible spherical tensor notation. To derive the icosahedral metric, we also need the transpose of the *T* matrix, its inverse, (T^{-1}), and the transpose of T^{-1}. Using standard matrix operations and the transformation matrix given in Eq. 15, one obtains:

$$T^{-1} = \frac{1}{2\left(a^6+b^6\right)} \begin{pmatrix} a^4 & a^4 & -a^2b^2 & -a^2b^2 & b^4 & b^4 \\ b^4 & b^4 & a^4 & a^4 & 0 & 0 \\ -a^2b^2 & -a^2b^2 & b^4 & b^4 & a^4 & a^4 \\ -\left(a^6+b^6\right)/2ab & \left(a^6+b^6\right)/2ab & 0 & 0 & 0 & 0 \\ 0 & 0 & -\left(a^6+b^6\right)/2ab & \left(a^6+b^6\right)/2ab & 0 & 0 \\ 0 & 0 & 0 & 0 & -\left(a^6+b^6\right)/2ab & \left(a^6+b^6\right)/2ab \end{pmatrix} \tag{16}$$

$$T^{-1}_{trsp} = \frac{1}{2\left(a^6+b^6\right)} \begin{pmatrix} a^4 & b^4 & -a^2b^2 & -\left(a^6+b^6\right)/2ab & 0 & 0 \\ a^4 & b^4 & -a^2b^2 & \left(a^6+b^6\right)/2ab & 0 & 0 \\ -a^2b^2 & a^4 & b^4 & 0 & -\left(a^6+b^6\right)/2ab & 0 \\ -a^2b^2 & a^4 & b^4 & 0 & \left(a^6+b^6\right)/2ab & 0 \\ b^4 & -a^2b^2 & a^4 & 0 & 0 & -\left(a^6+b^6\right)/2ab \\ b^4 & -a^2b^2 & a^4 & 0 & 0 & \left(a^6+b^6\right)/2ab \end{pmatrix} \tag{17}$$

Using Eq. 7, Maple obtains the icosahedral metric for $d^2(k)$ as follows:

$$
\begin{aligned}
d^2(k) &= \left({}^2\delta_{\mathrm{Cart},\mu}(k) - {}^1\delta_{\mathrm{Cart},\mu}(k)\right) EP_{\mathrm{Cart},\mu\eta}(\Omega) E\left({}^2\delta_{\mathrm{Cart},\eta}(k) - {}^1\delta_{\mathrm{Cart},\eta}(k)\right), \\
d^2(k) &= \left({}^2\delta_{\mathrm{Cart},\mu}(k) - {}^1\delta_{\mathrm{Cart},\mu}(k)\right) T_{trsp} T_{trsp}^{-1} P_{\mathrm{Cart},\mu\eta}(\Omega) T^{-1} T\left({}^2\delta_{\mathrm{Cart},\eta}(k) - {}^1\delta_{\mathrm{Cart},\eta}(k)\right), \\
d^2(k) &= \left[\left({}^2\delta_{\mathrm{Cart},\mu}(k) - {}^1\delta_{\mathrm{Cart},\mu}(k)\right) T_{trsp}\right]\left[T_{trsp}^{-1} P_{\mathrm{Cart},\mu\eta}(\Omega) T^{-1}\right]\left[T\left({}^2\delta_{\mathrm{Cart},\eta}(k) - {}^1\delta_{\mathrm{Cart},\eta}(k)\right)\right], \\
d^2(k) &= \left({}^2\delta_{\mathrm{icos},\mu}(k) - {}^1\delta_{\mathrm{icos},\mu}(k)\right)\left[P_{\mathrm{icos},\mu\eta}(\Omega)\right]\left({}^2\delta_{\mathrm{icos},\eta}(k) - {}^1\delta_{\mathrm{icos},\eta}\right).
\end{aligned}
\tag{18}
$$

Both icosahedral tensors (${}^1\delta_{\mathrm{icos}}$ or ${}^2\delta_{\mathrm{icos}}$) have identical transformation properties as found in Eq.s. 14 and 15, and $\mu = \eta$. Multiplying expressions and matrices in Equations 14 through 18 yields the metric of the icosahedral representation as follows:

$$
P_{\mathrm{icos}}(\Omega) = T_{\mathrm{trsp}}^{-1} P_{\mathrm{Cart}}(\Omega) T^{-1} = T_{\mathrm{trsp}}^{-1} \begin{pmatrix} 3 & 1 & 1 & 0 & 0 & 0 \\ 1 & 3 & 1 & 0 & 0 & 0 \\ 1 & 1 & 3 & 0 & 0 & 0 \\ 0 & 0 & 0 & 4 & 0 & 0 \\ 0 & 0 & 0 & 0 & 4 & 0 \\ 0 & 0 & 0 & 0 & 0 & 4 \end{pmatrix} T^{-1} = \frac{1}{6} \begin{pmatrix} 1 & 0 & 0 & 0 & 0 & 0 \\ 0 & 1 & 0 & 0 & 0 & 0 \\ 0 & 0 & 1 & 0 & 0 & 0 \\ 0 & 0 & 0 & 1 & 0 & 0 \\ 0 & 0 & 0 & 0 & 1 & 0 \\ 0 & 0 & 0 & 0 & 0 & 1 \end{pmatrix}. \tag{19}
$$

One should note that this icosahedral metric is not only orthogonal (i.e., diagonal) but also every term in $P_{\mathrm{icos}}(\Omega)$ is equally weighted and thus normalized. The metric provides symmetrical weighting of the ${}^2\delta_{\mathrm{icos},\mu}$ vs. ${}^1\delta_{\mathrm{icos},\mu}$ in a least-square plot. This plot greatly simplifies the processing of chemical shift data as it allows one to plot the theoretical vs. the experimental values and obtain $d^2(k)$ or the variance of the fit directly from the least-squares method. Hence, the mean squared distance actually determines the statistical variance for a least-square plot. The $d^2(k)$ for the icosahedral representation and the k^{th} atom then is:

$$d^2(k) = \frac{1}{6}\begin{pmatrix} \left({}^2\delta_1 - {}^1\delta_1\right)\left({}^2\delta_2 - {}^1\delta_2\right)\left({}^2\delta_3 - {}^1\delta_3\right) \\ \left({}^2\delta_4 - {}^1\delta_4\right)\left({}^2\delta_5 - {}^1\delta_5\right)\left({}^2\delta_6 - {}^1\delta_6\right) \end{pmatrix} \begin{pmatrix} 1 & 0 & 0 & 0 & 0 & 0 \\ 0 & 1 & 0 & 0 & 0 & 0 \\ 0 & 0 & 1 & 0 & 0 & 0 \\ 0 & 0 & 0 & 1 & 0 & 0 \\ 0 & 0 & 0 & 0 & 1 & 0 \\ 0 & 0 & 0 & 0 & 0 & 1 \end{pmatrix} \begin{pmatrix} \left({}^2\delta_1 - {}^1\delta_1\right) \\ \left({}^2\delta_2 - {}^1\delta_2\right) \\ \left({}^2\delta_3 - {}^1\delta_3\right) \\ \left({}^2\delta_4 - {}^1\delta_4\right) \\ \left({}^2\delta_5 - {}^1\delta_5\right) \\ \left({}^2\delta_6 - {}^1\delta_6\right) \end{pmatrix}. \quad (20)$$

Expanding Eq. 20 gives the following explicit algebraic expression:

$$d^2(k) = \left(\frac{1}{6}\right)\cdot\left(\left[{}^2\delta_1 - {}^1\delta_1\right]^2 + \left[{}^2\delta_2 - {}^1\delta_2\right]^2 + \left[{}^2\delta_3 - {}^1\delta_3\right]^2 + \left[{}^2\delta_4 - {}^1\delta_4\right]^2 + \left[{}^2\delta_5 - {}^1\delta_5\right]^2 + \left[{}^2\delta_6 - {}^1\delta_6\right]^2 \right). \quad (21)$$

Only single crystal NMR solid measurement techniques allow the determination of all six of these independent components in the icosahedral tensor. Powder methods only provide the three principal Cartesian components lying along the diagonal trace of the tensor found in Eq. 1. This limitation need not be a concern as theoretical calculations provide the tensor's principal orientation angles from nonzero off-diagonal components. Diagonalization of a shielding matrix may then be used to obtain the principal values of the tensor along with three Euler angles for each k^{th} nuclei needed to effect the transformation from the molecular frame to the principal-axis frame. As indicated above only one molecular frame per molecule may be used in CQM calculations. This molecular frame should never be confused with separate principal axes frames for each magnetic nucleus that are indicated by 11, 22 and 33 labels in this work.

The irreducible spherical representation

A conversion between the Cartesian and irreducible spherical representations has been given by Cook and de Lucia.[67] This representation, appearing in Mehring's book,[59]

was constructed for angular momentum using a three j-symbol approach. The spherical components of this transformation are given as follows:

$$\begin{aligned}
\delta_{0,0} &= -\sqrt{1/3}\cdot\left(\delta_{xx}+\delta_{yy}+\delta_{zz}\right) = -\sqrt{3}\cdot\delta_{\text{iso}},\\
\delta_{2,0} &= \sqrt{2/3}\cdot\left(\delta_{zz}-1/2\,\delta_{xx}-1/2\,\delta_{yy}\right),\\
\delta_{2,+2} &= \left[\frac{1}{2}\left(\delta_{xx}-\delta_{yy}\right)+i\delta_{xy}\right],\\
\delta_{2,-2} &= \left[\frac{1}{2}\left(\delta_{xx}-\delta_{yy}\right)-i\delta_{xy}\right],\\
\delta_{2,+1} &= -\left[\delta_{zx}+i\delta_{yz}\right],\\
\delta_{2,-1} &= \left[\delta_{zx}-i\delta_{yz}\right].
\end{aligned} \tag{22}$$

where the invariant zero rank term, in the molecular frame, has a (-1) phase angle and δ_{iso} is given by the trace of diagonal values:

$$\delta_{\text{iso}} = \frac{1}{3}\left(\delta_{xx}+\delta_{yy}+\delta_{zz}\right). \tag{23}$$

This term along with two additional composite shift values will be discussed in more detail in a section on tensor principle values below.

To remove a normalization problem in Eq. 22, it is necessary to convert the irreducible spherical components from an angular momentum basis to one that normalizes the mean squared deviation, $d^2(k)$. Cook and de Lucia[67] warned that the general transformations in Eq. 22, which apply to several types of electrical and magnetic properties, may need to be renormalized depending upon the physical property and/or interaction that an investigator is seeking. They did not treat the shielding tensor or its metric explicitly and gave only generalized normalization factors important to three j-symbols that characterize angular momentum. For convenience in preserving the historical derivation of Cook and de Lucia,[67] additional renormalization constants (i.e.,

Λ_0 and Λ_2) are added to Eq. 22 for $\ell = 0$ and $\ell = 2$.. Further, the real and imaginary components are also separated as follows:

$$
\begin{aligned}
\delta_{\mathrm{Re}\,0,0} &= -\sqrt{1/3}\cdot\Lambda_0\cdot\left(\delta_{xx}+\delta_{yy}+\delta_{zz}\right) = -\sqrt{3}\cdot\Lambda_0\cdot\delta_{\mathrm{iso}},\\
\delta_{\mathrm{Re}\,2,0} &= \sqrt{2/3}\cdot\Lambda_2\cdot\left(\delta_{zz}-\tfrac{1}{2}\delta_{xx}-\tfrac{1}{2}\delta_{yy}\right),\\
\delta_{\mathrm{Re}\,2,2} &= \Lambda_2\cdot\sqrt{1/2}\left(\delta_{2,+2}+\delta_{2,-2}\right) = \Lambda_2\cdot\sqrt{1/2}\left(\delta_{xx}-\delta_{yy}\right),\\
\delta_{\mathrm{Im}\,2,2} &= \Lambda_2\cdot\sqrt{1/2}\left(\delta_{2,+2}-\delta_{2,-2}\right) = \Lambda_2\cdot\sqrt{2}i\delta_{xy},\\
\delta_{\mathrm{Im}\,2,1} &= \Lambda_2\cdot\sqrt{1/2}\left(\delta_{2,+1}+\delta_{2,-1}\right) = -\Lambda_2\cdot\sqrt{2}i\delta_{yz},\\
\delta_{\mathrm{Re}\,2,1} &= \Lambda_2\cdot\sqrt{1/2}\left(\delta_{2,+1}-\delta_{2,-1}\right) = -\Lambda_2\cdot\sqrt{2}\delta_{zx}.
\end{aligned}
\tag{24}
$$

The $\sqrt{1/2}$ associated with $\left(\delta_{2,+2}\pm\delta_{2,-2}\right)$ and $\left(\delta_{2,+1}\pm\delta_{2,-1}\right)$ may be rationalized on the basis of propagation of errors for sums and differences in mean squared deviations, *msd*. (Consider the sum, $\Sigma = \delta_{2,2} + \delta_{2,-2}$; standard error propagation techniques for treating a sum of squared starts with: $\Sigma_{error}{}^2 = \frac{1}{4}\left(\delta xx-\delta yy\right)^2 + \frac{1}{4}\left(\delta xx-\delta yy\right)^2 = ½(\delta_{xx}-\delta_{yy})^2$ Taking the square root of both sides yields rms of $\Sigma_{error} = \sqrt{1/2}\left(\delta xx-\delta yy\right)$. Analogous expressions also exist for δ_{xy}, δ_{yz}, δ_{zx}. Substitution of $\sqrt{1/2}$ for both sum and differences into Eq. 24 separates real and imaginary spherical tensor components and provides the desired transformation matrix. The explicit connection between rms error analysis and d^2 in the chemical shift metrics is obvious.) The ($\delta_{2,+2}$, $\delta_{2,-2}$, $\delta_{2,+1}$, $\delta_{2,-1}$) terms in Equations 22 and 24 are converted into real and imaginary terms to separate, respectively, the diagonal and off-diagonal Cartesian shift components. This mathematical operation will allow one to deal better with shift data in principal axis

frames. Composing a matrix transformation from Eq. 24, yields the following transformation matrix, *T*:

$$\begin{pmatrix} \delta_{\mathrm{Re}\,0,0} \\ \delta_{\mathrm{Re}\,2,0} \\ \delta_{\mathrm{Re}\,2,2} \\ \delta_{\mathrm{Im}\,2,2} \\ \delta_{\mathrm{Im}\,2,1} \\ \delta_{\mathrm{Re}\,2,1} \end{pmatrix} = T \begin{pmatrix} \delta_{xx} \\ \delta_{yy} \\ \delta_{zz} \\ \delta_{xy} \\ \delta_{zx} \\ \delta_{yz} \end{pmatrix} = \begin{pmatrix} -\sqrt{1/3}\Lambda_0 & -\sqrt{1/3}\Lambda_0 & -\sqrt{1/3}\Lambda_0 & 0 & 0 & 0 \\ -\sqrt{1/6}\Lambda_2 & -\sqrt{1/6}\Lambda_2 & \sqrt{2/3}\Lambda_2 & 0 & 0 & 0 \\ \sqrt{1/2}\Lambda_2 & -\sqrt{1/2}\Lambda_2 & 0 & 0 & 0 & 0 \\ 0 & 0 & 0 & \sqrt{2}\Lambda_2 i & 0 & 0 \\ 0 & 0 & 0 & 0 & -\sqrt{2}\Lambda_2 i & 0 \\ 0 & 0 & 0 & 0 & 0 & -\sqrt{2}\Lambda_2 \end{pmatrix} \begin{pmatrix} \delta_{xx} \\ \delta_{yy} \\ \delta_{zz} \\ \delta_{xy} \\ \delta_{yz} \\ \delta_{zx} \end{pmatrix} . \quad (25)$$

The correction terms in Eq. 24 provide an overall metric that normalizes the mean squared deviation, not angular momentum, providing a metric in which variance is correctly predicted by the scatter in an irreducible spherical least-square plot of shielding vs. shifts (see below).

Eq. 24 forms the basis for expressing the irreducible spherical shift components in matrix form using the transformation matrix, *T*, given in Eq. 25. Continuing to develop Eq. 7, using two ${}^{\lambda}\delta_{\mathrm{IrrSph}}$ shift tensors (λ=1,2) yields the following equations in matrix form:

$$\begin{aligned} d^2(k) &= \sum_{\mu,\eta} \left({}^2\delta_{\mathrm{Cart},\mu} - {}^1\delta_{\mathrm{Cart},\mu} \right)^* \cdot E \cdot P_{\mathrm{Cart},\mu\eta}(\Omega) \cdot E \cdot \left({}^2\delta_{\mathrm{Cart},\eta} - {}^1\delta_{\mathrm{Cart},\eta} \right), \\ d^2(k) &= \sum_{\mu,\eta} \left({}^2\delta_{\mathrm{Cart},\mu} - {}^1\delta_{\mathrm{Cart},\mu} \right)^* T^*_{trsp} T^{-1*}_{trsp} P_{\mathrm{Cart},\mu\eta}(\Omega) T^{-1} T \left({}^2\delta_{\mathrm{Cart},\eta} - {}^1\delta_{\mathrm{Cart},\eta} \right), \\ d^2(k) &= \sum_{\mu,\eta} \left({}^2\delta_{\mathrm{IrrSph},\mu} - {}^1\delta_{\mathrm{IrrSph},\mu} \right)^* \left[T^{-1*}_{trsp} P_{\mathrm{Cart},\mu\eta}(\Omega) T^{-1} \right] \left({}^2\delta_{\mathrm{IrrSph},\eta} - {}^1\delta_{\mathrm{IrrSph},\eta} \right), \\ d^2(k) &= \sum_{\mu,\eta} \left({}^2\delta_{\mathrm{IrrSph},\mu} - {}^1\delta_{\mathrm{IrrSph},\mu} \right)^* \left[P_{\mathrm{IrrSph},\mu\eta}(\Omega) \right] \left({}^2\delta_{\mathrm{IrrSph},\eta} - {}^1\delta_{\mathrm{IrrSph},\eta} \right), \end{aligned} \quad (26)$$

where *E* is the identity matrix. Once again if one wishes to compare a theoretical shielding with an experimental shift, it is necessary to relate the compared tensors with a negative slope, m ≈ –1, and an adjustments for the constant TMS reference: $\sigma_{\mathrm{IrrSph},\mu}$ =

m·$\delta_{\text{IrrSph},\mu}$+ δ_{TMS}. Note, the conjugate transpose of the inverse $\left(\text{i.e., } T_{\text{trsp}}^{-1*}\right)$ is required for $d^2(k)$ to be real and to conform with the row and column vectors used in the derivation of $P_{\text{IrrSph}}(\Omega)$. Eq. 26 also provides the relationship between the metric tensors in two different representations as follows:

$$P_{\text{IrrSph}}(\Omega) = T_{\text{trsp}}^{-1*} P_{\text{Cart}}(\Omega) T^{-1}. \tag{27}$$

The corresponding values and form of T^{-1} and T_{trsp}^{-1*}, are provided in Eq. 28. They are of the same form for any two tensors to be compared.

$$T^{-1} = \begin{pmatrix} -1/\sqrt{3}\Lambda_0 & -1/\sqrt{6}\Lambda_2 & 1/\sqrt{2}\Lambda_2 & 0 & 0 & 0 \\ -1/\sqrt{3}\Lambda_0 & -1/\sqrt{6}\Lambda_2 & -1/\sqrt{2}\Lambda_2 & 0 & 0 & 0 \\ -1/\sqrt{3}\Lambda_0 & 2/\sqrt{6}\Lambda_2 & 0 & 0 & 0 & 0 \\ 0 & 0 & 0 & -i/\sqrt{2}\Lambda_2 & 0 & 0 \\ 0 & 0 & 0 & 0 & i/\sqrt{2}\Lambda_2 & 0 \\ 0 & 0 & 0 & 0 & 0 & -1/\sqrt{2}\Lambda_2 \end{pmatrix}$$

$$T_{\text{trsp}}^{-1*} = \begin{pmatrix} -1/\sqrt{3}\Lambda_0 & -1/\sqrt{3}\Lambda_0 & -1/\sqrt{3}\Lambda_0 & 0 & 0 & 0 \\ -1/\sqrt{6}\Lambda_2 & -1/\sqrt{6}\Lambda_2 & 2/\sqrt{6}\Lambda_2 & 0 & 0 & 0 \\ 1/\sqrt{2}\Lambda_2 & -1/\sqrt{2}\Lambda_2 & 0 & 0 & 0 & 0 \\ 0 & 0 & 0 & i/\sqrt{2}\Lambda_2 & 0 & 0 \\ 0 & 0 & 0 & 0 & -i/\sqrt{2}\Lambda_2 & 0 \\ 0 & 0 & 0 & 0 & 0 & -1/\sqrt{2}\Lambda_2 \end{pmatrix} \tag{28}$$

We may now obtain the metric for the irreducible spherical tensors with the renormalized corrective term included. Using Equations 27 and 28, the metric tensor for the separated real and imaginary irreducible spherical matrix is derived with Maple, as follows:

$$P_{\text{IrrSph}}(\Omega)=\frac{1}{15}\left[T_{trsp}^{-1*}P_{\text{Cart}}(\Omega)T^{-1}\right]=\frac{1}{15}\cdot\begin{pmatrix}\left(5/\Lambda_0^2\right) & 0 & 0 & 0 & 0 & 0\\ 0 & \left(2/\Lambda_2^2\right) & 0 & 0 & 0 & 0\\ 0 & 0 & \left(2/\Lambda_2^2\right) & 0 & 0 & 0\\ 0 & 0 & 0 & \left(2/\Lambda_2^2\right) & 0 & 0\\ 0 & 0 & 0 & 0 & \left(2/\Lambda_2^2\right) & 0\\ 0 & 0 & 0 & 0 & 0 & \left(2/\Lambda_2^2\right)\end{pmatrix} \tag{29}$$

Each term in the metric tensor is now normalized to 1/3 so that $d^2(k)$ is calibrated for a single nucleus of three principle shift values. This is done by setting $\Lambda_0 = -1$ for $\ell = 0$ and $\Lambda_2 = \sqrt{2/5}$ for $\ell = 2$. While the -1 phase factor in Eq. 22 for angular momentum (defined classically with moments of inertia and angular rotational velocity) would have purpose if a rotational position is indexed, they have no relevance in a mean squared deviation as negative phase factors are excluded by the squaring procedure in the metric definition. Hence, we arbitrarily employ the minus sign for the square root of Λ_0^2 to eliminate this phase complexity (It may be shown that the phase factor, whether + 1 or – 1, has no consequence on the results). Except for the phase factor, the renormalization term for both Λ_0 and Λ_2 may be written in the same Legendre polynomial form as $\Lambda_1 = \sqrt{\ell!/2\ell+1}$; and Eq. 29 now becomes:

$$P_{\text{IrrSph}}(\Omega)=\frac{1}{3}\cdot\begin{pmatrix}1&0&0&0&0&0\\0&1&0&0&0&0\\0&0&1&0&0&0\\0&0&0&1&0&0\\0&0&0&0&1&0\\0&0&0&0&0&1\end{pmatrix} \tag{30}$$

Introducing the renormalized terms in the Irreducible Spherical tensors now converts Eq. 25 to:

$$
\begin{aligned}
\delta_{\mathrm{Re}\,0,0} &= \sqrt{1/3}\cdot\left(\delta_{xx}+\delta_{yy}+\delta_{zz}\right)=\sqrt{3}\cdot\delta_{\mathrm{iso}},\\
\delta_{\mathrm{Re}\,2,0} &= \sqrt{4/15}\cdot\left(\delta_{zz}-1/2\,\delta_{xx}-1/2\,\delta_{yy}\right),\\
\delta_{\mathrm{Re}\,2,2} &= \sqrt{1/5}\cdot\left(\delta_{2,+2}+\delta_{2,-2}\right)=\sqrt{1/5}\cdot\left(\delta_{xx}-\delta_{yy}\right),\\
\delta_{\mathrm{Im}\,2,2} &= \sqrt{1/5}\cdot\left(\delta_{2,+2}-\delta_{2,-2}\right)=\sqrt{4/5}\cdot i\delta_{xy},\\
\delta_{\mathrm{Im}\,2,1} &= \sqrt{1/5}\cdot\left(\delta_{2,+1}+\delta_{2,-1}\right)=-\sqrt{4/5}\cdot i\delta_{yz},\\
\delta_{\mathrm{Re}\,2,1} &= \sqrt{1/5}\cdot\left(\delta_{2,+1}-\delta_{2,-1}\right)=-\sqrt{4/5}\cdot\delta_{zx}.
\end{aligned}
\tag{31}
$$

Expanding the last line of Eq. 26 gives explicit algebraic expressions for $d^2(k)$ for the k^{th} magnetic nucleus.

$$
d^2(k)=\left(\frac{1}{3}\right)\left\{\begin{array}{l}
3\left({}^2\delta_{0,0}-{}^1\delta_{0,0}\right)^2+\frac{2}{5}\left(\sqrt{\frac{2}{3}}\,{}^2\delta_{\mathrm{Re}2,0}-\sqrt{\frac{2}{3}}\,{}^1\delta_{\mathrm{Re}2,0}\right)^2+\frac{2}{5}\left(\sqrt{\frac{1}{2}}\,{}^2\delta_{\mathrm{Re}2,2}-\sqrt{\frac{1}{2}}\,{}^1\delta_{\mathrm{Re}2,2}\right)^2\\
+\frac{2}{5}\left(+i\sqrt{2}\,{}^2\delta_{\mathrm{Im}2,2}-i\sqrt{2}\,{}^1\delta_{\mathrm{Im}2,2}\right)^2+\frac{2}{5}\left(-i\sqrt{2}\,{}^2\delta_{\mathrm{Im}2,1}+i\sqrt{2}\,{}^1\delta_{\mathrm{Im}2,1}\right)^2+\frac{2}{5}\left(-\sqrt{2}\,{}^2\delta_{\mathrm{Re}2,1}+\sqrt{2}\,{}^1\delta_{\mathrm{Re}2,1}\right)^2
\end{array}\right\}
\tag{32}
$$

$$
\begin{aligned}
d^2(k)=&\left({}^2\delta_{0,0}-{}^1\delta_{0,0}\right)^2+\frac{4}{45}\left({}^2\delta_{\mathrm{Re}2,0}-{}^1\delta_{\mathrm{Re}2,0}\right)^2+\frac{1}{15}\left({}^2\delta_{\mathrm{Re}2,2}-{}^1\delta_{\mathrm{Re}2,2}\right)^2\\
&+\frac{4}{15}\left(-{}^2\delta_{\mathrm{Im}2,2}+{}^1\delta_{\mathrm{Im}2,2}\right)^2+\frac{4}{15}\left({}^2\delta_{\mathrm{Im}2,1}-{}^1\delta_{\mathrm{Im}2,1}\right)^2+\frac{4}{15}\left(-{}^2\delta_{\mathrm{Re}2,1}+{}^1\delta_{\mathrm{Re}2,1}\right)^2.
\end{aligned}
$$

We have now obtained the two orthonormal irreducible representations for the icosahedral and spherical symmetries, respectively in the molecular frame. One always obtains these results from theoretical shielding results; to obtain experimental results on complete chemical shift tensors, single crystal data must be secured. As most solid-state NMR data derive from microcrystalline powders, we now focus on principal axis frames and powder methods.

Metric Matrices for Chemical-Shift Representations in the Principal Axis Frame

Cartesian Representation

To express the Cartesian shift tensor in the principal-axis frame, it is convenient to use a sequential numeric designation from high to low frequency, i.e., $(\delta_{11}) \geq (\delta_{22}) \geq (\delta_{33})$ to indicate the order of the three principal-axis components lying on the diagonal of the shift tensor. Simultaneously, all off diagonal terms become zero (i.e., $\delta_{xy} = \delta_{yz} = \delta_{zx}$). As the principal components in the Cartesian frame are apolar, one is free, in fact obligated, to pair up the molecular x,y,z labels with the positional numeric indices in a manner consistent with the molecular model. It is not possible to use x,y,z labels simultaneously for both molecular and spectral rank order. Using the μ^{th} pair of tensors, given by ${}^{2}\delta_{\mu}$ and ${}^{1}\delta_{\mu}$, one obtains mean squared distance in the principal value Cartesian representation from Eq. 13:

$$d^2(k) = \frac{1}{15} \cdot \left\{ \begin{array}{l} 3\left({}^{2}\delta_{11} - {}^{1}\delta_{11}\right)^2 + 3\left({}^{2}\delta_{22} - {}^{1}\delta_{22}\right)^2 + 3\left({}^{2}\delta_{33} - {}^{1}\delta_{33}\right)^2 \\ 2\left({}^{2}\delta_{11} - {}^{1}\delta_{11}\right)\left({}^{2}\delta_{22} - {}^{1}\delta_{22}\right) + 2\left({}^{2}\delta_{22} - {}^{1}\delta_{22}\right)\left({}^{2}\delta_{33} - {}^{1}\delta_{33}\right) \\ +2\left({}^{2}\delta_{33} - {}^{1}\delta_{33}\right)\left({}^{2}\delta_{11} - {}^{1}\delta_{11}\right) \end{array} \right\}. \qquad (33)$$

Icosahedral Representation

Setting $\delta_{xy} = \delta_{yz} = \delta_{zx} = 0$ in Eq. 14 leaves only three unique terms for the icosahedral tensors, ${}^{\lambda}\delta_{\mathrm{icos},\mu}$:

$$\begin{aligned} {}^{\lambda}\delta_{\mathrm{icos},1} \equiv {}^{\lambda}\delta_{\mathrm{icos},2} &= a^2\delta_{11} + b^2\delta_{22}, \\ {}^{\lambda}\delta_{i\cos,3} \equiv {}^{\lambda}\delta_{i\cos,4} &= a^2\delta_{22} + b^2\delta_{33}, \\ {}^{\lambda}\delta_{i\cos,5} \equiv {}^{\lambda}\delta_{i\cos,6} &= a^2\delta_{33} + b^2\delta_{11}. \end{aligned} \qquad (34)$$

Using Eq. 34 the algebraic expression, given by Eq. 20, becomes:

$$d^2(k) = \frac{1}{6}\cdot\left(+2\left[{}^2\delta_{\mathrm{icos},1} - {}^1\delta_{\mathrm{icos},1}\right]^2 + 2\left[{}^2\delta_{\mathrm{icos},3} - {}^1\delta_{\mathrm{icos},3}\right]^2 + 2\left[{}^2\delta_{\mathrm{icos},5} - {}^1\delta_{\mathrm{icos},5}\right]^2\right)$$
$$= \frac{1}{3}\cdot\left(\left[{}^2\delta_{\mathrm{icos},1} - {}^1\delta_{\mathrm{icos},1}\right]^2 + \left[{}^2\delta_{\mathrm{icos},3} - {}^1\delta_{\mathrm{icos},3}\right]^2 + \left[{}^2\delta_{\mathrm{icos},5} - {}^1\delta_{\mathrm{icos},5}\right]^2\right). \quad (35)$$

Irreducible Spherical Representation

Aside from the Cartesian and Icosahedral representations just discussed, the remaining examples are either irreducible or related Spherical tensor cases. Table 1 summarizes the common uses. All four sets of spherically related shift components are quite similar to one another, and data in any given set may be used to calculate the remaining three. Even so, only the last two sets have the orthogonality necessary to make least-squares plots of theoretical shieldings vs. experimental shifts. The lattice models from CQM calculations of shieldings are the basis of determining molecular structures from shift measurements. The traditional form[58] is ideal for cylindrically symmetric ellipsoids when the asymmetry term is zero ($\eta = 0$). Otherwise, the flexible anisotropy definition for prolate and oblate symmetry may at times lead to ambiguity, for novices, with this historical convention. The Mehring[59] formalism is the basis for this work and with proper normalization yields a mathematically correct analysis. It only lacks the intuitive concept of span (δ_{span}) proposed by Mason[68] and deviation from centro-symmetric (i.e., acentricity, δ_{acent}) proposed in this work.[3] We feel this orthogonal notation provides a desirable conceptual way to discuss the spectral features of powder bands and their spinning sideband patterns. Further, it is easy to normalize the set and provides a statistical foundation for structural studies. Interestingly the Mason convention closely identifies with the one used in this work because $\delta_{\mathrm{acent}} = \kappa\Omega/2$.

Table 1. Irreducible or related spherical tensors[69]

	Isotropic	Anisotropy, Skew, Acentricity	Asymmetry, Span
Traditional[58]	$\delta_{iso} = \frac{1}{3}\left(\delta_{11} + \delta_{22} + \delta_{33}\right)$	Prolate elipsoid $\delta_{aniso} = \delta_{11} - \frac{1}{2}\left(\delta_{22} + \delta_{33}\right) = \frac{3}{2}\varsigma$ Oblate elipsoid $\delta_{aniso} = \delta_{33} - \frac{1}{2}\left(\delta_{11} + \delta_{22}\right) = \frac{3}{2}\varsigma$	Asymmetry $\eta = \frac{\left(\delta_{22} - \delta_{33}\right)}{\varsigma}$ $\eta = \frac{\left(\delta_{11} - \delta_{22}\right)}{\varsigma}$
Mason[68]	$\delta_{iso} = \frac{1}{3}\left(\delta_{11} + \delta_{22} + \delta_{33}\right)$	skew $\kappa = \frac{2\,\delta_{22} - \left(\delta_{11} + \delta_{33}\right)}{\Omega}$	$\delta_{span} = \left(\delta_{11} - \delta_{33}\right) = \Omega$
Mehring[59]	$\delta_{iso} = \frac{1}{3}\left(\delta_{11} + \delta_{22} + \delta_{33}\right)$	$\delta_{aniso} = \delta_{11} - \frac{1}{2}\left(\delta_{22} + \delta_{33}\right)$	$\delta_{asym} = \left(\delta_{11} - \delta_{22}\right) = \delta_{Re2,\,2}$
This work[3]	$\delta_{iso} = \frac{1}{3}\left(\delta_{11} + \delta_{22} + \delta_{33}\right)$	$\delta_{aniso} = \delta_{22} - \frac{1}{2}\left(\delta_{11} + \delta_{33}\right)$	$\delta_{span} = \left(\delta_{11} - \delta_{33}\right)$

Thus, in the principal axis frame, the irreducible spherical representation including renormalization yields the following definitions:

$$\begin{aligned} \delta_{0,0}(k) &= N_{\text{iso}}\ \delta_{\text{iso}}(k) &&= \sqrt{3}\ (\delta_{11}+\delta_{22}+\delta_{33})/3, \\ \delta_{2,0}(k) &= N_{\text{acent}}\ \delta_{\text{acent}}(k) &&= \sqrt{4/15}\ (\delta_{22}-\tfrac{1}{2}\delta_{11}-\tfrac{1}{2}\delta_{33}), \\ \delta_{\text{Re}2,2}(k) &= N_{\text{span}}\ \delta_{\text{span}}(k) &&= \sqrt{1/5}\ (\delta_{11}-\delta_{33}). \end{aligned} \tag{36}$$

where the normalization constants are given by: $N_{\text{iso}} = \sqrt{3}$, $N_{\text{acent}} = \sqrt{4/15}$, and $N_{\text{span}} = \sqrt{1/5}$. The distance in the principal axis frames for the irreducible spherical representation is readily adapted from Eq. 32 by setting ${}^{\lambda}\delta_{xy} = {}^{\lambda}\delta_{yz} = {}^{\lambda}\delta_{zx} = 0$, and is given as follows:

$$d^2(k) = \tfrac{1}{3}\cdot\left(\sigma_{\text{iso}} + m\cdot\delta_{\text{iso}} - \sigma_{\text{TMS}}\right)^2 + \tfrac{4}{45}\cdot\left(\sigma_{\text{acent}} + m\cdot\delta_{\text{acent}}\right)^2 + \tfrac{1}{15}\cdot\left(\sigma_{\text{span}} + m\cdot\delta_{\text{span}}\right)^2. \tag{37}$$

Once again, Eq. 37 uses a matching shielding tensor, σ_{μ} to it's shift pair, $-\delta_{\mu}$. Both σ and δ have the same transformation properties, except that both the shielding components and shift components must be referenced to the same fiducial constant and the negative correlation, m = -1, between the two representations properly adjusted.

The orthogonality of the irreducible spherical and icosahedral representations make it easy to make respective plots of ${}^{2}\delta_{\mu}$ vs. ${}^{1}\delta_{\mu}$. Conversely, the lack of orthogonality in the metric analysis makes Cartesian tensor components unsuitable statistically for a least-squares plot of two sets of shift components. A proper Cartesian Metric exists (see, Eq. 11) and yields an identical $d^2(k)$ value to that of the irreducible spherical and icosahedral metrics. However, least-square plots of Cartesian quantities and their statistical packages for obtaining the variance of the fit fail to construct the cross terms needed in the analysis. An increased visual scatter is noted in these plots and the standard deviation may be about 50% larger (exhibiting a factor of approximately two

in the statistical variance). This discrepancy reflects nothing more than an inadequate rendition of the data in the plot and the inaccuracies bias the development of molecular structure from calculated Cartesian chemical shifts used in NMR crystallography.

The icosahedral metric is easy to use because of the ease and simplicity with which it can be assembled from the corresponding Cartesian tensor components. Furthermore, the self normalizing nature of the icosahedral metric for both principal and non-principal value data is appealing. The one very attractive feature of the irreducible spherical representation is the invariance of the zero rank *isotropic* shift term which is invariant under rotation whether it is molecular tumbling in a liquid or undergoing mechanical turning or spinning in a solid. This feature allows the use of high speed spinning to improve the calibration of shift scales and the determination of theoretical shielding and experimental shift offsets. As the two scales run in opposite frequency directions, the shielding must first be expressed with a common reference shift (*infra supra*) and be compatible with the shift components. This requires that the shielding field corresponding to the shift references be known in both scales and that m = -1. We now give some examples of the use of different representations and their metrics to illustrate the benefits and problems encountered in the use of metrics.

Examples of Metrics for Chemical-Shift Representations with Principal Axis Components

^{13}C Shift Tensors in *p*-Dimethoxybenzene

Our examples focus on the four unique ^{13}C shift tensors in *p*-dimethoxybenzene. A schema is given for this molecule in Figure 8. This compound was chosen because we have tensors, from 1988,[70] that were obtained using single crystal data. Recently new

powder shift data and the very latest theoretical results on this molecule have become available, which link better the tensor shifts with x-ray molecular structure. With this data base one may illustrate experimental vs. experimental comparisons as well as theoretical vs. experimental correlations. Experimental and theoretical data are contained in Table 2. The experimental tensor components are for powdered multicrystalline samples, ${}^{1}\delta_{\mu}$, and for single crystal samples, ${}^{2}\delta_{\mu}$.

The theoretical components, σ_{μ}, are constants that are recorded as shielding instead of shift values. It should be stressed that these two scales increase in opposite directions and are related by a line that has a correlation slope of m = –1. Further, to determine the mean distance squared one must relate explicitly the two tensors to the same reference nucleus. *p*-Dimethoxybenzene is a relatively small molecule with diffraction structural data that are relatively easy to optimize quantum mechanically. Thus, reasonably good CQM refined structures of the x-ray results are readily available. The absence of a permanent molecular dipole significantly reduces long range electrostatic forces, and this minimizes intermolecular shielding errors in theoretical results calculated only on isolated molecules.

Columns 2 and 5 in Table 2 are experimental powder and single crystal data, respectively. These are changed into Icosahedral and Irreducible Sherical representation in the following columns. Column 8 contains the theoretical shielding components which are changed into theoretical shifts with the TMS shielding value and a minus 1 on the shielding components. By using scaled shift values one avoids considerable complexity in constructing the Scaled Icosahedral shifts and Scaled Spherical representations.

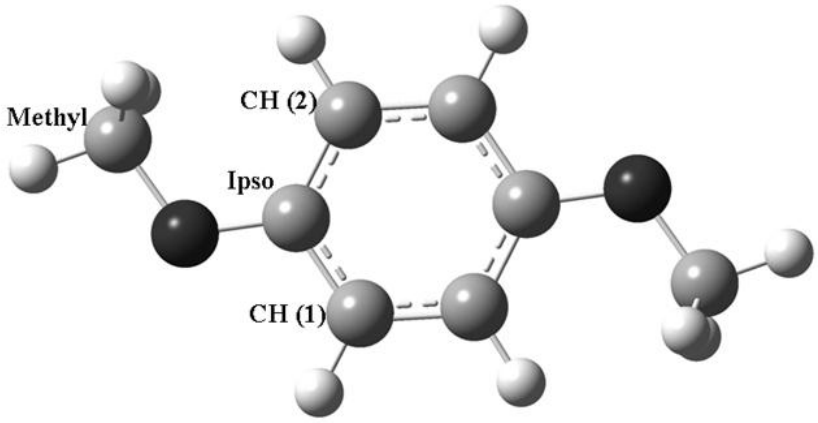

Figure 8. Schema for *p*-Dimethoxybenzene.

Table 2. The database used in the examples

Atom	Experimental						Theory			
	Powder Microcrystals			Single Crystal						
	Cartesian	Icosahedral	Irreducible Spherical	Cartesian	Icosahedral	Irreducible Spherical	Cartesian	Scaled Cartesian	Scaled Icosahedral	Scaled Irred. Spher.
Key	$^{1}\delta_{11}$ $^{1}\delta_{22}$ $^{1}\delta_{33}$	$^{1}\delta_{icos,1}$ $^{1}\delta_{icos,3}$ $^{1}\delta_{icos,5}$	$N_{iso}{}^{1}\delta_{iso}$ $N_{ace}{}^{1}\delta_{ace}$ $N_{span}{}^{1}\delta_{span}$	$^{2}\delta_{11}$ $^{2}\delta_{22}$ $^{2}\delta_{33}$	$^{2}\delta_{icos,1}$ $^{2}\delta_{icos,3}$ $^{2}\delta_{icos,5}$	$N_{iso}{}^{2}\delta_{iso}$ $N_{ace}{}^{2}\delta_{ace}$ $N_{span}{}^{2}\delta_{span}$	σ_{11} σ_{22} σ_{33}	$^{th}\delta_{11} = \sigma_{TMS}-\sigma_{11}$ $^{th}\delta_{22} = \sigma_{TMS}-\sigma_{22}$ $^{th}\delta_{33} = \sigma_{TMS}-\sigma_{33}$	$^{th}\delta_{icos,1}$ $^{th}\delta_{icos,3}$ $^{th}\delta_{icos,5}$	$N_{iso}{}^{th}\delta_{iso}$ $N_{ace}{}^{th}\delta_{ace}$ $N_{span}{}^{th}\delta_{span}$
Methyl	77.7 67.8 12.7	75.0 52.6 30.7	91.3 11.7 29.1	80.0 72.0 13.0	77.8 55.7 31.5	95.3 13.2 30.0	103.1 110.0 179.4	81.9 75.0 5.6	80.0 55.9 26.7	93.9 16.2 34.1
Ipso	230.8 156.5 68.7	210.3 132.2 113.5	263.3 3.5 72.5	232.0 159.0 70.0	211.8 134.4 114.8	266.2 4.1 72.4	-36.1 23.5 120.8	221.1 161.5 64.2	204.6 134.6 107.6	258.0 9.7 70.2
Ortho-1	196.6 129.6 20.9	178.1 99.6 69.4	200.4 10.8 78.6	200.0 131.0 22.0	180.9 100.9 71.2	203.8 10.3 79.6	-12.3 61.1 164.6	197.3 123.9 20.4	177.0 95.3 69.3	197.2 7.8 79.1
Ortho-2	189.6 135.7 5.4	174.7 99.7 56.3	190.9 19.8 82.4	193.0 137.0 6.0	177.5 100.8 57.7	194.0 19.4 83.6	-5.3 62.8 178.7	190.3 122.2 6.3	171.5 90.2 57.1	184.1 12.4 82.3

The values for $N_{iso}=\sqrt{(4/15)}$ and $N_{span}=\sqrt{(1/5)}$ are found in Eq. 36. Note, the value of $\delta_{TMS}=0$ is implicite, but $\sigma_{TMS}\approx 185$ ppm.

Comparing Two Experimental Tensors

In Figure 9 we compare the single crystal and powder FIREMAT experimental data using Cartesian, icosahedron and irreducible spherical representations. Even though only the latter two cases exhibit orthogonal character, all representations yield identical values for $d^2(k)$ in all four k nuclei. Thus, the average distance squared value for the whole molecule is the same in spite of the considerable diversity in $d(k)$ for all four atomic tensors. All 12 data points are used without statistical massaging because of the excellent correlation of the two sets. Hence, all 12 degrees of freedom are taken into the treatment of the variance of the least-squares fit. Both sets of data are referenced to TMS with a variety of reference values that cluster around zero within rounding errors (1.2, 0.2 and 1.6 ppm). The correlation slopes exhibit a near perfect relationship relative to unity (1.01, 1.01 and 1.00); and the R^2 correlation coefficients are 0.9998, 0.9999 and 0.9998, respectively. These statistical parameters are given in Figure 9 and in Table 2. The legend in Figure 9 is quite complete and describes this graph accordingly.

From earlier single crystal measurements,[71] a standard error of 0.3 to 0.7 ppm was estimated for the precision of single crystal measurements. The remainders, whatever they may be, derive from the FIREMAT powder data. As single crystal tensor components are all determined from frequency data they likely are more intrinsically accurate than FIREMAT data, which are acquired from the less accurate intensity of the spinning sidebands employed in the FIREMAT experiment. It should be remembered that proportion of intramolecular and intermolecular shifts would be the same for both experimental sets of tensors and hence cannot be used to explain the discrepancies. The four $d^2(k)$ values for p-dimethoxybenzene are given in Figure 9. An average of the four

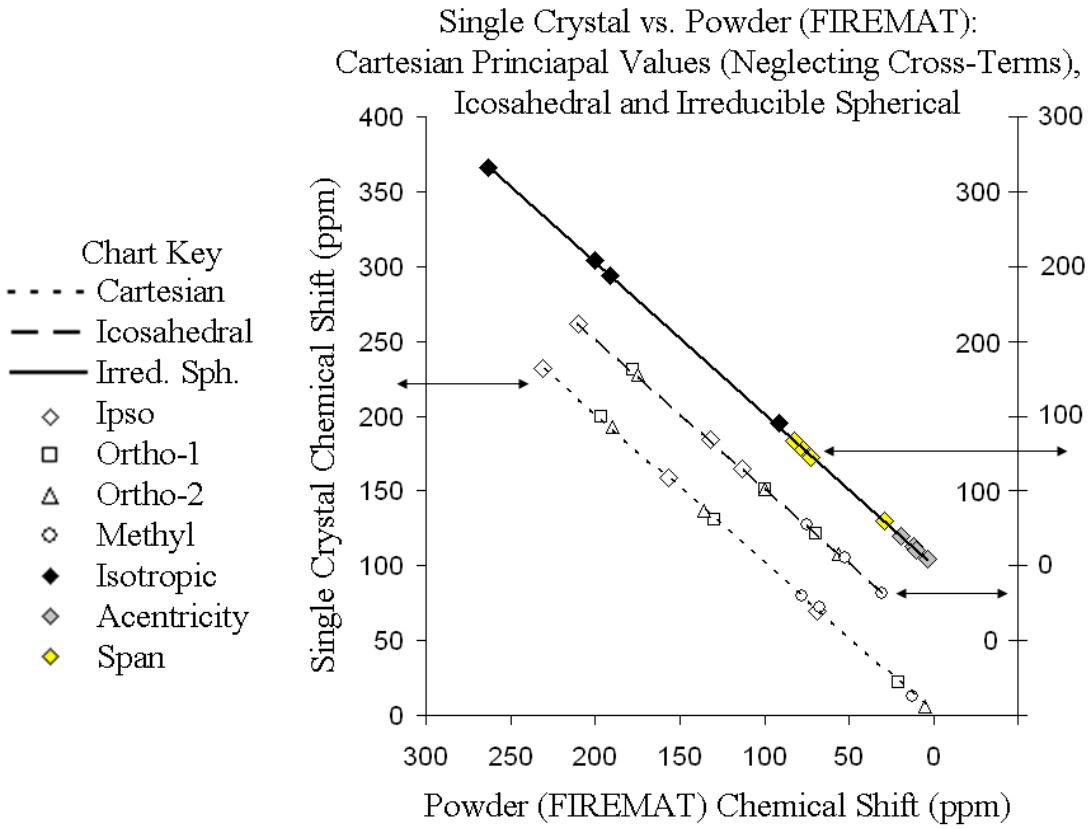

Figure 9. Comparison of single crystal and FIREMAT powder data. The three correlation lines actually overlap one another completely but have been offset by 0 ppm for the Cartesian plot, 50 ppm for the icosahedral line, and 100 ppm for the irreducible spherical data. This was done to make it easy to see clearly the corresponding plots by type. The latter two shielding scales appear on the RHS of the plot. The $d^2(k)$, averaged over k uses no degrees of freedom in the normalization. This machinery makes the variance deviation more comparable with d^2. Note, the statistics for the icosahedral and irreducible spherical tensors are identical within rounding errors. The FIREMAT data likely account for the largest portion of the ~2 ppm Std. Dev. as signal spinning sideband intensities play a greater role in measurement errors than do the single crystal measured shifts, which are frequently derived.

atomic terms also is presented along with an overall molecular rms value:

$$\text{rms-}d = \sqrt{\sum_k d^2(k)/n(k)}\,, \tag{38}$$

where $n(k)$ is the number of atomic tensors in the molecule. The individual $d^2(k)$ values vary among themselves with the rms d values ranging from 1.7 ppm to 2.5 ppm (obtained from $d^2(k) = 3.0$ ppm^2 to 6.1 ppm^2, respectively). Intrinsic line widths (note that the quaternary ipso carbon is the sharpest resonance and also has the lowest $d^2(ipso)$ value) carry errors accordingly. The span of the sidebands would affect the measurement of both frequencies and intensities if the spectral response is not the same across the spectrum. Stochastic methyl jumping could also lead to differences in the single and powder crystals. Thus, there are a varity of effects that could introduce differences in $d^2(k)$ for the various nuclei. All least-square plots, except for the non-orthogonal Cartesian case, yields parameters (variance and standard deviations) that correspond very well with the d^2 and rms-d, respectively, except for the Cartesian case. See Figure 9 and Table 3. Thus, these representations yield rms-d values that match the standard deviations of the fits.

Note in Table 3, the d^2 and rms d values are the same for all three representations. The slope and intercepts are consistent with one another even though the Cartesian scatter is slightly larger. The Cartesian variance is 5.1 ppm^2 (Std. Dev. = 2.3 ppm); multiple $R^2 = 0.9998$. Only minor differences exist between the Irreducible Spherical and Icosahedral representations. We now consider differences between theory and experimental tensors.

Table 3. Single crystal vs. FIREMAT data.[a]

Cartesian Principal Values (Neglecting Cross-Terms)		Irreducible Spherical	Icosahedral
Least Squares			
Equation	y = 1.01x + 1.2	y = 1.01x - 0.2	y = 1.01x + 1.6
R^2	0.9998	0.9999	0.9998
Variance (ppm^2)	5.1	4.3	4.3
Std. Dev. (ppm)	2.3	2.1	2.1
Mean Distance Squared			
d^2 (ppm^2)	4.3	4.3	4.3
d (ppm)	2.1	2.1	2.1

[a]12 Degrees of Freedom

Comparing Theoretical with Experimental Tensors

In the comparison of Theoretical/Experimental tensors, see Figure 10, the impact of using a proper Cartesian metric is more dramatic. See the considerable reduction of scatter in the two orthogonal and normalized representations (i.e., the Icosahedral and the Irreducible Spherical) when compared with the Cartesian data in Figure 10. All representation allow d^2 to be calculated with a proper metric matrix, but the Cartesian representation in a simple least-squares plot exhibits considerably more scatter with a much higher variance that would reduce the accuracy of determining molecular structure correlations.

A convenient way to relate shieldings to shifts is by plotting the theoretical vs. experimental results and determining a corresponding slope and reference intercept (e.g., $\sigma_\mu = m \cdot \delta_\mu + \sigma_{TMS}$). When comparing shielding to shifts the value of m = −1. These data define the linear transformation that places both sets of data on the same basis (typically the shift scale is calibrated to the TMS reference for ^1H and ^{13}C). The reference point for shielding tensors is usually zero where the diamagnetic and paramagnetic terms exactly cancel, but σ_{TMS} differs by about ≈185 ppm from σ_{REF}. Limitations in quantum mechanical computations and neglect of long distance intermolecular lattice shielding interactions show up as mean squared differences and/or errors between experimental and theoretical tensors. The success on the structural modeling is then approximated by the value of d^2 and the best of two or more structural models is taken to be the theoretical model that comes closest to the experimental tensor. Once the most promising tensor model is selected, the corresponding molecular structure ensues from the CQM computational results.

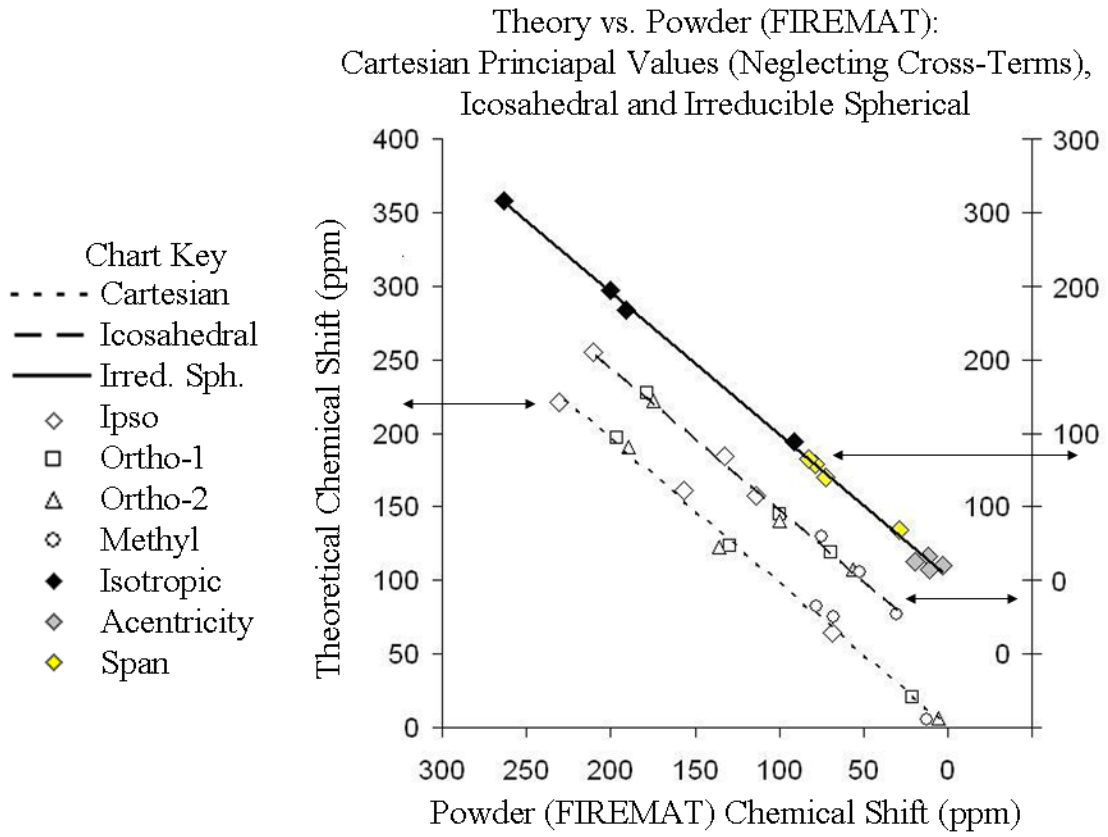

Figure 10. A principal value plot of theory vs. experiment uses only the δ_{11}, δ_{22}, and δ_{33} terms. The metric dilemma in the Cartesian plot increases the least-squares scatter of the line due to omission of the cross terms. The theoretical dispersion in the other plots is visibly less but none the less greater than found in the experimental tensors. Most likely, this ensues from theoretically ignoring differences in the intermolecular terms and in the limitation of the CQM modeling of structure.

The Cartesian and Icosahedral lines are relatively easy to construct from the respective shift and shielding values primarily because of their monotonic relations to one another. The compacted Icosahedral line (range 179 ppm) removes some of the worst scatter in the highly scattered mid-field points found in the Cartesian line (range ~215 ppm). Conversely, the Spherical plot (range ~250 ppm) is expanded, due primarily to the greater sensitivity of zero rank terms. While recognition of the scatter in Figure 10 is clouded slightly by psychological visual factors, when the ranges differ, the data of Table 4 clearly indicate the statistical improvement of the two orthogonal representations over that of the basic Cartesian formulation. Nonetheless, the best appreciation of the physical foundation of tensors and the basis of the experimental measurements lies in the Cartesian representation. Normalizing irreducible spherical terms could carry with it a great deal of theoretical complexity not familiar to many NMR application scientists.

While all three formulations yield a d^2 and rms-d of 16.5 ppm^2 and 4.1 ppm, respectively, the 43.1 ppm^2 variance of the Cartesian correlation plot is more than twice that of 18.0 and 18.9 ppm^2 variances of the remaining two formulations. The difference between variances in the 18-19 ppm^2 range is primarily due to the 10 vs. 12 degrees of freedom used, respectively, in a least-square plot vs. a mean square distance calculation.

Summary

The *Cartesian formalism* provides the basic definitions and the measureable quantities. This is usually the simplest representation for those that understand the rudiments of tensors and their three-dimensional properties. The analysis of errors and discrepancies of theoretical methods in comparing tensors is seriously handicapped by the nonorthogonal character of the Cartesian representation. However, one may use the

Table 4. Theory vs. FIREMAT data.[a]

	Cartesian Principal Values (Neglecting Cross-Terms)	Irreducible Spherical	Icosahedral
Least Squares			
Equation	y = 0.99x - 0.2	y = 0.97x + 1.8	y = 0.98x + 0.7
R^2	0.993	0.998	0.994
Variance (ppm^2)	43.1	18	18.9
Std. Dev. (ppm)	6.6	4.2	4.4
Mean Distance Squared			
d^2 (ppm^2)	16.5	16.5	16.5
d (ppm)	4.1	4.1	4.1

[a]10 Degrees of Freedom

Cartesian components and a slightly more complicated computation for the average distance square, d^2, to obtain an approximation of the variance of quantum mechanical structural correlation of experimental tensor shifts.

The *icosahedral representation* is easily constructed from the Cartesian components, is orthogonal and normalized, and readily applied to shift and theoretical components alike. Monotonic relationships make the exercise simple to use and one does not have to use a complicated analysis. Warping of the spin space to obtain the orthogonal quantities may be somewhat perplexing to the new spectroscopist, but is easily understood in terms of symmetry arguments not unlike those employed in group theory.

The *irreducible spherical representation* is the most complex construct of the three formalisms. Complexity ensues from referencing the theoretical shielding values to an experimental shift reference and the mixture of zero-rank and second rank-shift terms and the use of two scales that increase in opposite directions. This representation, however, possesses all of the benefits of the rotation matrix transformations of the molecular frame. There never will be totally serious NMR crystallography until single crystal work can be done with the ability to manipulate molecular frames using angular momentum theories. Single crystal data depend on frequency data which are more accurate than intensity data employed in sideband results. In the mean time, the FIREMAT spinning side band technique does yield isotropic zero-rank terms that also may be measured with highly accurate isotropic frequencies; the remaining anisotropic spherical components, which come from the less accurate side-band intensities. This spherical approach with a proper metric improves the experimental precision of

extracting structural data from chemical shift tensors. Spherical representations, unfortunately, suffer from an embarrassing plethora of similar shift scales and definitions.[69,72] Aside from the Cartesian metric complication, the field may be better served, even so, by always reporting the measured Cartesian shift components. This representation greatly reduces the ambiguity in the literature and provides everyone with rudimentary shift information with precise definitions.

In a recent set of molecular structure correlations obtained in the author's laboratory, Heider et al.[32] did an analysis of two Taxol® polymorphs per asymmetric unit cell using the Icosahedral representation. She sorted through 600 plus computations in a grid search analysis of the shifts that were compared with their computer generated structures. Using the most sensitive nuclear positions and a F-test of the average d^2 or variances for a least-squares fit, literally millions of conformational permutations are reduced to only 2-3 dozen structures (10 model structures for the A polymorph and 13 for the B polymorph). This *tour de force* indicated the feasibility of NMR crystallography; the power of its synergy with diffraction results, and the unequaled superiority of SSNMR to suggest positions for lattice H-atoms,[73] especially in powder samples. The full scope of the work is given by Heider et al.[32] These results are discussed briefly in Figure 11, which contains a comparison of computational energies using CQM vs. the shielding/shift d^2 or variance using the icosahedral formalism. As the ability to compare and to distinguish the various conformational structures depend in a large measure on working with reduced variances, use at least of the icosahedral representation is definitely beneficial. This work on a unit cell approaching 2,000 Daltons, has taken the technique into a molecular size where the data will be useful in many fields of endeavor.

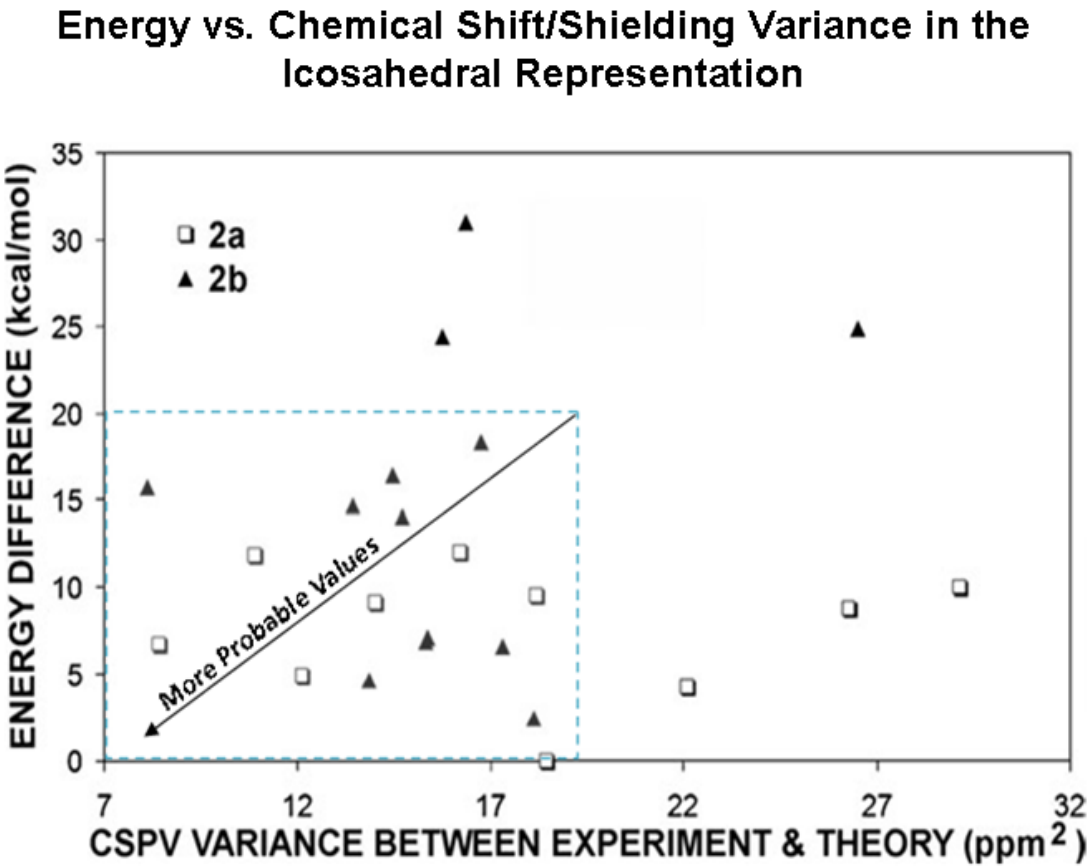

Figure 11. Energy difference (in kcal/mol) versus the variance (ppm^2) between experimental chemical shifts and theoretical shielding principal values. The two molecules of Taxol® (2a and 2b) that appear in the asymmetric unit are compared for a variety of conformers and effects of different types of H-bonds. The variances were determined for the highly sensitive nuclear positions C13, C18, C10, C20 and C30 using the Icosahedral representation and its metric. It was found in a grid search, involving more than 600 trial molecular models, but high statistical probability is found for only 23 of the test structures. Literally millions of test structures exist, which make computer methods intractable without the assistance of reasonable structural moieties obtained from experimental chemical shift results. The Icosahedral metric and method reduce the variance by a factor of two. These data are now ready for a renewed diffraction analysis to exploit the solid-state NMR data.[32] (Reprinted with permission from Heider, E. M.; Harper, J. K.; Grant, D. M. *Phys. Chem. Chem. Phys*. **2007**, *9*, 6083.)

CHAPTER 3

SOLID-STATE ^{13}C NMR INVESTIGATIONS OF 4,7-DIHYDRO-1H-TRICYCLO-PENTA[*def,jkl,pqr*]TRIPHENYLENE (SUMANENE) AND INDENO[1,2,3-*cd*]FLUORANTHENE: BUCKMINSTERFULLERENE MOIETIES*

Introduction

The existence of buckminsterfullerene (C_{60}) was predicted in 1970 by Eiji Osawa of Toyohashi University of Technology.[74] Prior to 1984, carbon was known to exist in only two allotropic forms, diamond and graphite. Kroto's interest in microwave spectroscopy in the study of chains of carbon atoms observed in outer-space near carbon-rich red stars lead to the chance discovery of C_{60}.[75] In that same year, spectroscopic evidence[76] of C_{60} was confirmed. A major advance in the study of C_{60} came in 1990 when Krätschmer et al.[77] developed a method to make macroscopic quantities of C_{60} and were able to obtain infrared and X-ray powder diffraction data that supported the previous structure predictions.[77] Further studies lead to the discovery of a wide range of fullerenes. Although fullerenes have been produced in laboratories, greater amounts than expected are found occurring in nature. The naturally produced C_{60} is found in soot and

---

* Reprinted with permission from Halling, M. D.; Orendt, A. M.; Strohmeier, M.; Solum, M. S.; Tsefrikas, V. M.; Hirao, T.; Scott, L. T.; Pugmire, R. J.; Grant, D. M. *Phys. Chem. Chem. Phys.* **2010**, *12*, 7934-7941.

formed by lightning discharges in the atmosphere.[78] Fullerenes have also been found naturally occurring in a family of minerals known as shungites.[79] Since its discovery, C_{60} has provided a basis for scientific advancement in engineering, medicine, and fuels/energy.[80,81,82,83,84,85,86] As such, an understanding of its structure and impact on science is important to future technologies and discoveries.

In C_{60}

> the carbon nuclei reside in a sphere of about 7 Å diameter, with the electronic wave functions extending inside and outside by about 1.5 Å. The diameter of the molecule is approximately 10 Å and there is a 4 Å cavity inside. The atoms are actually positioned at the 60 vertices of a truncated icosahedron (or soccer ball) structure, with 90 edges, 12 pentagons and 20 hexagons. The two different bond lengths in C_{60} (1.40 and 1.46 Å) indicate that the π-electrons are not delocalized evenly over all bonds.[87] The 30 short bonds are on the edges that are shared by two hexagons; the bond length at the 60 edges shared by a hexagon and a pentagon are longer.[88]

The formation of C_{60} can be simplistically described as assembling two bowl shaped structures, e.g., 4,7-dihydro-1H-tricyclopenta[def,jkl,pqr]triphenylene (sumanene) as the top and bottom *end-caps*, respectively, with two indeno[1,2,3-cd]fluoranthene structures (indenofluoranthene) providing the equatorial *belt* around the center of C_{60} (*vide infra*). Sumanene exists as a natural bowl structure due to the presence of three five-member rings around the periphery. On the other hand, indenofluoranthene has a planar structure that must be dimerized and distorted in order to provide the required equatorial *belt* that anchors the sumanene *end-caps*. The energetics involved in the dimerization of indenofluoranthene, and assembling the sumanene *end-caps* into the C_{60} structure with the associated displacement of all protons on the parent structural components is quite amazing. A careful study of the spectroscopic and theoretical basis of details for the

formation of C_{60} provides further insight into the electronic structures of highly curvature deformed aromatic compounds.

Solid-state NMR (SSNMR) has the capability of providing full structural information with atom level resolution[89] and this technique was used to identify the various fullerene structures. Chemical shift tensors have been used to determine many polycyclic aromatic hydrocarbon structures[90,91,92] and provide useful information about three-dimensional structure.[18,32,34,37] ^{13}C SSNMR chemical shift tensors, therefore, provide a means for analyzing the structure of C_{60}.[89] The experimental SSNMR work for C_{60} was performed by Tycko et al.[93] who reported the chemical shift tensor principal values to be 220, 186, and 40 ppm while Yannoni et al.[94] reported the chemical shift tensor principal values to be 213, 182, and 33 ppm. These principal tensor values are typical aromatic chemical shift tensor values. The δ_{33} component shows a substantial downfield shift caused by the adjacent five-member ring.

Since 1986, researchers have been using π-orbital axis vector (POAV) pyramidalization angles (θ_p) to define the three-dimensional curvature of bowl shaped polycyclic aromatic hydrocarbons.[95,96] The POAV is defined as the vector which creates three equivalent angles ($\theta_{\sigma\pi}$) from bisecting the pyramid formed at the apex of a sp^2 carbon atom and its three protruding σ-bonds, as shown in Figure 12. θ_p is defined as:

$$\theta_p = \theta_{\sigma\pi} - 90° \tag{39}$$

Since 1986, θ_p data have been reported for many such molecules, including C_{60}, corannulene, and sumanene.[97,98,99]

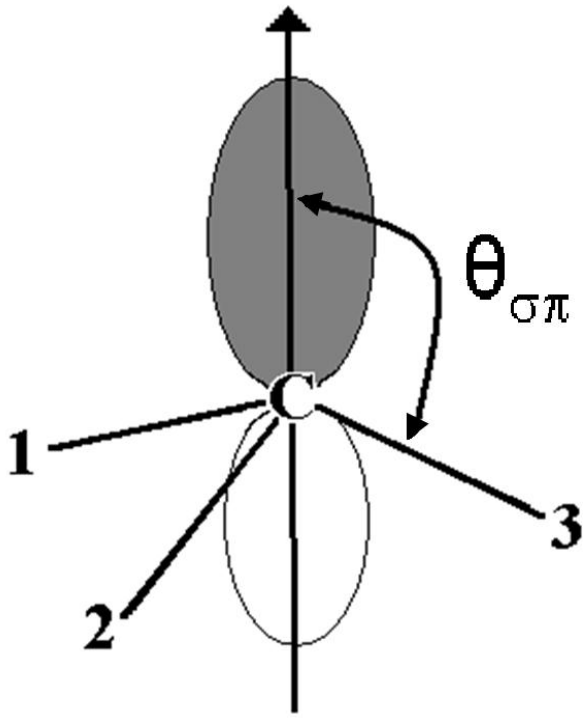

Figure 12. Depiction of POAV pyramidalization angle, θ_p, where $\theta_p = \theta_{\sigma\pi} - 90°$ and 1, 2, and 3 represent the adjacent atoms bonded to the sp^2 hybridized carbon atom at the vertex of the pyramid.

C_{60} has I_h symmetry. Hence, it contains multiple centers of rotation and very high symmetry. For this reason, in this paper, the curvature in each molecular system will be compared using θ_p in degrees as its basis. The θ_p for C_{60} is determined by symmetry to be exactly 11.64°.[97] The present study examines in detail sumanene and indenofluoranthene (shown in Figure 13), which are the two PAHs that are structural moieties found in C_{60}, using SSNMR techniques, X-ray diffraction, and theoretical methods. In order to understand the dynamics in indenofluoranthene the curvature and minimized energies of each molecular conformation needed to be investigated.

Corannulene has been studied for a number of years, because it is a known structural moiety of C_{60}. Corannulene has a θ_p of 8.2° for its inner carbon atoms,[98] based on the crystal structure of corannulene which was collected using single crystal X-ray crystallography.[100] Corannulene is of interest due to its curved three-dimensional shape and its involvement in the synthesis of buckybowl and fullerene structures. The SSNMR data for corannulene has been reported by Orendt et al.[91] The θ_p of corannulene is less than that of C_{60}, indicating that it is more planar than C_{60}.

Sumanene is a polycyclic aromatic hydrocarbon that forms the polar *end-caps* of C_{60} as shown in Figure 14a. It has a natural three-dimensional bowl shaped curvature similar to that found in corannulene. The θ_p of sumanene is 8.7°,[99] which is slightly greater than that found in corannulene but less than that of C_{60}, indicating a geometry that is more planar in conformation than C_{60}. The modest difference in θ_p between C_{60} and

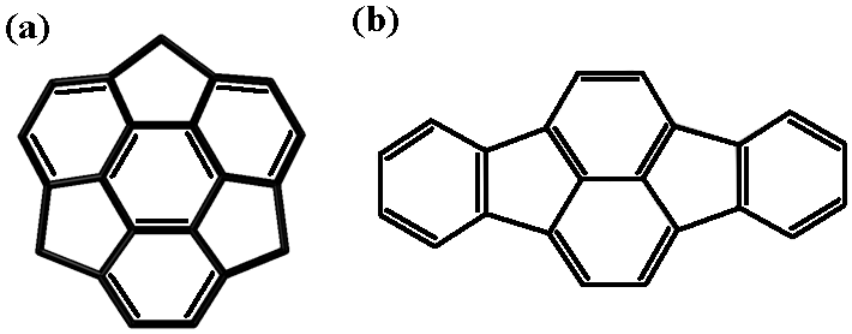

Figure 13. The structures of (a) sumanene and (b) indenofluoranthene.

sumanene is mostly due to relaxation of the rim away from the steep curvature in sumanene. As reported in the literature, sumanene has an inversion energy barrier of 82.1 kJ/mol at 140 °C, which indicates that inversion does not occur at room temperature on the NMR time scale.[101] Sumanene has a known X-ray structure[102] and reported ^{13}C isotropic spectrum containing four chemical shift values at 148.8, 148.6, 123.2, and 41.8 ppm.[101]

Indenofluoranthene, on the other hand, is a polycyclic aromatic hydrocarbon moiety that forms the *belt* circumscribing C_{60} as shown in Figure 14b. Indenofluoranthene is a planar molecule in its lowest energy conformational state. As such the θ_p for this conformation is 0°. Since indenofluoranthene is found as a moiety in C_{60}, its conformation and energy relationships between the planar and semi-hemispherical conformations with θ_p equivalent to that of C_{60} (11.64°) needs to be understood. Also of interest is the relationship between the chemical shift tensors of indenofluoranthene and how they change as a function of θ_p. A detailed discussion of these calculations and results follows in subsequent sections of this paper.

Experimental

Synthesis

Indenofluoranthene was prepared using the synthesis reported by H. A. Wegner, L. T. Scott and A. de Meijere.[103,104] The synthesis of sumanene was carried out following the method proposed by H. Sakurai, T. Daiko and T. Hirao [101]

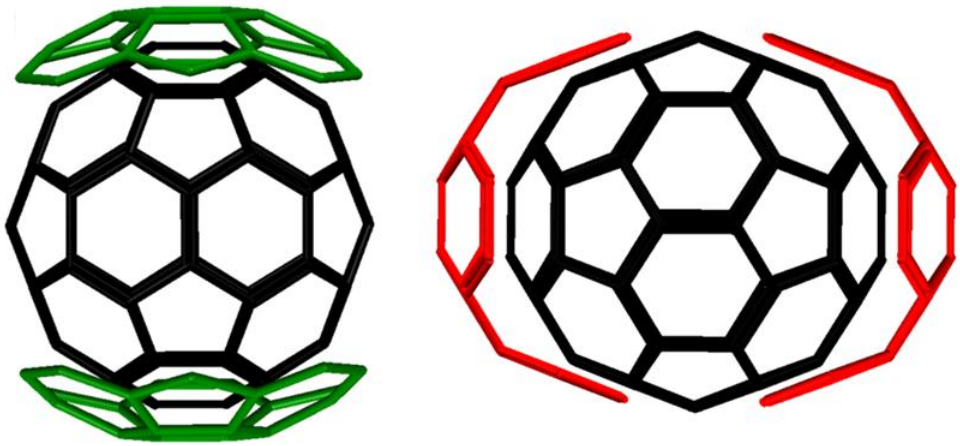

Figure 14. C_{60} with its structural moieties, (a) sumanene and (b) indenofluoranthene illustrating how they can be traced upon its surface.

Solid-State ^{13}C NMR

The ^{13}C FIREMAT data were collected on a CMX-400 NMR spectrometer operating at 400.119 MHz for ^{1}H and 100.622 MHz for ^{13}C using a 7.5 mm PENCIL rotor probe. The methyl peak of hexamethylbenzene (HMB) at 17.35 ppm was used for referencing and setting the Hartmann-Hahn match.[105] All data were collected at room temperature.

Sumanene

The FIREMAT data were collected utilizing a spinning speed of 1667 Hz and the FIREMAT pulse sequence.[13] Other parameters include a recycle time of 60.0 s, a 4.40 μs ^{1}H 90° pulse, a 8.70 μs ^{13}C 180° pulse, a contact time of 3.0 ms, and spectral widths of 16.6667 and 50.0000 kHz in the evolution and acquisition dimensions, respectively. The analysis utilized 512 transients collected during 10 evolution increments.

Indenofluoranthene

The FIREMAT data were collected utilizing a spinning speed of 2588 Hz and the FIREMAT pulse sequence.[13] Other parameters include a recycle time of 60.0 s, 4.30 μs ^{1}H 90° pulse, 8.50 μs ^{13}C 180° pulse, a contact time of 10.0 ms, and spectral widths of 10.3520 and 59.5238 kHz in the evolution and acquisition dimensions, respectively. The analysis employed 2048 transients collected during four evolution increments. FIREMAT data were also collected at -100 °C and they confirm the room temperature results.

Data Analysis

The 1D ^{13}C isotropic guide spectrum was derived in the typical way from the FIREMAT data via Fourier transformation of the evolution points corresponding to the first acquisition point according to Gan's P2DSS suppression method.[15] Sideband patterns for each of the isotropic values in the guide spectrum were calculated and fit using the TIGER processing method.[16]

Calculations

The calculations presented in this paper used the X-ray data of sumanene[102] and indenofluoranthene[104] as starting structural models. Following precedence from previous investigations,[106,107] the crystal structures were refined by optimizing the hydrogen atom positions using the Gaussian03 suite of programs[5] using Density Functional Theory (DFT) with the B3LYP exchange and correlation functionals[108,109] as described by Cheeseman and co-workers,[110,111] along with the 6-311G** basis set.[112,113] All of the chemical shielding calculations presented in this paper were performed using the Gaussian03 program utilizing the same experimental setup, DFT/B3LYP and respective basis sets, as was used in the refinement process with the calculation of chemical shielding tensor principal values performed using the Gauge-Independent Atomic Orbitals (GIAO) method.[114,115]

The energy calculations of the bending of sumanene and indenofluoranthene from a planar conformation to the $\theta_p = 11.64°$ were calculated with Gaussian03[5] using DFT/B3LYP[108,109] along with the 6-311G** basis set.[110,111] A grid analysis was

performed by increasing the curvature in small steps and measuring the energy for each intermediate conformation in order to develop an energy diagram for each molecule.

Results and Discussion

The numbering scheme for both sumanene and indenofluoranthene as used in this paper is given in Figure 15. The FIREMAT spectra for sumanene are given in Figure 16 and for indenofluoranthene are given in Figure 17. The FIREMAT experimental results and the theoretical results, calculated using Gaussian03, for the chemical shift tensors of sumanene and indenofluoranthene are reported in Tables 5 and 6, respectively. The experimental carbon tensor assignments were made, aided by the theoretical chemical shielding results. The correlation between experimental and theoretical data of sumanene and indenofluoranthene is shown in Figure 18. The error values reported in this paper are calculated using the RMS distance metric analysis approach introduced and discussed in detail by Alderman et al.[23] and Grant and Halling.[116] The error between experiment and theory for sumanene is 3.2 ppm.[23,116] The error between experiment and theory for indenofluoranthene is 3.1 ppm.[23,116] These results show that there is excellent agreement between the theoretical and experimental data, approximately 3.0 ppm difference. Furthermore, it also suggests that the crystallographic conformations of both sumanene and indenofluoranthene not only are the lowest energy conformations, but they also have the best agreement with NMR data.

The NMR results for sumanene not only correlate well between experiment and theory, but they also compare well with the isotropic chemical shift values reported in the literature[101] (1.5 ppm). The advantage of using SSNMR to analyze sumanene is that more information about three-dimensional structure can be acquired. With the

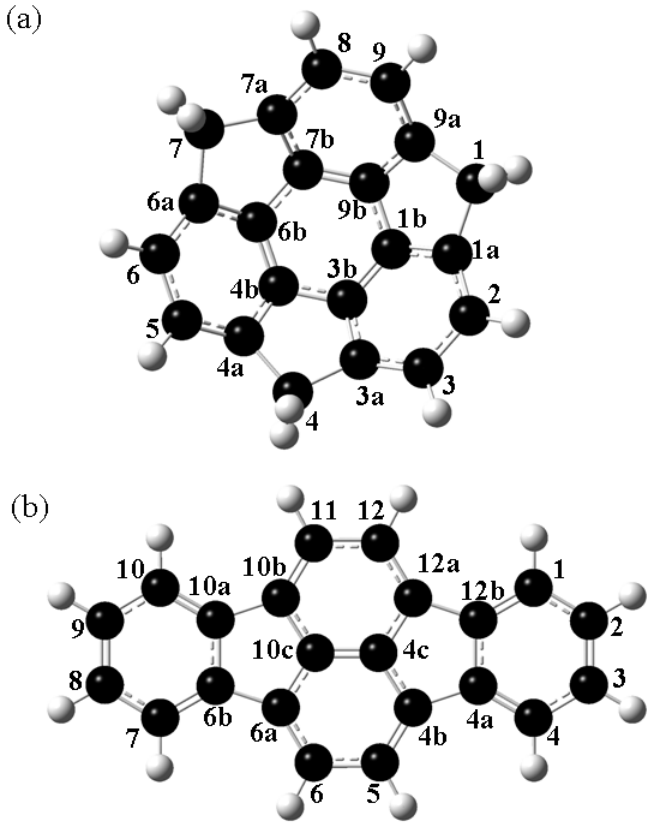

Figure 15. The numbering schemes used in this paper for (a) sumanene and (b) indenofluoranthene.

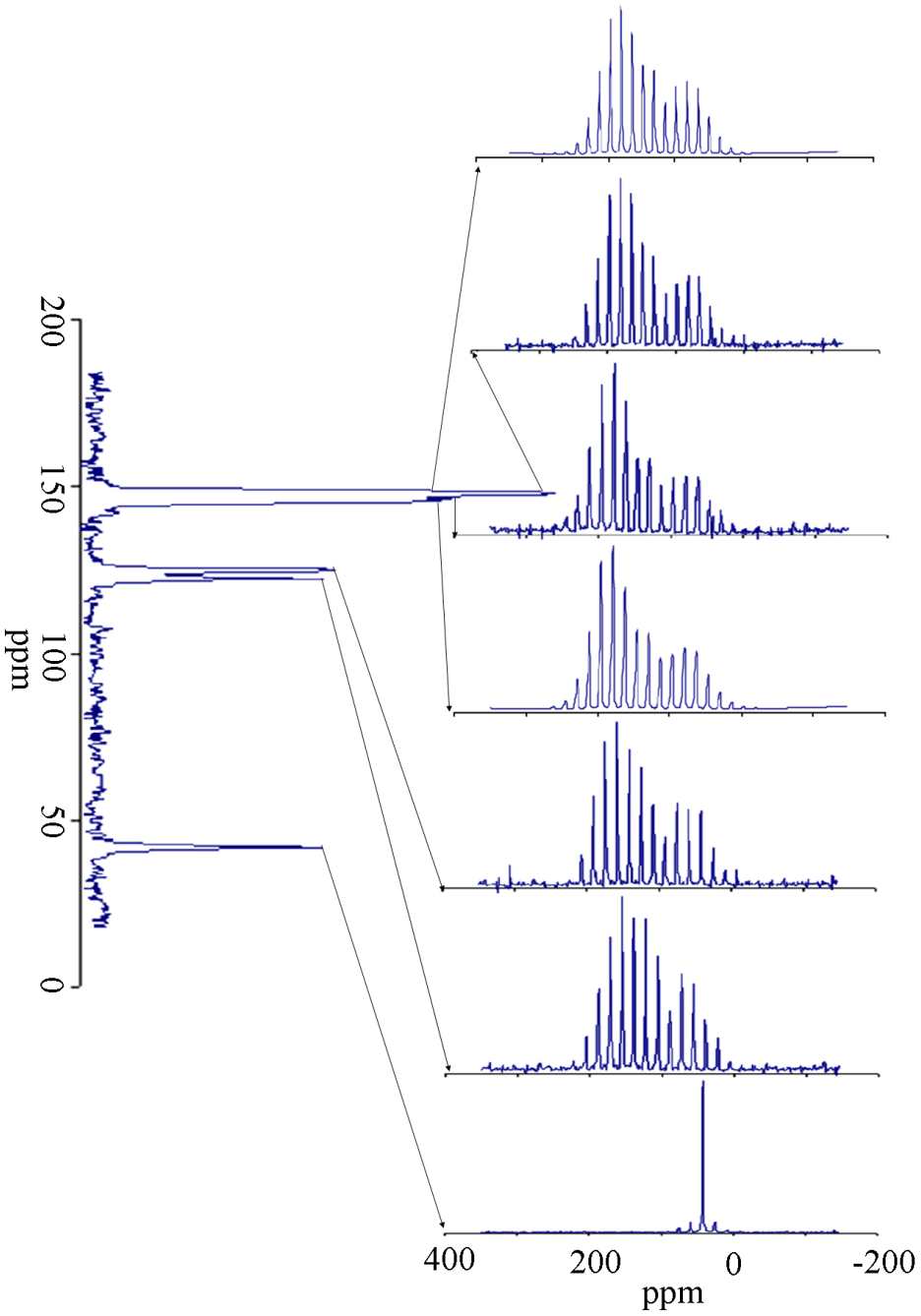

Figure 16. The FIREMAT spectrum of sumanene. The isotropic guide spectrum is along the y-axis and the anisotropic spinning-sideband patterns for each isotropic value are given along the x-axis.

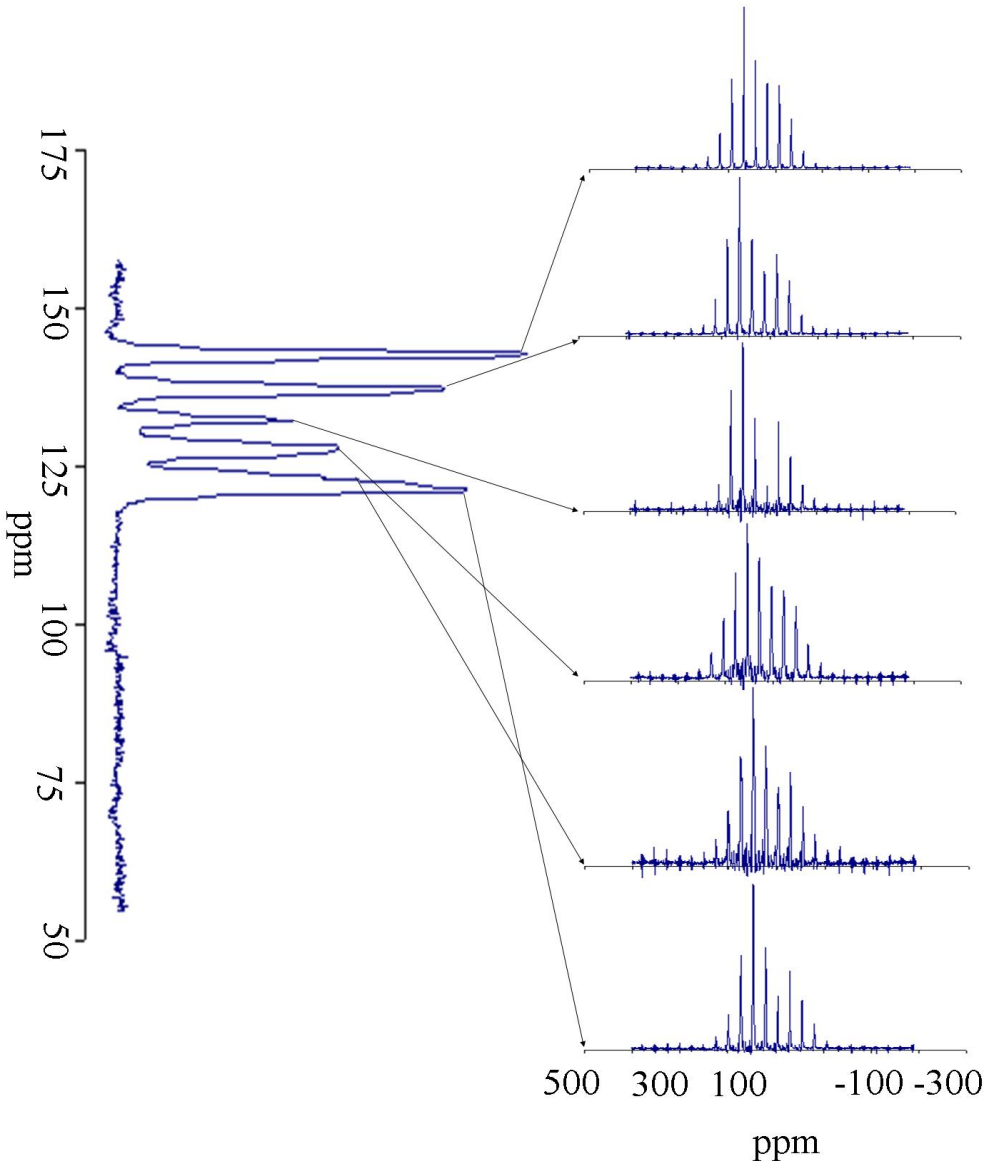

Figure 17. The FIREMAT spectrum of indenofluoranthene. The isotropic guide spectrum is along the y-axis and the anisotropic spinning-sideband patterns for each isotropic value are given along the x-axis.

Table 5. Experimental and theoretical CSA results for sumanene. Theoretical results reported are for the crystallographic conformation of sumanene and were calculated using Gaussian03. The experimental data were collected using the FIREMAT experiment. Sumanene has an error of 3.2 ppm in the correlation between experiment and theory.

Carbon		δ_{11}	δ_{22}	δ_{33}	δ_{iso}
1, 4, 7	Experiment	57.3	38.6	30.1	42.0
	Theory	67.2	32.9	21.5	40.5
2, 5, 8	Experiment	207.3	143.0	16.6	122.3
	Theory	211.7	136.3	16.9	121.6
3, 6, 9	Experiment	210.3	148.9	15.0	124.7
	Theory	212.1	137.8	17.0	122.3
1a, 4a, 7a	Experiment	231.6	178.0	32.8	147.5
	Theory	234.9	179.4	32.2	148.8
3a, 6a, 9a	Experiment	237.9	177.7	29.7	148.4
	Theory	235.7	179.0	32.1	149.0
1b, 4b, 7b	Experiment	227.2	178.9	29.2	145.1
	Theory	228.6	179.4	31.9	146.6
3b, 6b, 9b	Experiment	231.7	181.3	25.7	146.2
	Theory	229.1	180.3	32.3	147.2

Table 6. Experimental and theoretical CSA results for indenofluoranthene. Theoretical results reported are for the crystallographic conformation of indenofluoranthene and were calculated using Gaussian03. The experimental data were collected using the FIREMAT experiment. Indenofluoranthene has an error of 3.1 ppm in the correlation between experiment and theory.

Carbon		δ_{11}	δ_{22}	δ_{33}	δ_{iso}
1, 4, 7, 10	Experiment	213.1	143.5	12.6	123.0
	Theory	219.3	135.3	10.1	121.6
2, 3, 8, 9	Experiment	225.8	141.5	15.7	127.7
	Theory	233.1	136.4	11.0	126.8
5, 6, 11, 12	Experiment	201.7	148.4	13.4	121.2
	Theory	209.7	142.3	12.4	121.5
4a, 6b, 10a, 12b	Experiment	228.1	158.8	40.9	142.6
	Theory	227.6	156.4	44.8	142.9
4b, 6a, 10b, 12a	Experiment	221.1	161.4	28.8	137.1
	Theory	221.1	163.2	32.8	139.0
4c, 10c	Experiment	197.3	185.2	14.4	132.3
	Theory	193.8	181.9	19.8	131.8

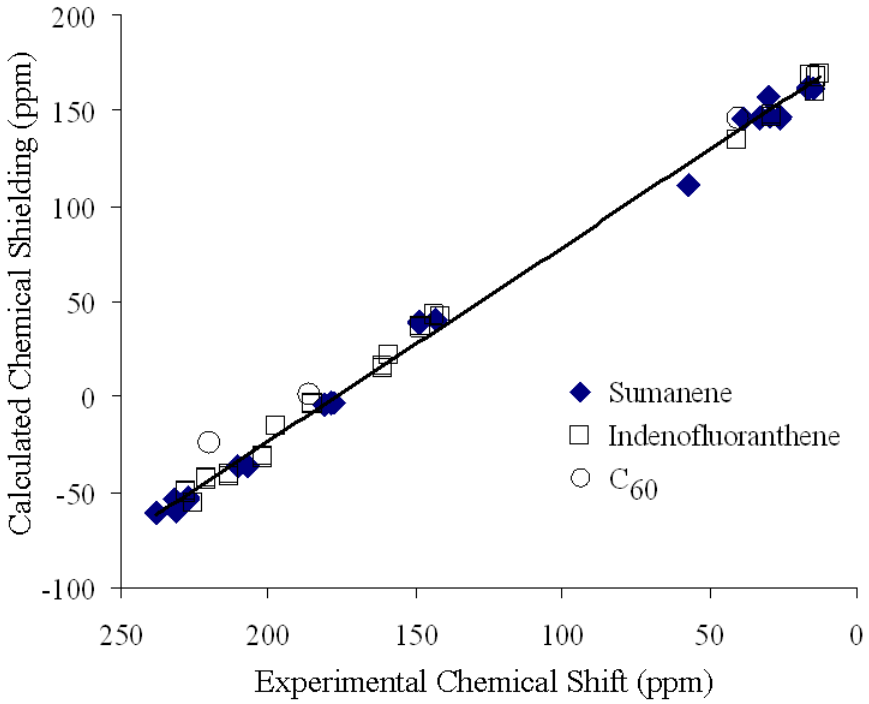

Figure 18. Correlation between theoretical chemical shielding and experimentally derived chemical shift for sumanene and indenofluoranthene. The equation of the linear least-squares fit is y = -1.02x + 180.1. The R^2 value for the data is 0.996, indicating an excellent correlation between experiment and theory. While the experimental chemical shift values of C_{60} were first reported in 1991, [93,94] modern theoretical values are added to this publication for the first time. The three theoretical principal values are: 209.3, 184.1, and 39.4 ppm.

FIREMAT experiment, the three chemical shift principal values were collected for each carbon position. In the case of sumanene, it is of interest to see how the principal values compare to those of corannulene and C_{60} to understand how curvature affects the bonding orbitals. A depiction of the changes in each of the chemical shift principal values of the nonprotonated carbon atoms for sumanene, corannulene, C_{60}, and indenofluoranthene is given in Figure 19.

The shift in the δ_{33} component of the chemical shift tensor has been observed to be related to effects due to ring deformation in PAHs,[64] with the downfield chemical shifts being related to greater curvature.[92] It is interesting to note that the δ_{33} components of sumanene are further downfield by approximately 30 ppm than the similar δ_{33} components of corannulene. The δ_{11} components of the *rim* and *hub* carbon positions in sumanene are further downfield than the similar δ_{11} components of corannulene by approximately 20 ppm.[91] The δ_{22} components of the nonprotonated carbon positions in sumanene and corannulene remain approximately unchanged, differing by ± 10 ppm.[91] These differences are due to the ring deformation on the nonprotonated carbon atoms with the largest difference being in the δ_{33} component of the *rim*, *r*, carbon. The *rim* carbon in sumanene has more ring curvature because of a higher population of peripheral five-member rings. These rings are the cause of the deformation in the three-dimensional structure in sumanene. Corannulene only has six-member rings in its periphery and its three-dimensional deformation is caused by a single internal five-member ring.

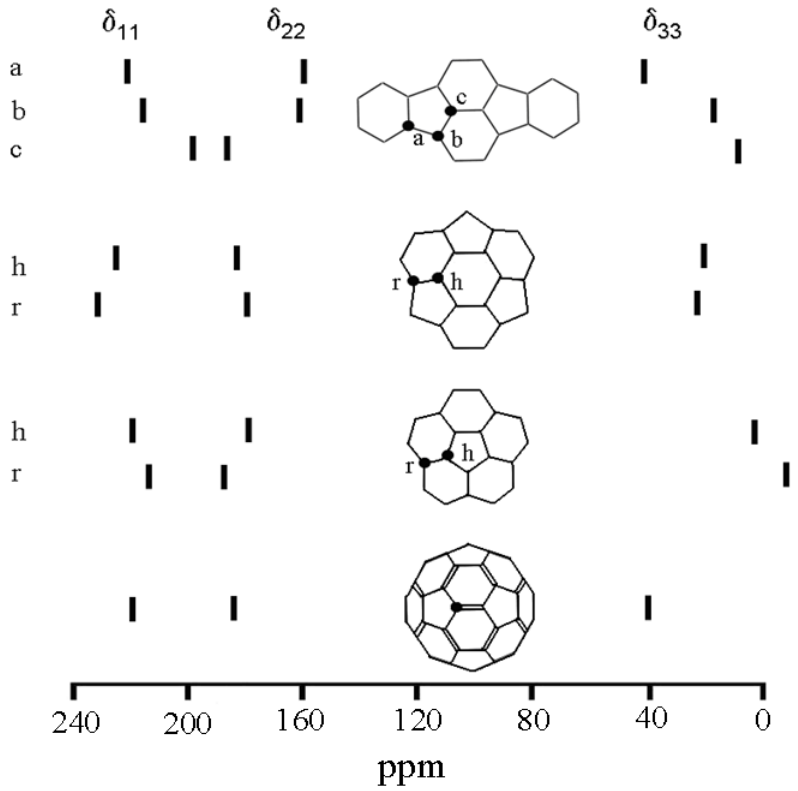

Figure 19. The experimental ^{13}C chemical shift principal values of the nonprotonated carbon atoms in indenofluoranthene, sumanene, corannulene, and C_{60} are plotted systematically. The labels, *a*, *b*, and *c* refer to the labels of the carbon atoms in indenofluoranthene. The labels *r* and *h* refer to *rim* and *hub* carbon atoms, respectively, in sumanene and corannulene.

The energy relationship with the conformation of sumanene is given in Figure 20. The NMR error vs. θ_p is also represented in Figure 20b. An interesting point in these diagrams is that both the minimum energy point and the lowest NMR error occur at the 7.3°, ranging from 3.1 ppm in its planar conformation to 4.0 ppm when $\theta_p = 7.3°$. This θ_p determined through X-ray crystallography, $\theta_p = 8.7°$. Table 7 lists the relationship between θ_p, the energy associated with sumanene curvature, and the NMR errors between theory and experiment. Another interesting feature of the energy diagram and the NMR error diagram in Figure 20 is that both diagrams show a modest local minimum when the molecule is flat, $\theta_p = 0.0°$.

An interesting attribute of indenofluoranthene is its minimized energy as it is related to the different structural conformations as well as the errors between experimental and theoretical NMR data.[23,116] These data are represented for indenofluoranthene in Figure 21. The lowest energy conformation of indenofluoranthene was found to be planar, $\theta_p = 0°$, unlike C_{60} and sumanene. Interestingly, the energetics involved with the structure yield a soft barrier to inversion which allows indenofluoranthene to distort to a curvature of $\theta_p = 4.73°$ at an energy of 57.4 kJ/mol. The relationship between θ_p, the energy associated with indenofluoranthene distortion, and the NMR errors is given in Table 8. The amount of energy required to distort planar indenofluoranthene to its curved configuration as found in the equatorial *belt* moiety in C_{60}, with $\theta_p = 11.64°$, is calculated to be 310.6 kJ/mol. This is a considerable amount of energy, but a large amount of which can be explained by the repulsion strain of the attached hydrogen atoms. At this conformation, the distance between hydrogen atoms is

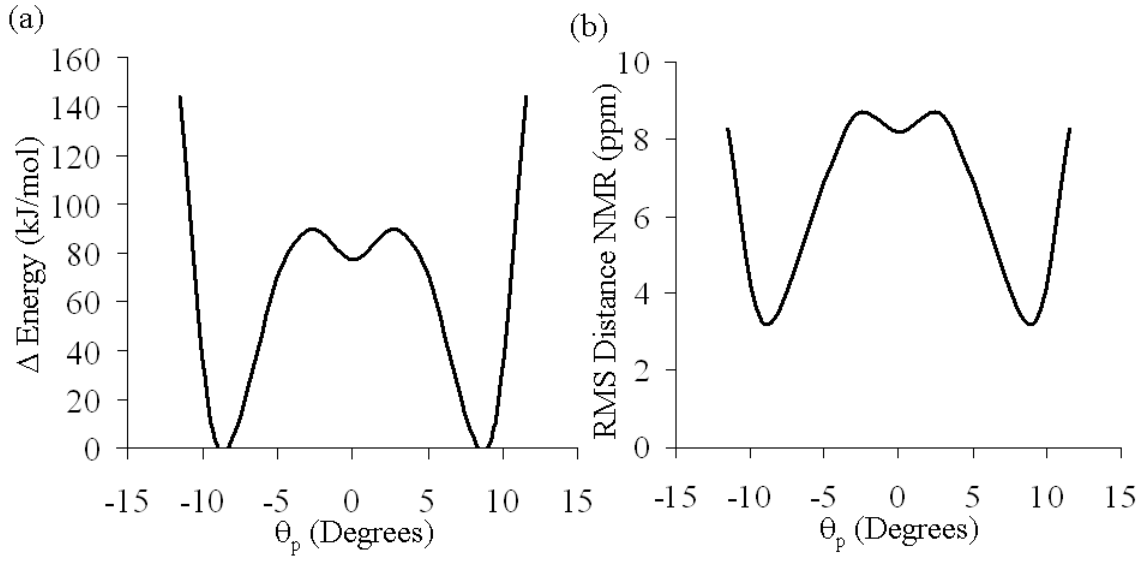

Figure 20. Curves consisting of various structural conformations of sumanene associated with inversion bending including (a) the change in energy (kJ/mol) vs. θ_p (Degrees) and (b) the NMR errors (ppm) vs. θ_p (Degrees).

Table 7. The relationship between θ_p, the change in energy associated with curved sumanene from a flat conformation to its curved conformations, and the NMR errors for each conformation.

θ_p (Degrees)	ΔE (kJ/mol)	NMR Error (ppm)
11.64	144.2	8.3
8.70	0.0	3.2
4.86	73.2	7.0
2.76	89.8	8.7
0.00	77.4	8.2

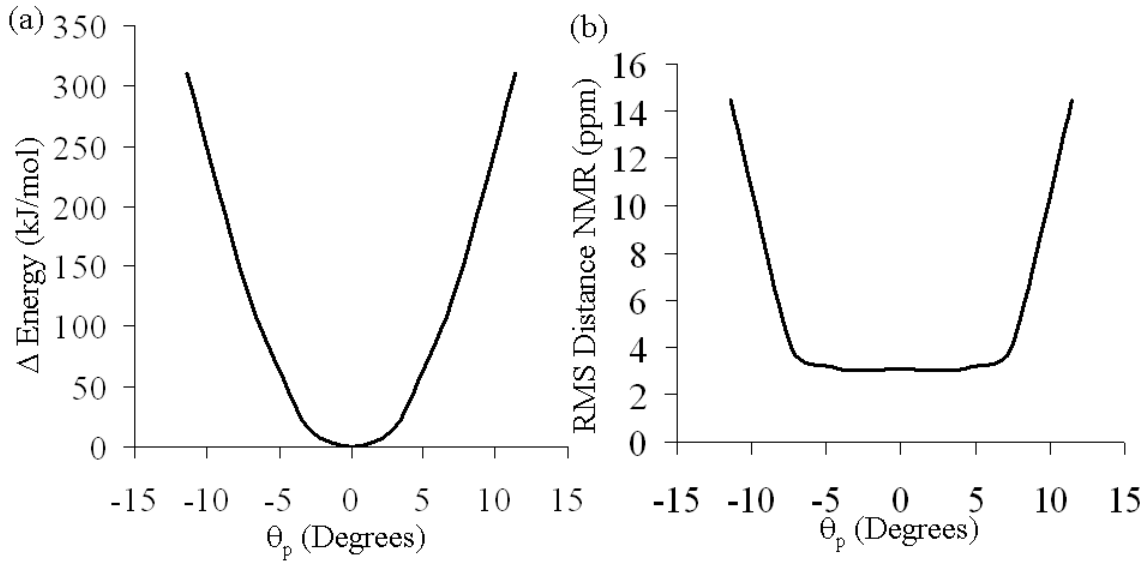

Figure 21. Curves consisting of various structural conformations of indenofluoranthene associated with inversion bending including (a) the change in energy (kJ/mol) vs. θ_p (Degrees) and (b) the NMR errors (ppm) vs. θ_p (Degrees).

Table 8. The relationship between θ_p, the change in energy associated with bending indenofluoranthene from a flat conformation to its curved conformations, and the NMR errors for each conformation.

θ_p (Degrees)	ΔE (kJ/mol)	NMR Error (ppm)
11.64	310.6	14.4
7.31	133.8	4.0
4.73	57.4	3.2
2.89	14.4	3.0
0.00	0.0	3.1

slightly less than the Van der Waals radius of hydrogen, producing large repulsion between hydrogen atoms.

The NMR results for indenofluoranthene show that the error between experiment and theory does not change significantly until the structure is distorted to a θ_p of at least suggests that indenofluoranthene is a highly flexible PAH in which bending out of plane can occur at room temperature. The ring distortion, evidenced by the large downfield δ_{33} principal component of 40.9 ppm at the carbon labeled *a* in Figure 19, is one of the furthest downfield δ_{33} shift components in a PAH that has been collected. It is nearly identical to the 40 ppm δ_{33} shift reported for C_{60}. The δ_{11} shift component is approximately equivalent to δ_{11} shift components of similar nonprotonated carbon atoms in sumanene. The δ_{22} component is approximately 20 ppm further upfield than similar δ_{22} components in sumanene. The substantially large value in the δ_{33} component suggests that there is a large amount of ring distortion within the five-member rings of indenofluoranthene. The majority of PAHs that include five-member conjugated rings are three-dimensional curvature-deformed molecules. In comparison, the planar conformation of indenofluoranthene contains a considerable amount of proton-proton repulsion trying to reduce the curvature of the molecular plane due to the presents of five-member rings.

The NMR error data comparing the experimental and theoretical chemical shift tensors for indenofluoranthene show that from the planar conformation up to a conformation of $\theta_p = 7.31°$ the theoretical chemical shift tensor data and the planar experimental data do not differ significantly. This suggests that the change in the

principal values as a change in conformation in indenofluoranthene are relatively small and that both theory and experiment predict the same dominant features contributing to the three-dimensional structure of indenofluoranthene. Just as in the energy vs. θ_p discussion, once indenofluoranthene bends close to its $\theta_p = 11.64°$ value as in C_{60}, the repulsion of the hydrogen atoms takes over and cause the NMR error values to increase dramatically. There is also high correlation between the experimental and theoretical isotropic chemical shifts with an error of 1.2 ppm.

Conclusion

The SSNMR data for sumanene and indenofluoranthene, important structural moieties of C_{60}, provide structural information regarding three-dimensional shape and structure. This information includes chemical shift tensors, which give information about the three-dimensional chemical shift anisotropy of each carbon atom. Comparisons with theoretical data also offer confirming information of the energetics involved with bending indenofluoranthene and these conformational relationships with fullerenes and its role in the formation of C_{60}. The theoretical results aided in making experimental assignments of tensors.

The substantially large downfield shift of the δ_{33} component of the chemical shift tensor for the *a* labeled carbon (shown in Figure 19) indicates high ring deformation at that position. The 40.9 ppm δ_{33} shift is nearly identical to the 40 ppm δ_{33} shift of C_{60}. Indenofluoranthene is a flexible molecule with the ability to flex with relatively little energy added to the system, making it an ideal candidate in fullerene and other related molecular synthesis. This is evidenced by the excellent correlation between experimental

^{13}C NMR results and theoretical results with curvature deformation, whereas sumanene and corannulene reflect properties similar to those found in C_{60}. While the experimental chemical shift values of C_{60} were first reported in 1991, [93,94] modern theoretical values are added to this publication for the first time. The three theoretical principal values are: 209.3, 184.1, and 39.4 ppm. The excellent correlation between experiment and theory for all three compounds is given in Figure 18. The SSNMR results for sumanene and indenofluoranthene reported in this paper are supported by excellent correlation with theoretical results.

CHAPTER 4

SOLID-STATE NMR SPECTRA AND LONG, INTRADIMER BONDING IN THE π-$[TTF]_2^{2+}$ (TTF = TETRATHIAFULVALENE) DICATION*

Introduction

Tetrathiafulvalene (2,2'-bi-1,3-dithiole), TTF, is an important electron donor that as the TCNQ (7,7,8,8-tetracyano-*p*-quinodimethane) electron transfer salt led to the study and development of organic-based electrical conductors.[117] In solution TTF can be reversibly oxidized to $[TTF]^{\bullet+}$ and $[TTF]^{2+}$;[118] however, their isolation in the solid state is rare. Frequently compounds with extended structures with TTF are isolated in a fractional oxidation state.[119] These oxidation states have evoked a paper entitled "Do π-dimers of tetrathiafulvalene cation radicals really exist at room temperature?"[120] Mono-oxidized TTF has frequently been isolated as its eclipsed cofacial ~D_{2h} dimer dication, $[TTF]_2^{2+}$ in the solid state,[121] and have also been reported in solution,[122] as typified by $[TTF]_2[ClO_4]_2$.[123] The molecular structures of TTF and $[TTF]_2^{2+}$ are given in Figure 22. These dimers have short, intradimer C-C and S-S separations (~3.4 Å) that is less than the sum of the van der Waals radii (3.6 Å) due to sulfur.[124] This suggests that the structure of the $[TTF]_2^{2+}$ dimer is similar to that for $[TCNE]_2^{2-}$ (TCNE = tetracyanoethylene).

---

* Reprinted with permission from Halling, M. D.; Bell, J. D.; Pugmire, R. J.; Grant, D. M.; Miller, J. S. *J. Phys. Chem. A.* **2010**, *114*, 6622-6629.

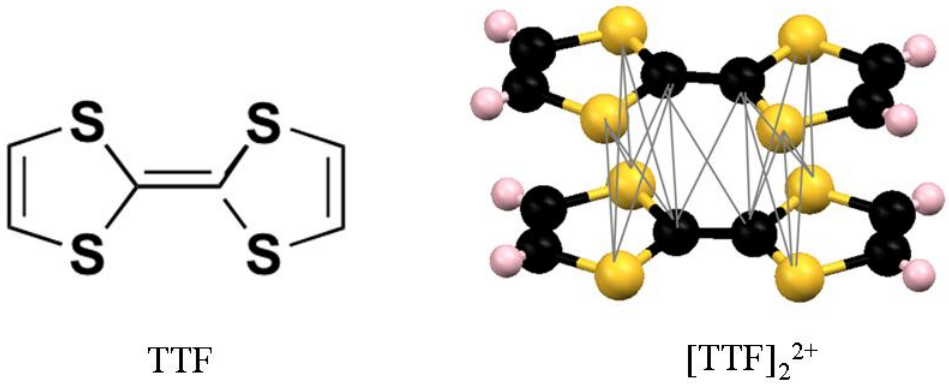

TTF $[TTF]_2^{2+}$

Figure 22. The molecular structures of TTF and $[TTF]_2^{2+}$.

$[TCNE]_2^{2-}$ has been studied by a variety of methods[125,126] including solid-state NMR (SSNMR),[127] and its electronic structure is best described by a $2e^-/4$ center ($2e^-/4c$) multicenter bond with an $^1A_{1g}$ ($b_{2u}^2 b_{1g}^0$) ground state. This analysis has been extended to $[TTF]_2^{2+}$ and it is best described by a $2e^-/6c$ multicenter bond with 2 C and 4 S bonding components and a singlet ground state, $^1A_{1g}$.

The theory of the NMR chemical-shielding is well understood and both *ab initio* and DFT methods are used to correlate the experimental chemical shift parameters with structure, conformation, bonding and other molecular properties for a variety of compounds.[128,129,130,131] To understand the nature and strength of the intradimer bonding in $[TTF]_2^{2+}$ quantum mechanical DFT NMR calculations were performed on TTF, $[TTF]^+$, and $[TTF]_2^{2+}$ to provide an understanding of the intradimer bonding in $[TTF]_2^{2+}$ through chemical shift tensors, and to provide a basis for comparison with experimentally achieved chemical shift tensors for TTF and $[TTF]_2^{2+}$. This study is unique to other investigations involving TTF, because only liquid NMR studies reporting isotropic chemical shifts have been reported in the literature[132] and we report and discuss the results of ^{13}C solid-state NMR studies of TTF and $[TTF]_2^{2+}$ herein. Many ^{13}C chemical shift tensors have been studied and a database containing many of their trends has been compiled.[133] Multiple ^{13}C NMR studies have been performed to investigate the chemical shift effects in π-bonds on olefinic and aromatic systems, resulting in general rules formulated for discussing these systems.[134,135,136] These findings show that the ^{13}C chemical-shift tensor components lying in the molecular plane for ethylene-like carbon atoms in aromatic or olefinic hydrocarbons exhibit a sensitivity to π-electrons and the paramagnetic shielding typically spans more than a hundred ppm. These large chemical

shift variations arise from the magnetic field mixing of π- and σ*-orbitals or σ- and π*-orbitals. These results are compared to that observed for TCNE, $[TCNE]_2^{2-}$, and $[TCNE]^{2-}$.

Ramsey proposed that the magnitude of the chemical shift tensor is inversely proportional to promotional energies, 1/ΔE's, between occupied bonding and unoccupied anti-bonding orbitals.[1] Ramsey discussed both orbital diamagnetic and orbital paramagnetic ring currents using perturbation theory. The differences in the promotion energies of the sigma and pi valence orbitals and the corresponding low-lying anti-bonding valence orbitals has a significant effect on the electron shielding currents especially those dominated by π-orbitals. The details of the interactions of the HOMO and LUMO have been discussed.[121] This notation for highest occupied and lowest unoccupied MO may be unfortunate as the HOMO/LUMO designations were established for optical spectroscopy where electrons may be transferred unequivocally between an occupied orbital and an unoccupied orbital. Ring currents arising from strong magnetic fields simultaneously promote angular momentum components for almost all valence orbitals, unlike optical methods. This issue, clearly understood by chemical shielding theoreticians, is treated briefly in the results and discussion section.

Wave function energies, chemical shift tensors, and single crystal X-ray diffraction (SCXRD) structures reflect a variety of physical properties. From each of these methods, lattice parameters can be extracted and better understood. Wave functions and chemical shielding depend on similar energy considerations. They both have similar average dependence on molecular motions. SCXRD determines crystalline structural parameters using linear lattice displacements. Further, molecular motion causes

averaging of values. Fortunately, the average structure of π-$[TTF]_2^{2+}$, involving very weak long bonds, is sensitive to the intradimer bond length of 3.4 Å obtained from SCXRD. Chemical-shift tensors have been shown to be sensitive to bond and torsion angles. Shielding parameters are also sensitive to intra- and inter-molecular effects including hydrogen bonding, non-bonding repulsions, intermolecular ring current effects, and electrostatic field interactions.[17,38,137,138,139,140]

The quantum mechanical embedded ion method (EIM) determines a crystal's atomic charges within a surrounding point charge array. The locations of the point charges in the lattice are determined by the diffraction data.[141] The atomic charges in the molecular system are then calculated using a natural population analysis (NPA).[142,143] The EIM optimizes the positions and charges of the hydrogen atoms while calculating the charges on the heavy hetero-atoms. Iterations between Ewald and NPA calculations are performed until the atomic charges do not change significantly. Through these calculations, the electrostatic potential Madelung constant is reproduced along with a three dimensional array of partial atomic charges of the nuclei at the crystallographic locations. This EIM self-consistent potential accounts for polarization and electrostatic lattice effects. This method has been shown to reliably improve the chemical shift tensors of several ionic and hydrogen bonded species, but lattice symmetry often minimizes the magnitude of these charge variations.

Methods

Sample Preparation

A commercial sample of TTF was purified by sublimation, and $[TTF]_2[ClO_4]_2$ was prepared by a literature method.[119] The magnetic susceptibility was measured above 250 K in a 1000 Oe applied field on a Quantum Design MPMS superconducting quantum interference device (SQUID) magnetometer as previously reported.[144]

^{13}C Solid-State NMR

Data were collected on a CMX-400 NMR spectrometer operating at 400.12 MHz for ^{1}H and at 100.62 MHz for ^{13}C. All spectra are referenced relative to TMS via a secondary external reference to the methyl peak of hexamethylbenzene at 17.35 ppm. Samples were packed into 7.5 mm o.d. rotors made from zirconia and were run in a 7.5 mm PENCIL rotor probe.

Cross polarization was used to enhance the ^{13}C nuclei signal in TTF, along with background suppression to eliminate a signal from the probe body.[105,145-146] A 90 s recycle delay was used on TTF and a 15 s recycle delay was used on $[TTF]_2^{2+}$ to maximize signal to noise. The $\pi/2$ pulse width for ^{1}H was 4.0 μs, the $\pi/2$ pulse width for ^{13}C was 4.0 μs and the ^{13}C π-pulses were 8.4 μs. The FIREMAT[13] spinning speed was 1221 Hz to collect a magic angle spinning (MAS) spectrum with a sufficient number of sidebands for accurate determination of the principal values of the chemical-shift tensors from the sideband patterns present in the spectrum. The spectral width was 85.470 kHz with 1056 transients and 2048 acquisition points for TTF and $[TTF]_2^{2+}$. The cross polarization and dipolar dephased spectra were collected at a spinning speed of 4 kHz. A

dephasing time of 42 μs was employed to eliminate CH_2 and CH peaks and to aid spectral assignment.

Data Analysis

Data were transferred to a Sun Enterprise 3500 and analyzed with software developed in-house. The 1D ^{13}C isotropic guide spectrum was derived directly from the FIREMAT data via Fourier transformation of the evolution points corresponding to the first acquisition point according to Gan's P2DSS suppression method.[15] Sideband patterns for each of the isotropic values in the guide spectrum were calculated and fit using the TIGER processing method.[16]

Calculations

Density functional theory (DFT) computations were performed using the Gaussian03 suite of programs.[5] Calculations where performed on TTF and $[TTF]_2[ClO_4]_2$ at the B3LYP[97,147] and B3PW91[148] levels of theory using the D95**,[98,149] 6-311+G**,[150,151] cc-pVDZ[129] basis sets. The DFT calculations on TTF and $[TTF]_2^{2+}$ were performed using default-spin and the DFT calculations on $[TTF]^+$ were done using UB3LYP and UB3PW91. The shielding tensor calculations used gauge invariant atomic orbitals[152,153] (GIAO) method. The theoretical shielding tensors were converted to the chemical-shift scale using a linear least-squares fit of theory and experiment. A natural bond orbital (NBO) analysis was performed using NBO as implemented in Gaussian03.[154] The NBO calculations utilized B3LYP and MP2 levels of theory and the 6-311+G** basis set. Chemical shift tensor computations were performed using the heavy-atom positions obtained[155] from diffraction data and proton positions were optimized through quantum chemical geometry optimization using Gaussian03,

following precedence from previous investigations.[113,114] The embedded ion method (EIM)[156] was used to investigate the electrostatic lattice potential in $[TTF]_2^{2+}$.

Results and Discussion

^{13}C Solid-State NMR Spectra

FIREMAT spectra were acquired for TTF and $[TTF]_2^{2+}$ to obtain chemical-shift tensor principal values. The FIREMAT spectra of TTF and $[TTF]_2^{2+}$ are shown in Figures 23 and 24, respectively. An isotropic guide spectrum was fit directly from the experimental data. The isotropic spectrum of TTF contains two peaks appearing at 110.9 ppm, which are assigned to the ethylenic carbon atoms, and 120.5 ppm, which are assigned to the CH carbon atoms. These values agree within ± 1.0 ppm of the isotropic chemical shift values reported by Miyajima et al.[132] The isotropic spectrum of $[TTF]_2^{2+}$ contains twelve carbon peaks in the isotropic spectrum with eight protonated carbon peaks appearing at 137.3, 136.6, 134.7, 134.4, 133.5, 132.4, 132.3, and 132.1 ppm and four ethylenic carbon peaks appearing at 145.3, 140.3, 140.2, and 139.6 ppm. The sideband patterns were extracted using TIGER processing and the experimental chemical shift tensor principal values for the ethylenic and protonated carbon atoms for TTF and $[TTF]_2^{2+}$ are reported in Tables 9 and 10. In spite of the significant overlap of the three ethylenic carbon atoms with isotropic shifts centered around 140 ppm, TIGER was able

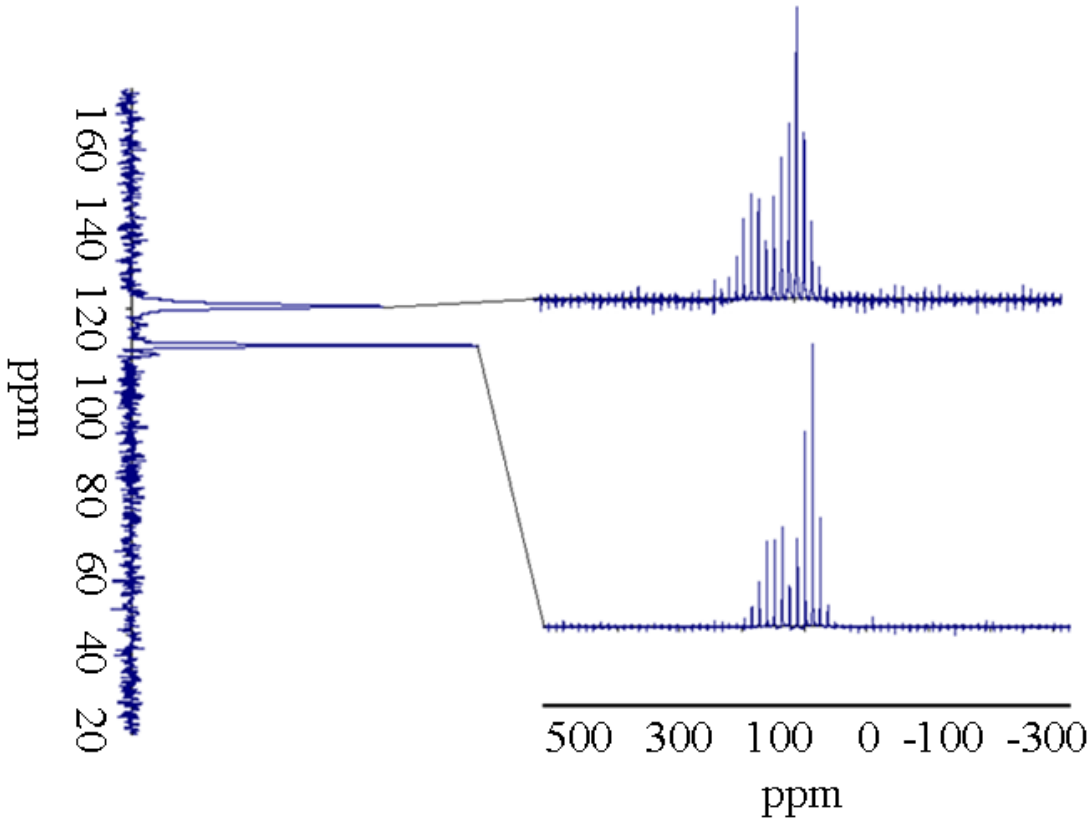

Figure 23. FIREMAT spectrum of TTF.

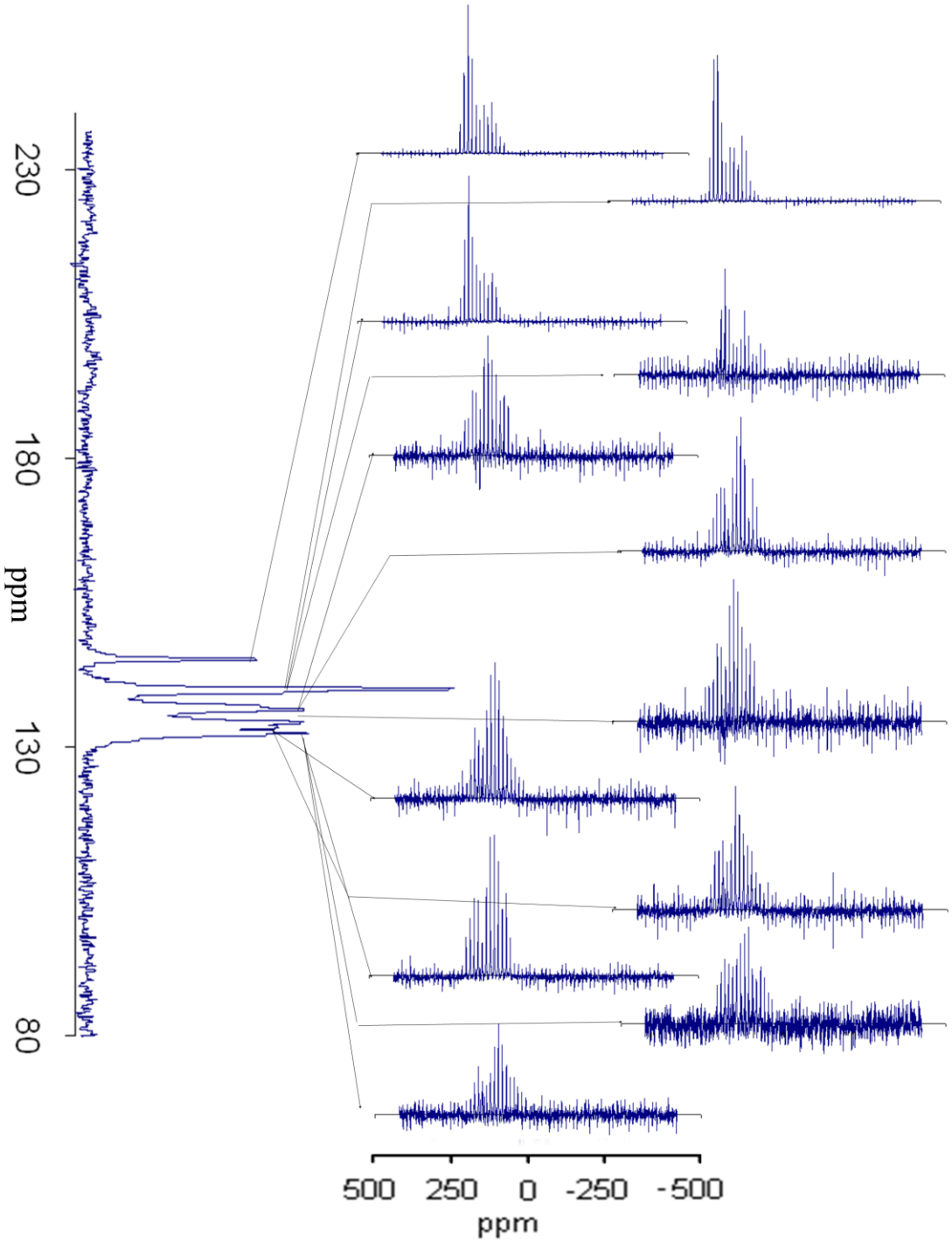

Figure 24. FIREMAT spectrum of $[TTF]_2^{2+}$.

Table 9. TTF chemical shift tensor data.[a]

TTF	Experimental Chemical Shift			Theoretical Chemical Shift (Using 6-311+G** Basis Set)		
Carbon	δ_{11}	δ_{22}	δ_{33}	δ_{11}	δ_{22}	δ_{33}
Ethylenic	180.4	76.2	76.2	179.2	85.1	69.4
CH	198.9	96.6	65.9	199.3	96.6	65.0

[a] The RMS distance error between the experimental chemical shift theoretical chemical shielding is ± 2.4 ppm.

Table 10. $[TTF]_2^{2+}$ chemical shift tensor data.[a]

$[TTF]_2^{2+}$	Experimental Chemical Shift			Theoretical Chemical Shift (Using 6-311+G** Basis Set)		
Carbon	δ_{11}	δ_{22}	δ_{33}	δ_{11}	δ_{22}	δ_{33}
Ethylenic						
C9	184.1	173.5	62.8	191.5	175.9	65.7
C10	191.6	183.3	60.9	190.3	180.5	70.3
C23	189.9	169.1	61.1	191.4	162.2	67.1
C24	185.9	167.9	64.9	184.1	151.3	69.9
CH						
C5	204.7	127.6	64.0	210.4	124.0	59.4
C6	210.2	126.6	66.3	214.7	130.6	64.2
C7	212.3	134.4	57.1	214.9	135.0	60.1
C8	216.4	133.0	62.6	217.5	133.1	63.9
C19	219.5	129.6	60.5	217.8	131.3	60.2
C20	210.7	121.1	65.5	215.2	126.7	61.0
C21	212.9	126.1	61.4	211.9	122.1	54.3
C22	212.6	120.0	64.4	210.4	120.1	55.7

[a] The RMS distance error between the experimental chemical shift theoretical chemical shielding is ± 3.8 ppm.

to resolve the principal components of the chemical shift. The error values reported in this paper are calculated using the RMS distance metric analysis approach introduced and discussed in detail by Alderman et al.[23] and Grant and Halling.[116]

Theoretical Chemical Shift Data

The theoretical chemical shift tensor principal values for the ethylenic and CH carbon atoms for TTF and $[TTF]_2^{2+}$ are reported in Tables 9 and 10. These calculated chemical shift tensor principal values were calculated using the Gaussian03 suite[5] of programs at the B3LYP/6-311+G** level of theory and the GIAO method used to calculate chemical shielding tensors. Other methods, levels of theory, and basis sets were also used in this study, and the results are provided as supplemental information. The theoretical chemical shielding values where fit with a linear least-squares fit to the experimental chemical shift values and converted into chemical shift values using the equation of the line produced. The theoretical isotropic chemical shift values for TTF are 111.2 ppm for the ethylenic carbon atoms and 120.3 ppm for the CH carbon atoms. The theoretical isotropic chemical shift values for $[TTF]_2^{2+}$ are 147.1, 144.4, 140.2, and 135.1 ppm for the ethylenic carbon atoms and 138.2, 136.6, 136.5, 136.4, 134.3, 131.3, 129.5, and 128.7 ppm for the CH carbon atoms. The crystal structure used in the calculations and the numbering scheme used in Table 10 for $[TTF]_2^{2+}$ is given in Figure 25.

The DFT Kohn-Sham orbitals and chemical shielding tensors for TTF and $[TTF]_2^{2+}$ are first calculated for their isolated systems using crystallographic structural information, optimizing the protons. The calculated chemical shielding principal values are compared to the experimental chemical shift principal values for both TTF and

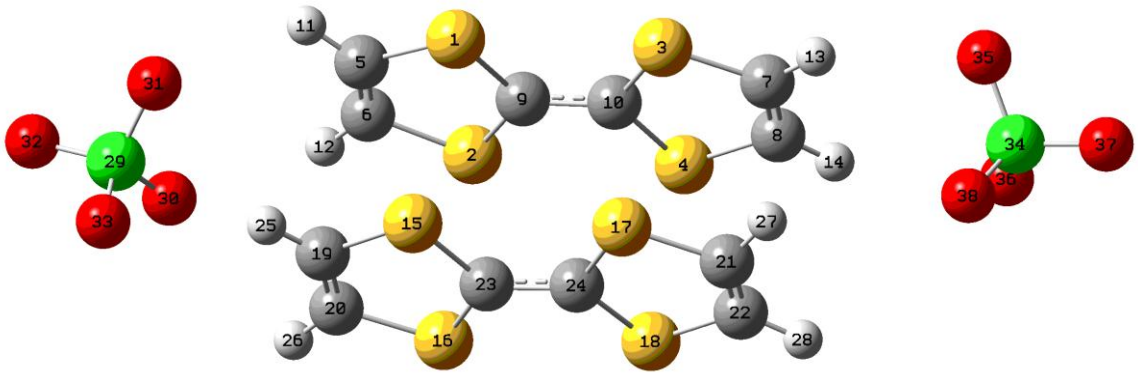

Figure 25. Diagram of the crystal structure used in all calculations for $[TTF]_2^{2+}$ taken directly from X-ray data.[123] The numbering scheme used in Table 9 refers to the numbers in this Figure. The two $[TTF]^+$ cations are parallel to each other with a slight glide plane distortion.

$[TTF]_2^{2+}$ in Figure 26. The linear least-squares fit has the form of:

$$\sigma^c_{ii} = m\delta^e_{ii} + \sigma_{ref} \quad (40)$$

where σ^c_{ii} is the calculated chemical shielding tensor value, δ^e_{ii} is the experimental chemical shift tensor value, m = the slope (-1.02 in Figure 26), σ_{ref} is the isotropic chemical shielding value of the reference compound, TMS (182.6 ppm in Figure 26). This linear least-squares fit was used to convert the calculated chemical shielding tensors into chemical shift values[62] and the results are reported in Tables 9 and 10 for TTF and $[TTF]_2^{2+}$. A linear least-squares approach is used to minimize the systematic errors in the theory. The experimental and theoretical chemical shift principal values agree by ±3.8 ppm. The embedded-ion method was used to study any long range electrostatic that might affect the chemical shifts. In this case, due to lattice symmetry, the effects of the long-range electrostatic fields cancel when the shifts are computed. This conclusion gives no information on long-range magnetic susceptibilities effects.

The chemical shielding tensor calculations for $[TTF]^+$ are performed using the same levels of theory and basis sets as TTF and $[TTF]_2^{2+}$. The main differences between $[TTF]^+$ and the other two systems is that the charge on the overall system of $[TTF]^+$ is 1+ and the multiplicity of the calculation is 2. Unrestricted DFT was used in the $[TTF]^+$ calculations. The hydrogen atom positions were optimized and then the chemical shielding tensors were calculated using the GIAO method. The $[TTF]^+$ results were converted from chemical shielding values into chemical shift values using the linear

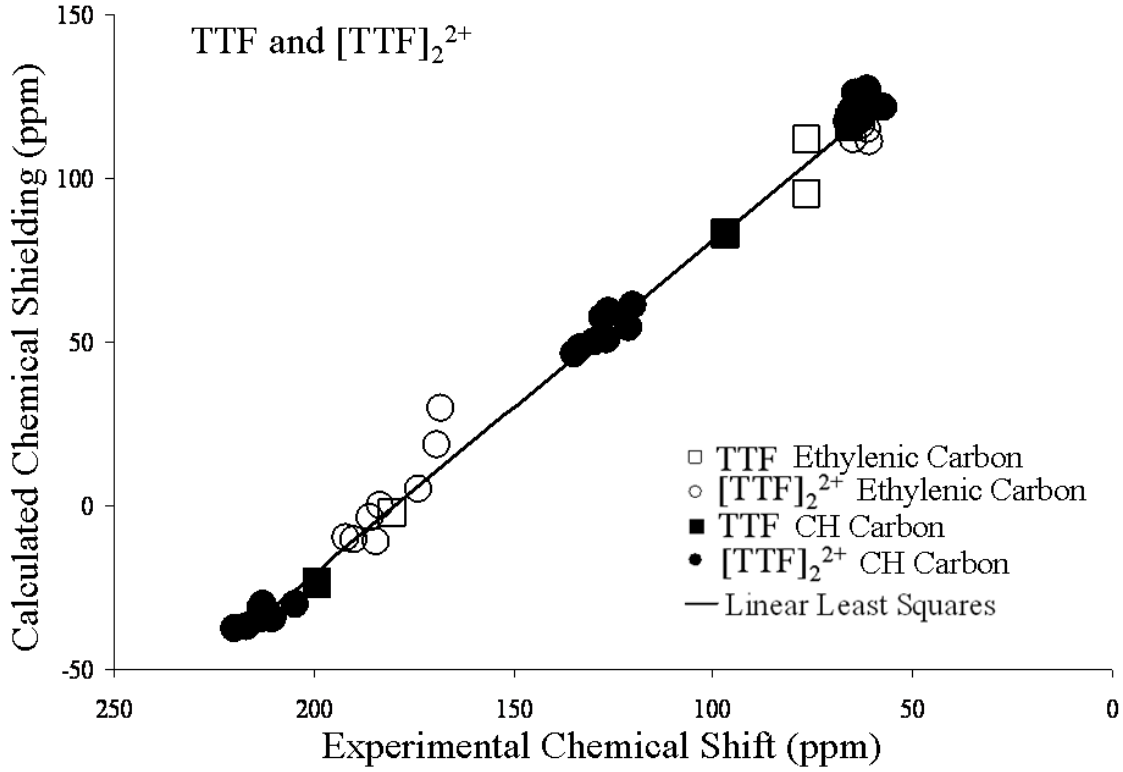

Figure 26. Calculated chemical shielding tensor principal values vs. experimentally measured chemical shift principal values in TTF and in $[TTF]_2^{2+}$ dimer dication. The calculated values were performed using DFT and the least-squares fit was done to minimize systematic errors in the calculations. Note that the $[TTF]_2^{2+}$ open circles have the greatest deviation. These entries are for carbons in the weak bond that may be influenced by long range shielding (i.e., magnetic susceptibility type) factors due to the highly polarized nature of the four weakly bonded carbon electrons.[157]

least-squares line calculated from TTF and $[TTF]_2^{2+}$ for each level of theory and basis set. The results using UB3LYP/6-311+G** are given in Table 11. The other results are given as supplemental information. The results for $[TTF]^+$ were used to understand the changes in the chemical shift principal values due to oxidation of TTF.

^{13}C Chemical Shift Tensors

Oxidation of TTF to $[TTF]_2^{2+}$ has a profound effect on the principal shift values of the central, ethylenic, carbon atoms. The orientation of the principal shift values in planar π-bonded systems, such as planar aromatic hydrocarbons and olefins, is set by the local symmetry of the ^{13}C. The $[TTF]_2^{2+}$ forms two parallel dication molecular planes. It has an intradimer distance of 3.4 Å, less than the van der Waals radii for sulfur atoms of 3.6 Å.

The weak, multicenter intradimer bonding involves the carbon atoms and the π-electrons in the sulfur atoms. The presence of relatively narrow NMR signals support the existence of a diamagnetic dimer, π-$[TTF]_2^{2+}$, in contrast to that expected for the paramagnetic monomer. A paramagnetic monomer would introduce strong spin-spin interactions between the free electrons and the carbon nuclei with broadening and shifting of the NMR signal beyond detection limits.[158,159] In accord with earlier work this observation suggests that the long π-bond pairs the two electrons in the overlapping π□-orbitals. This conclusion agrees with the magnetic susceptibility data that confirms the singlet ground state for the π-$[TTF]_2^{2+}$ dimer species.

Table 11. TTF^+ theoretical chemical shift tensor data.

$[TTF]^+$	Theoretical Chemical Shift (Using 6-311+G** Basis Set)		
Carbon	δ_{11}	δ_{22}	δ_{33}
Ethylenic	195.4	185.3	70.5
	193.7	180.1	71.7
CH	209.5	124.1	59.8
	209.3	126.8	61.2
	208.1	123.0	65.6
	209.8	124.4	59.6

The assignment of the principal components to δ_{11}, δ_{22}, and δ_{33} is supported by an acceptable agreement between the experimental and theoretical data and are described in Figure 27. The electronic currents in the plane perpendicular to a principal shielding component dominate the assignment of the chemical shift. Thus, the principal shift components represent a sensitive spatially resolved description of the three-dimensional electronic structure.[23] The δ_{11} and δ_{22} chemical shift tensor components lie in the molecular plane of TTF and $[TTF]_2^{2+}$, while δ_{33} is perpendicular to the molecular plane. Thus, the δ_{11} and δ_{22} components of the chemical shift tensor mainly arise from paramagnetic orbital contributions involving π-electrons and result from magnetic-field mixing of excited-state and ground-state wave functions that are connected by dipolar allowed transitions.[160]

The overall agreement between experimental and calculated chemical shift principal values is somewhat surprising considering the large shift variations encountered in this study. The electronic structure must change appreciably to account for the magnitude of these structural and shielding variations. The experimental and theoretical chemical shift tensors of TTF and $[TTF]_2^{2+}$ are reported in Tables 9 and 10 while the theoretical chemical shift tensors of $[TTF]^+$ are reported in Table 11. These results reveal highest variability in the two components in the molecular plane. The variability is due to changes in the chemical shift components in TTF upon oxidation to $[TTF]_2^{2+}$. This is confirmed by the large change associated with oxidation of TTF to $[TTF]^+$. The largest

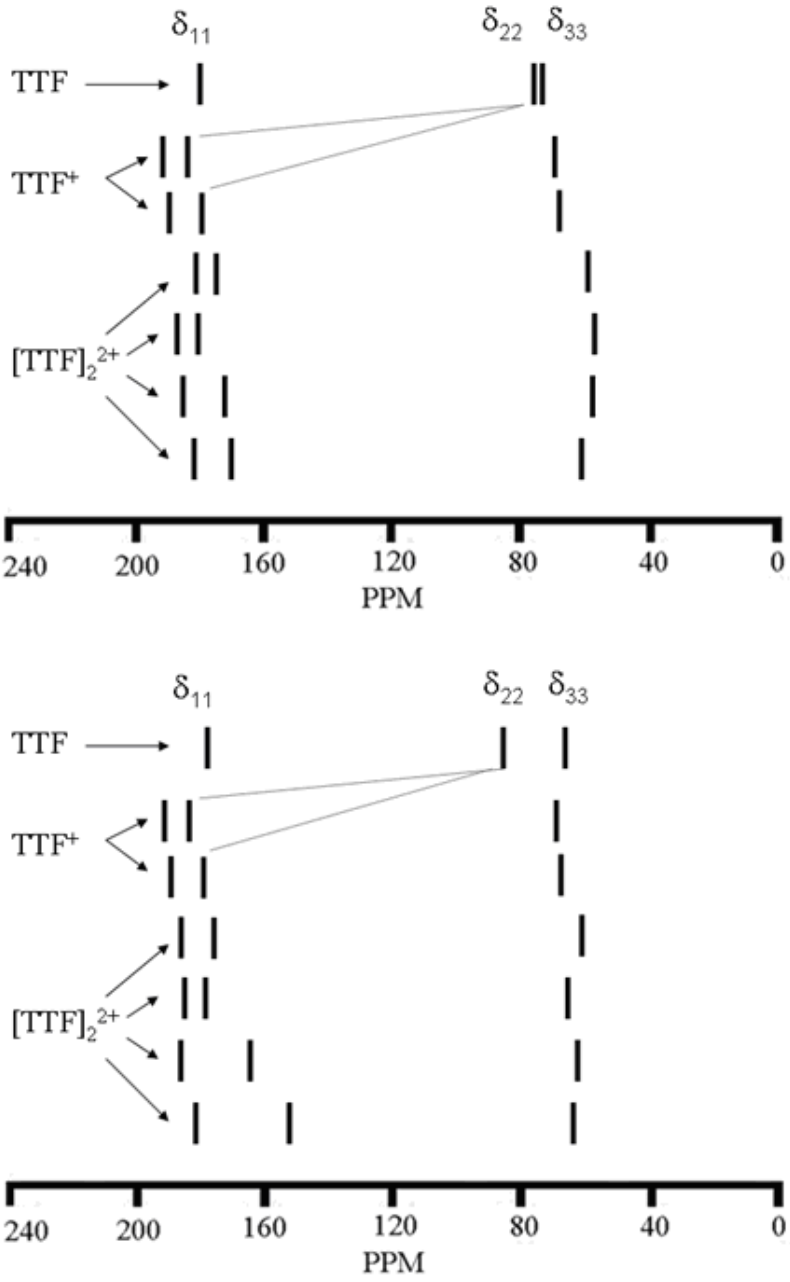

Figure 27. Experimental (only theoretical data is represented for TTF^{+}) and theoretical ethylenic ^{13}C chemical shift principal components of TTF, TTF^{+}, and $[TTF]_2^{2+}$.

change in ethylenic carbon chemical shift is seen in the component δ_{22}, and is observed to be approximately 100 ppm. The δ_{11} component, lying within the molecular plane and perpendicular to the δ_{22} component, exhibits a change in chemical shift of approximately 5-10 ppm. However, the out-of-plane component δ_{33} shows a change in chemical shift of approximately –12 to –15 ppm. The theoretically determined chemical shift principal components undergo a similar shift upon oxidation from TTF to $[TTF]^{+}$ with their change in shift values of approximately 15, 100, and 1 ppm for $\Delta\delta_{11}$, δ_{22}, and δ_{33}, respectively. The difference between theoretical chemical shift principal values upon oxidation from TTF to $[TTF]_2^{2+}$ change by approximately 7 ± 4, 85 ± 15, and 0 ± 4 ppm for $\Delta\delta_{11}$, δ_{22}, and δ_{33}, respectively. TTF is similar to TCNE in that upon electron transfer, both compounds experience large changes in the ethylenic ^{13}C δ_{11} and δ_{22} chemical shift components lying in the molecular plane and perpendicular to the δ_{33} component. While TTF does not experience the dramatic inversion of principal components like TCNE upon electron transfer, the dramatic shift in δ_{22} component in TTF is attributed to intradimer π-electron interactions similar to those found in reduced TCNE. These, however, are not solely localized to the ethylenic carbon atoms like they are in reduced TCNE, but they are distributed among the sulfur atoms forming multicenter intradimer bonds in $[TTF]_2^{2+}$.

The oxidation of TTF to $[TTF]_2^{2+}$ also affects the chemical shift principal values of the CH carbon atoms, but to a lesser extent than the effects seen in the ethylenic carbon atoms and is described in Figure 28. The change in experimentally observed chemical shift components due to oxidation from the neutral TTF to $[TTF]_2^{2+}$ are approximately 14 ± 7, 31 ± 7, and 3 ± 4 ppm for δ_{11}, δ_{22}, and δ_{33}, respectively. The theoretically determined chemical-shift principal components undergo a change in shift

values of approximately 10, 28, and – 4 ppm for δ_{11}, δ_{22}, and δ_{33}, respectively, in oxidation from TTF to $[TTF]^{+}$. The change in theoretical principal values due to oxidation from TTF to $[TTF]_2^{2+}$ change by approximately 15 ± 3, 31 ± 7, and 5 ± 5 ppm for δ_{11}, δ_{22}, and δ_{33}, respectively. The smaller change in chemical shift of the CH carbon atoms is due to their not participating as much in the weak intradimer bonding that the ethylenic carbons participate in.

Population Analysis

A natural population analysis (NPA) charge and bond-order treatment was performed for TTF and $[TTF]_2^{2+}$. This was done to aid interpretation of the electronic structure through charge and bond-order calculations performed on the isolated molecules. Earlier theory has shown that DFT cannot account for the van der Waals stabilization that is needed to compute accurate bond energies in long bonds.[126] As such, a bond-order analysis using DFT will likely underestimate the intercation attractive forces. To confirm the intermolecular interactions, MP2/6-311+G** bond-order calculations were performed on TTF, $[TTF]_2^{2+}$, and two TTF molecules interspaced equivalent to $[TTF]_2^{2+}$. The theoretical NPA atomic charges and the Wiberg[161] bond orders are given in Figure 29 for the isolated molecules.

The bond order for the ethylenic C-C bond changes from 1.75 in TTF to 1.37 in $[TTF]_2^{2+}$ upon oxidation. The bond order for the ethylenic carbon-sulfur single bond increases from 0.99 in TTF to 1.13 in $[TTF]_2^{2+}$. The other bond orders remain

Figure 28. Experimental (only theoretical data is represented for TTF^{+}) and theoretical CH ^{13}C chemical shift principal components of TTF, TTF^{+}, and $[TTF]_2^{2+}$.

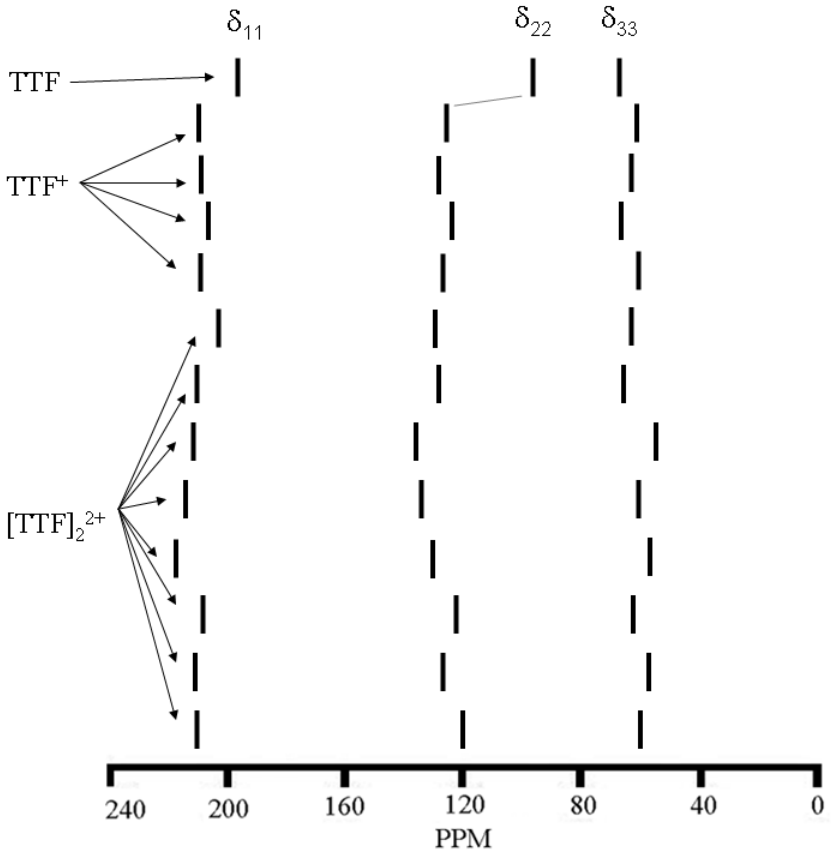
δ11
δ22
δ33
TTF
TTF+
[TTF]2 2+
240
200
160
120
80
40
0
PPM

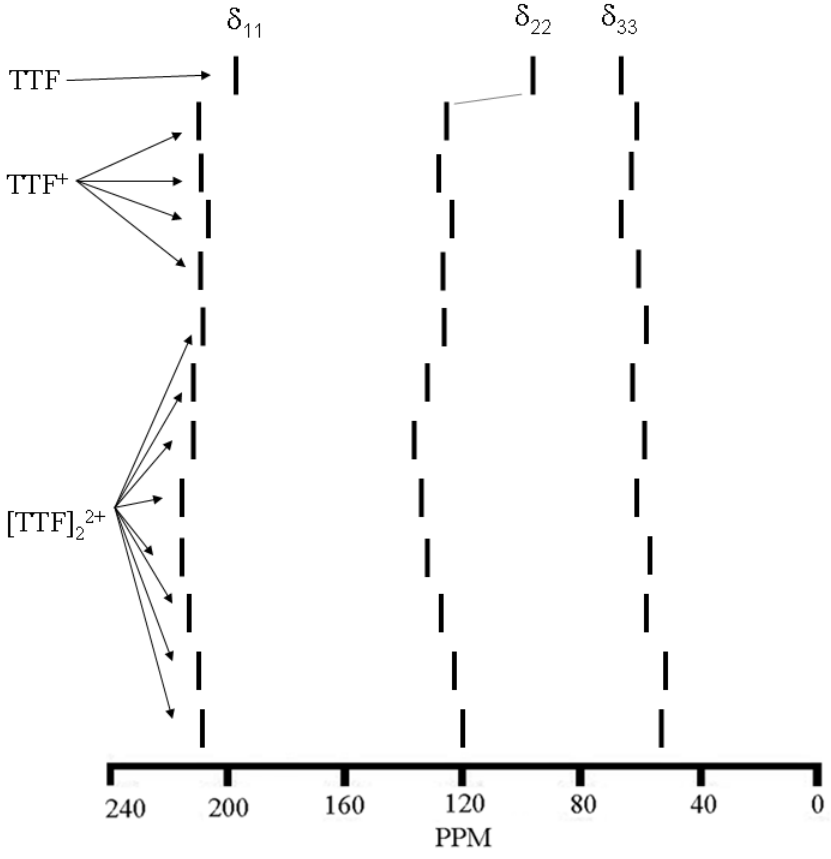
δ11
δ22
δ33
TTF
TTF+
[TTF]2 2+
240
200
160
120
80
40
0
PPM

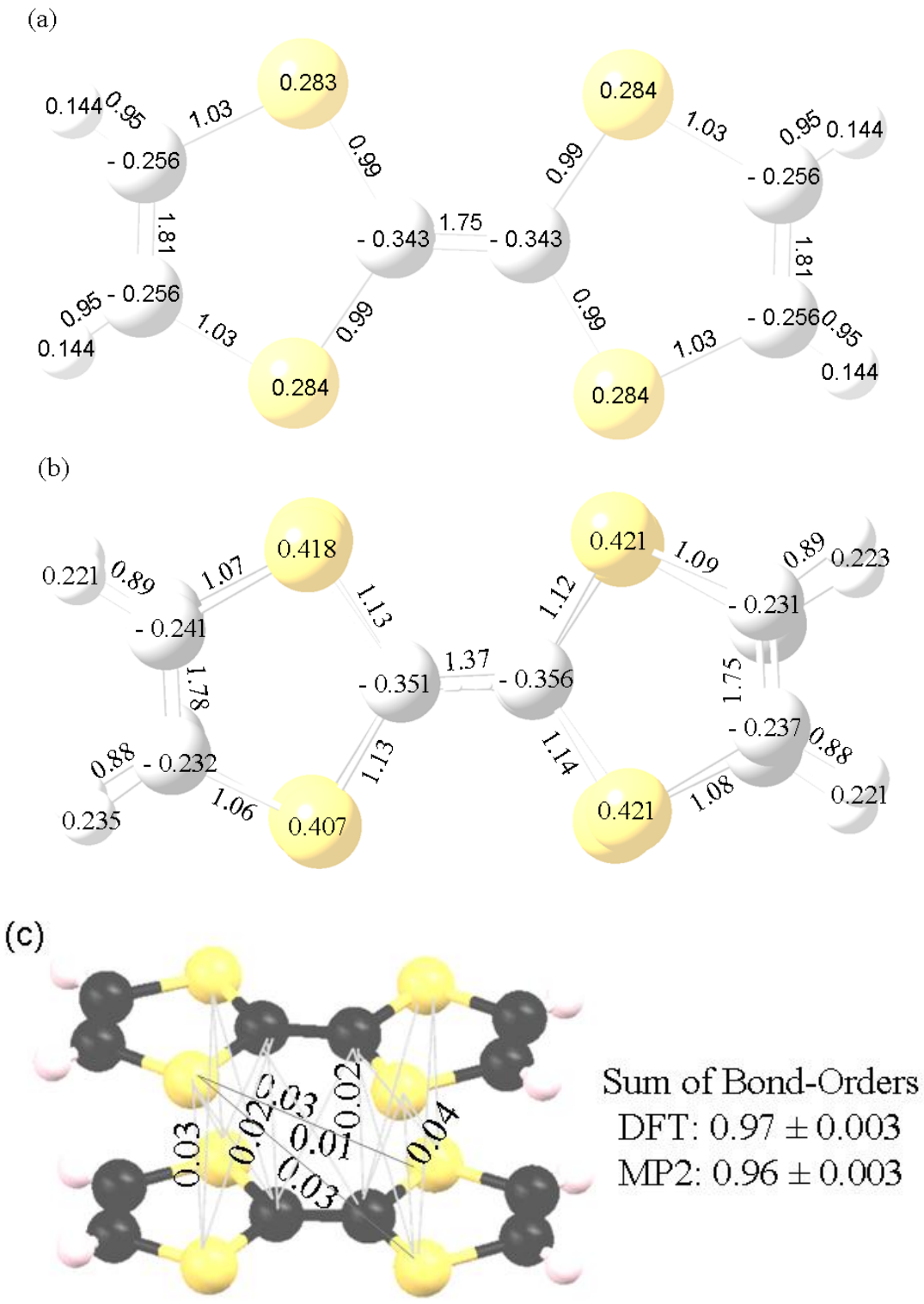

Figure 29. The natural atomic charges and Wiberg bond orders for (a) TTF, (b) $[TTF]_2^{2+}$, and (c) intradimer bond orders for $[TTF]_2^{2+}$. The numbers reported are rounded to two decimal places because of the uncertainty of the bond-orders is ± 0.002 due to random errors.

approximately equivalent during oxidation. There is a weak, yet significant, inter-cation bond-order occurring between the two $[TTF]^{+}$ cation planes. Although the individual intradimer bond-orders range from 0.01 to 0.04, their sum is 0.97 using DFT and 0.96 using MP2 level calculations. While these interactions are small individually, collectively they give a bond order similar to that of a single bond with $2e^{-}$. The sum of the bond-orders between two TTF molecules interspaced equivalent to $[TTF]_2^{2+}$ was zero, indicating that no long bonds were present. These resulting bond-order calculations assure that all of the bond-orders are properly scaled.

Chemical shifts are influenced by the interaction of many molecular orbitals. This is in contrast to optical spectroscopy which usually is influenced most by the HOMO and LUMO. In the case of $[TTF]_2[ClO_4]_2$, there are 785 total molecular orbitals and are made up of 587 unoccupied Rydberg orbitals, 128 valence molecular orbitals, including 45 anti-bonding orbitals, 45 bonding orbitals, and 38 lone-pair electron orbitals and 70 inner core orbitals. These details are summarized in Table 12. The intricate details of these 785 molecular orbitals are not discussed as such information would be beyond the scope of this paper. The embedded ion method (EIM) was used to investigate the electrostatic lattice potential in $[TTF]_2[ClO_4]_2$. Lattice symmetry minimizes the magnitude of the effects of the ionic charges of the ClO_4^{-} anions.

Conclusions

The chemical shift tensor principal values of the ethylenic and CH carbon positions in TTF and $[TTF]_2^{2+}$ have been measured using the FIREMAT experiment. Systematic EIM-DFT and isolated molecule DFT chemical shielding tensor calculations

Table 12. Molecular orbitals and the contribution to chemical shift.[a]

Number of Mos	Element	Shell	Energy (Hartrees) Avg/Range	Occupancy (# of e⁻) Avg/Range	Contribution to ^{13}C Chemical Shifts
Unoccupied Rydberg Orbitals[b]					
42	Cl		0.46–206	0.00	Negligible
167	S		0.34–187	0.00	Negligible
136	O		0.56–48.1	0.00	Negligible
202	C		0.43–23.4	0.00	Negligible
40	H		1.0–2.3	0.00	Negligible
Valence Molecular Orbitals[c]					
Unoccupied Anti-bonding Mos					
8	C–H	L shell (2s,2p)	0.36	0.019	Significant
8	Cl–O		0.3	0.23	Insignificant[d]
18	S–C	L shell (2s,2p)	0.10–0.13	0.022–0.043	Significant
11	C–C	L shell (2s,2p)	-0.22–0.62	0.018–0.87	Significant
Occupied Bonding Mos					
11	C–C	L shell (2s,2p)	-0.91– -0.40	1.79–1.99	Significant
8	C–H	L shell (2s,2p)	-0.63	1.97	Significant
18	S–C	L shell (2s,2p)	-0.82– -0.76	1.98	Significant
8	Cl–O		-1.05	1.99	Insignificant[d]
Lone-Pairs of Electrons					
24	O	L shell (2p)	-0.81– -0.28	1.84–1.99	Insignificant[d]
14	S	M shell (3p)	-0.76– -0.36	1.59–1.97	Significant[e]
Inner Core Orbitals[f]					
32	S	L shell (2s,2p)	-9.0– -6.0	2.00	Negligible
8	Cl	L shell (2s,2p)	-10.7– -7.5	2.00	Negligible
12	C	K shell (1s)	-10.2	2.00	Negligible
8	O	K shell (1s)	-18.9	2.00	Negligible
8	S	K shell (1s)	-87.8	2.00	Negligible
2	Cl	K shell (1s)	-100.6	2.00	Negligible

[a]Effect on carbon nuclei in the presence of a magnetic field.

[b]All Rydberg shells are those orbitals higher in energy than the Valence Molecular Orbitals.

[c]These orbitals are used to compute the paramagnetic shieldings and designated as significant.

[d]The effect of the perchlorate anions on the ^{13}C chemical shift is insignificant due to symmetry charge distribution in the Ewald electrostatic terms and gives a negligible contribution to the ^{13}C chemical shielding.

[e]The lone-pairs of electrons on sulfur play an important role in charge distribution and electron density. These charges will alter the electric polarization of the moiety and effect the chemical shifts.

[f]These are marked as negligible because closed shells have no paramagnetic term and the diamagnetic term is invariant to the selected reference compound (i.e., TMS).

provide a detailed investigation of orientation of chemical shift principal values with respect to the molecular frame. The experimental chemical shift principal values agree with the calculated quantum mechanical chemical shielding principal values, within typical errors commonly seen for this class of molecular system. The error in the correlation between experiment and theory is due to systematic errors inherent to DFT theoretical chemical shielding tensor calculations. Relatively weak Wiberg bond orders between the two $[TTF]^{+}$ components of the dimer dication correlate with the weak bonds linking the two $[TTF]^{+}$ cations and substantiate the claim that there are weak, multicenter bonds present. Further information is included in the following supplemental tables, Tables 13-15.

Table 13. Comparison between calculated and experimental chemical shifts in TTF. All chemical shift values in ppm referenced to TMS. Error values for each carbon are given in units of ppm^2.

			B3LYP		
		Experiment	Calc Shift D95**	Calc Shift 6-311+g**	Calc Shift cc-pVDZ
C1	δ_{11}	180.4	181.6	179.2	181.2
	δ_{22}	76.2	86.9	85.1	86.4
	δ_{33}	76.2	72.3	69.4	72.3
	δ_{iso}	110.9	Error: 21.8	Error: 17.0	Error: 19.4
C4	δ_{11}	198.9	198.0	199.3	198.3
	δ_{22}	96.6	96.9	96.4	96.4
	δ_{33}	65.9	62.8	65.5	63.4
	δ_{iso}	120.5	Error: 2.3	Error: 0.1	Error: 1.6
C6	δ_{11}	198.9	198.2	199.5	198.5
	δ_{22}	96.6	97.5	97.0	97.0
	δ_{33}	65.9	61.9	64.6	62.5
	δ_{iso}	120.5	Error: 3.2	Error: 0.3	Error: 2.3
C8	δ_{11}	180.4	181.6	179.2	181.2
	δ_{22}	76.2	86.8	85.1	86.4
	δ_{33}	76.2	72.4	69.4	72.4
	δ_{iso}	110.9	Error: 21.5	Error: 16.8	Error: 19.2
C11	δ_{11}	198.9	197.8	199.1	198.1
	δ_{22}	96.6	96.9	96.4	96.4
	δ_{33}	65.9	62.6	65.3	63.3
	δ_{iso}	120.5	Error: 2.8	Error: 0.1	Error: 1.9
C13	δ_{11}	198.9	198.0	199.3	198.3
	δ_{22}	96.6	97.2	96.8	96.7
	δ_{33}	65.9	62.0	64.7	62.6
	δ_{iso}	120.5	Error: 3.5	Error: 0.3	Error: 2.5
RMS Distance Metric Error (ppm):			3.0	2.4	2.8

Table 13. (Continued)

			B3PW91		
		Experiment	Calc Shift D95**	Calc Shift 6-311+g**	Calc Shift cc-pVDZ
C1	δ_{11}	180.4	180.2	178.1	179.9
	δ_{22}	76.2	87.1	85.3	86.4
	δ_{33}	76.2	70.2	67.8	70.5
	δ_{iso}	110.9	Error: 22.0	Error: 21.4	Error: 19.3
C4	δ_{11}	198.9	198.4	199.7	198.8
	δ_{22}	96.6	97.8	96.8	97.0
	δ_{33}	65.9	63.1	66.0	63.9
	δ_{iso}	120.5	Error: 1.5	Error: 0.2	Error: 0.7
C6	δ_{11}	198.9	198.7	200.0	199.0
	δ_{22}	96.6	98.4	97.4	97.6
	δ_{33}	65.9	62.2	65.1	63.0
	δ_{iso}	120.5	Error: 2.6	Error: 0.4	Error: 1.5
C8	δ_{11}	180.4	180.2	178.0	179.8
	δ_{22}	76.2	87.0	85.2	86.3
	δ_{33}	76.2	70.2	67.8	70.5
	δ_{iso}	110.9	Error: 21.7	Error: 21.2	Error: 19.1
C11	δ_{11}	198.9	198.2	199.6	198.6
	δ_{22}	96.6	97.8	96.8	97.0
	δ_{33}	65.9	62.9	65.8	63.8
	δ_{iso}	120.5	Error: 1.8	Error: 0.1	Error: 0.9
C13	δ_{11}	198.9	198.4	199.7	198.8
	δ_{22}	96.6	98.2	97.2	97.3
	δ_{33}	65.9	62.3	65.1	63.1
	δ_{iso}	120.5	Error: 2.6	Error: 0.3	Error: 1.5
RMS Distance Metric Error (ppm):			3.0	2.7	2.7

Table 14. Calculated chemical shifts of TTF^+. All chemical shift values in ppm referenced to TMS. Conversion from chemical shielding to chemical shift using least-squares fit line of TTF.

		UB3LYP			UB3PW91		
		Calc Shift D95**	Calc Shift 6-311+g**	Calc Shift cc-pVDZ	Calc Shift D95**	Calc Shift 6-311+g**	Calc Shift cc-pVDZ
C5	δ_{11}	202.5	195.4	200.6	201.0	194.1	199.1
	δ_{22}	199.6	185.3	194.4	196.8	183.0	191.6
	δ_{33}	70.6	70.5	70.3	70.7	70.5	70.2
C6	δ_{11}	200.6	193.7	198.8	199.2	192.4	197.3
	δ_{22}	193.6	180.1	188.9	190.9	177.9	186.2
	δ_{33}	71.9	71.7	71.7	72.1	71.8	71.7
C7	δ_{11}	209.0	209.5	209.6	209.3	209.9	210.1
	δ_{22}	128.8	124.1	127.2	130.2	125.2	128.3
	δ_{33}	56.1	59.8	56.7	56.4	60.3	57.3
C8	δ_{11}	208.7	209.3	209.5	209.0	209.7	210.0
	δ_{22}	131.9	126.8	130.3	133.3	128.0	131.4
	δ_{33}	57.7	61.2	58.3	58.2	61.7	58.9
C9	δ_{11}	207.0	208.1	207.9	207.4	208.5	208.4
	δ_{22}	128.2	123.0	126.4	129.5	124.1	127.4
	δ_{33}	62.1	65.6	62.7	62.6	66.2	63.4
C10	δ_{11}	208.9	209.8	209.6	209.2	210.2	210.1
	δ_{22}	129.8	124.4	127.9	131.1	125.6	128.9
	δ_{33}	55.8	59.6	56.5	56.2	60.1	57.1

Table 15. Comparison between calculated and experimental chemical shift tensors of $[TTF]_2^{2+}$. All chemical shift values in ppm referenced to TMS. Error values for each carbon are given in units of ppm^2.

			B3LYP			
		Experiment	Calc Shift 6-311g**	Calc Shift D95**	Calc Shift 6-311+g**	Calc Shift cc-pVDZ
C5	δ_{11}	204.7	211.4	203.5	210.4	205.5
	δ_{22}	127.6	123.1	126.4	124.0	121.5
	δ_{33}	64.0	60.6	57.1	59.4	60.2
C6	δ_{11}	210.2	214.5	205.5	214.7	201.9
	δ_{22}	126.6	131.3	136.7	130.6	134.5
	δ_{33}	66.3	64.8	61.0	64.2	64.5
C7	δ_{11}	212.3	216.5	207.8	214.9	212.0
	δ_{22}	134.4	134.0	136.4	135.0	130.4
	δ_{33}	57.1	59.9	57.0	60.1	59.9
C8	δ_{11}	216.4	229.5	228.8	217.5	270.5
	δ_{22}	133.0	133.9	136.8	133.1	129.1
	δ_{33}	62.6	63.5	60.1	63.9	63.0
C9	δ_{11}	184.1	190.8	195.0	191.5	192.0
	δ_{22}	173.5	172.7	183.7	175.9	171.3
	δ_{33}	62.8	66.4	66.2	65.7	67.7
C10	δ_{11}	191.6	188.7	199.0	190.3	211.1
	δ_{22}	183.3	184.0	192.7	180.5	188.0
	δ_{33}	60.9	71.9	71.6	70.3	72.8
C19	δ_{11}	219.5	218.0	209.3	217.8	209.0
	δ_{22}	129.6	128.9	130.8	131.3	123.9
	δ_{33}	60.5	60.5	57.7	60.2	60.5
C20	δ_{11}	210.7	214.2	207.1	215.2	205.7
	δ_{22}	121.1	125.2	127.3	126.7	123.2
	δ_{33}	65.5	60.9	57.9	61.0	60.6
C21	δ_{11}	212.9	212.9	204.9	211.9	205.7
	δ_{22}	126.1	122.2	124.6	122.1	122.5
	δ_{33}	61.4	54.7	51.3	54.3	54.3
C22	δ_{11}	212.6	209.1	200.6	210.4	197.6
	δ_{22}	120.0	119.4	121.8	120.1	118.9
	δ_{33}	64.4	56.0	52.7	55.7	55.6
C23	δ_{11}	189.9	188.3	191.9	191.4	186.7
	δ_{22}	169.1	158.6	169.0	162.2	159.8
	δ_{33}	61.1	67.5	67.4	67.1	68.9
C24	δ_{11}	185.9	183.5	187.6	184.1	186.6
	δ_{22}	167.9	146.5	157.0	151.3	147.6
	δ_{33}	64.9	70.9	70.4	69.9	71.7
RMS Error (ppm):			4.6	5.9	3.8	9.3

			B3PW91		
		Experiment	Calc Shift D95**	Calc Shift 6-311+g**	Calc Shift cc-pVDZ
C5	δ_{11}	204.7	204.5	211.6	206.5
	δ_{22}	127.6	126.4	124.1	121.4
	δ_{33}	64.0	57.4	59.7	60.7
C6	δ_{11}	210.2	206.0	215.6	201.9
	δ_{22}	126.6	137.2	130.7	134.6
	δ_{33}	66.3	61.7	64.7	65.2
C7	δ_{11}	212.3	209.1	215.8	213.6
	δ_{22}	134.4	136.0	134.9	130.2
	δ_{33}	57.1	57.3	60.3	60.5
C8	δ_{11}	216.4	235.4	219.7	277.4
	δ_{22}	133.0	136.1	133.3	127.7
	δ_{33}	62.6	60.7	64.2	63.6
C9	δ_{11}	184.1	192.9	190.2	190.2
	δ_{22}	173.5	180.3	174.2	168.2
	δ_{33}	62.8	66.3	65.4	67.5
C10	δ_{11}	191.6	199.2	189.0	212.5
	δ_{22}	183.3	190.6	179.5	185.9
	δ_{33}	60.9	71.6	70.0	72.6
C19	δ_{11}	219.5	210.0	218.4	209.2
	δ_{22}	129.6	130.7	131.3	124.2
	δ_{33}	60.5	58.0	60.6	60.9
C20	δ_{11}	210.7	207.7	215.9	205.8
	δ_{22}	121.1	127.5	126.8	123.6
	δ_{33}	65.5	58.3	61.1	61.1
C21	δ_{11}	212.9	205.8	212.7	206.2
	δ_{22}	126.1	124.9	122.5	122.5
	δ_{33}	61.4	51.6	54.7	54.7
C22	δ_{11}	212.6	201.0	211.0	197.8
	δ_{22}	120.0	122.1	120.4	119.2
	δ_{33}	64.4	53.0	56.1	56.1
C23	δ_{11}	189.9	190.0	190.1	184.9
	δ_{22}	169.1	166.4	160.7	157.3
	δ_{33}	61.1	67.5	66.9	68.7
C24	δ_{11}	185.9	186.4	183.1	185.1
	δ_{22}	167.9	154.5	149.8	145.4
	δ_{33}	64.9	70.4	69.9	71.6
RMS Error (ppm):			5.8	3.9	10.0

CHAPTER 5

SOLID-STATE ^{13}C NMR INVESTIGATIONS OF CYCLOPHANES: [2,2]PARAYCYCLOPHANE AND 1,8-DIOXA[8](2,7)PYRENOPHANE

Introduction

The discovery of fullerenes and their potential uses in science, medicine, and industry has led to increased efforts to understand the structural details of this class of molecules, including their structural moieties.[75,162,163,164] Many polycyclic aromatic hydrocarbons (PAHs) can be mapped onto the surface of fullerene molecules.[165] This is one reason why PAHs are of great interest to the scientific community. One interesting aspect of PAHs is that they are generally planar molecules. This planarity differs considerably from the curvature found in fullerene molecules.[97,98,99] There have been studies on the molecular strain on PAHs due to curvature.[64,165] One of the most sensitive means for determining strain in PAHs is solid-state NMR chemical shift tensors.

Solid-state NMR spectroscopy has the capability of providing full structural information with atom level resolution.[89] It has been used to identify various fullerene structures.[93,94] Chemical shift tensors have been used to determine many polycyclic aromatic hydrocarbon structures and provide useful information regarding their three-dimensional structure.[90,91,92] The chemical shift tensors provide electronic information

for each atom in a given molecule.[38] This information includes distortions in the electron configuration due to bonding and neighboring atoms, including variations in atomic orbitals due to strain. Molecular strain caused by curvature is typically most pronounced in the δ_{33} principal component in the chemical shift tensor.[64,165]

Three-dimensional curvature has been described using π-orbital axis vector (POAV) pyramidalization angles (θ_p) since 1986.[95,96] The POAV is defined as the vector which creates three equivalent angles ($\theta_{\sigma\pi}$) from bisecting the pyramid formed at the apex of an sp^2 carbon atom and its three protruding σ-bonds. θ_p is defined in Eq. 39. θ_p data have been reported for many curved molecules, including C_{60} and many PAHs.[97,98,99] A depiction of θ_p is given in Figure 12.

Cyclophane structures are of interest to researchers due to their aromatic qualities and their strained, curved structure.[166,167,168] Research has also predicted new possible synthetic routes for fullerene structures via cyclophane intermediates.[169] Many cyclophane structures have been synthesized and studied. One way to measure strain in cyclophane structure is to compare the curved cyclophane structure to that of its planar PAH constituent. This can be done by comparing energetic, geometric, and magnetic properties. In this study, comparisons of chemical shift tensors will be made between [2,2]paracyclophane and benzene as well as 1,8-dioxa[8](2,7)pyrenophane and pyrene. These comparisons will provide useful information regarding ring strain introduced by forcing curvature upon molecules that energetically prefer to be planar. This information should provide further understanding of aromatic fullerene and nanotube materials.

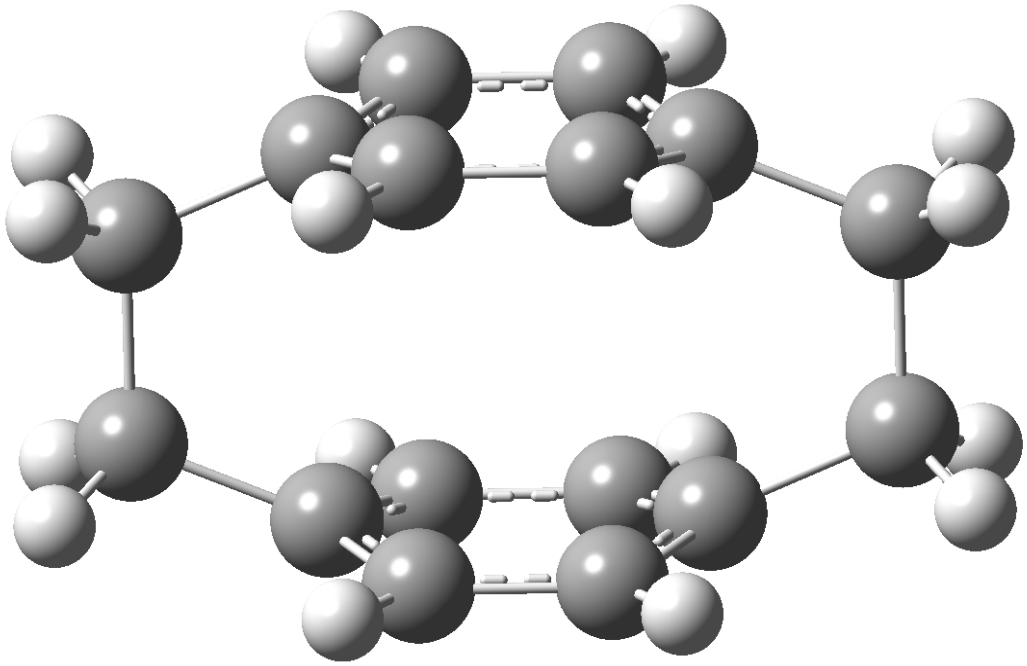

Figure 30. [2,2]Paracyclophane

[2,2]Paracyclophane is made up of two parallel benzene rings that are connected in a para- arrangement via $(CH_2)_2$ bridges as shown in Figure 30. These CH_2 bridges introduce curvature to both benzene rings. The crystal structure of [2,2]paracyclophane is known and originally reported by Lonsdale et al.[170] The crystal structure suggests that [2,2]paracyclophane belongs to the *P42/mnm* space group, has D_{2h} symmetry, and is in an eclipsed geometric configuration.[170] Theoretical studies have been performed, optimizing the energy of [2,2]paracyclophane in order to compare theoretical structures to experimental crystal structural data.[171]

1,8-Dioxa[8](2,7)pyrenophane is a cyclophane made up of one aromatic pyrene unit consisting of two carbon-oxygen bonds at the C2 and C7 positions. The oxygen atoms are cyclically connected by an aliphatic $(CH_2)_6$ bridge as shown in Figure 31. There is curvature in the pyrene moiety of 1,8-dioxa[8](2,7)pyrenophane due to the strain introduced by the aliphatic bridge.[172] The single crystal X-ray structural data for 1,8-dioxa[8](2,7)pyrenophane have been previously reported and deposited with the Cambridge Crystallographic Data Center.[172]

Experimental

Synthesis

The synthesis of 1,8-dioxa[8](2,7)pyrenophane was carried out by the Graham Bodwell laboratory group at Memorial University of Newfoundland. The details of the synthesis and the crystal structure of 1,8-dioxa[8](2,7)pyrenophane are reported in the literature.[172] The [2,2]paracyclophane sample was purchased from Aldrich.

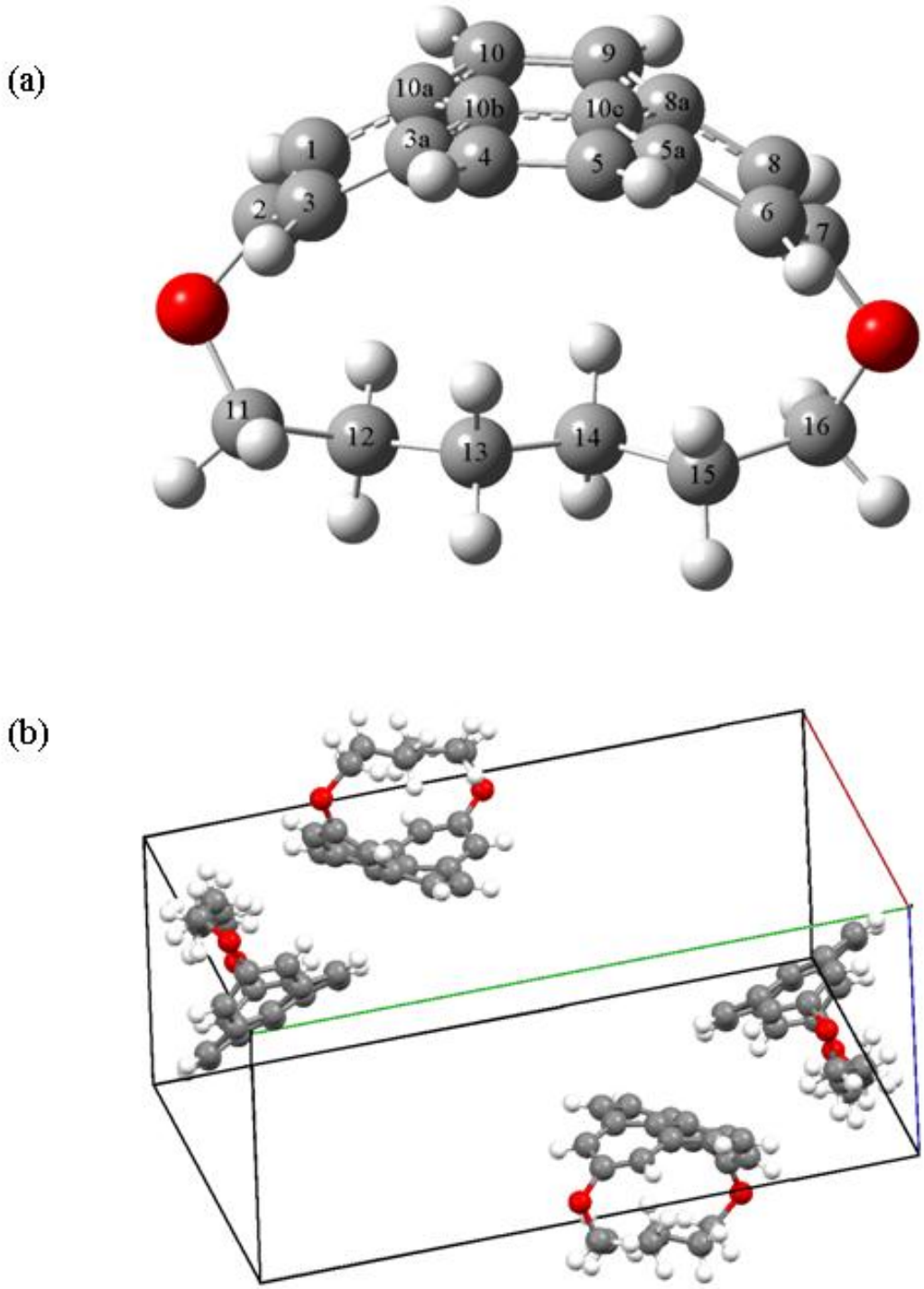

Figure 31. 1,8-Dioxa[8](2,7)pyrenophane (a) single molecule with numbering scheme and (b) unit cell containing four molecules.

Solid-state NMR

The ^{13}C FIREMAT data were collected on a CMX-400 NMR spectrometer operating at 400.119 MHz for ^{1}H and 100.622 MHz for ^{13}C, using a 7.5 mm PENCIL rotor probe. The methyl peak of hexamethylbenzene (HMB) at 17.35 ppm was used for referencing and setting the Hartmann-Hahn match.[105] All data were collected at room temperature.

[2,2]Paracyclophane

The FIREMAT data were collected utilizing a spinning speed of 1634 Hz and the FIREMAT pulse sequence. Other parameters include a recycle time of 400 s, a 4.10 μs ^{1}H 90° pulse, an 9.10 μs ^{13}C 180° pulse, a contact time of 3.0 ms, and spectral widths of 24.5098 and 55.5556 kHz in the evolution and acquisition dimensions, respectively. The analysis utilized 2048 transients collected during 15 evolution increments.

1,8-Dioxa[8](2,7)pyrenophane

The FIREMAT data were collected utilizing a spinning speed of 1634 Hz and the FIREMAT pulse sequence. Other parameters include a recycle time of 60 s, a 4.35 μs ^{1}H 90° pulse, a 9.50 μs ^{13}C 180° pulse, a contact time of 3.0 ms, and spectral widths of 24.5098 and 55.5556 kHz in the evolution and acquisition dimensions, respectively. The analysis utilized 2048 transients collected during 15 evolution increments.

Data Analysis

The 1D ^{13}C isotropic guide spectrum was derived in the prescribed manner from the FIREMAT data via Fourier transformation of the evolution points corresponding to the first acquisition point according to Gan's P2DSS suppression method.[15] Sideband

patterns for each of the isotropic values in the guide spectrum were calculated and fit using the TIGER processing method.[16]

Calculations

The calculations presented in this article used the X-ray data of [2,2]paracyclophane[170] and 1,8-dioxa[8](2,7)pyrenophane[172] as starting structural models. The crystal structures were refined by optimization of the hydrogen atom positions using the Gaussian03 suite of programs[5] using Density Functional Theory (DFT) with the B3LYP exchange and correlation functionals[108,109] as described by Cheeseman and co-workers,[110,111] along with the 6-311G** basis set,[112,113] following previously established precedents.[106,107] All of the chemical shielding calculations presented in this article were performed using the Gaussian03 suite[5] utilizing the same level of theory and basis set as those used in the crystal structure refinement process. The chemical shielding tensor principal values were calculated using the Gauge-Independent Atomic Orbitals (GIAO) method.[114,115]

Results and Discussion

The numbering scheme for 1,8-dioxa[8](2,7)pyrenophane are given in Figure 31. The FIREMAT spectra for [2,2]paracyclophane and 1,8-dioxa[8](2,7)pyrenophane are given in Figures 32 and 33, respectively. The experimental and theoretical chemical shift tensor principal values of [2,2]paracyclophane and 1,8-dioxa[8](2,7)pyrenophane are reported in Tables 16 and 17, respectively. The experimental carbon tensor assignments were made, aided by the theoretical chemical shielding results. All of the

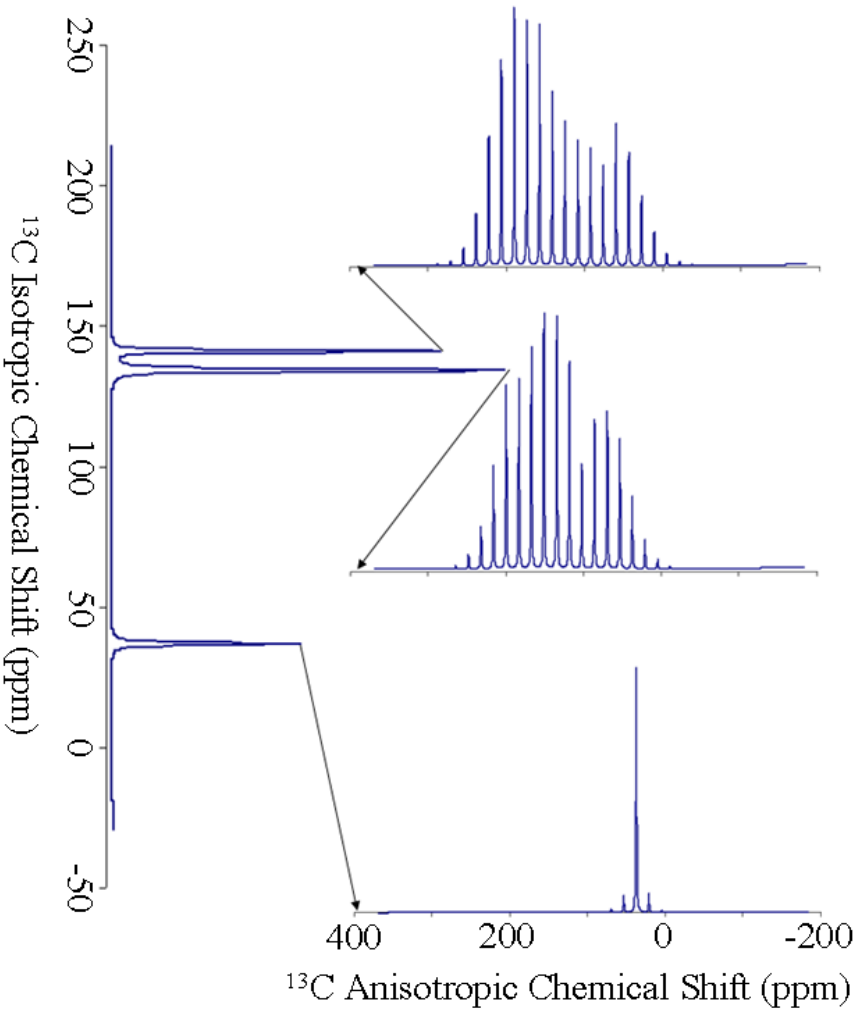

Figure 32. FIREMAT spectrum of [2,2]paracyclophane. The isotropic guide spectrum and the spinning sidebands for each carbon atom are represented along the y- and x- axes, respectively.

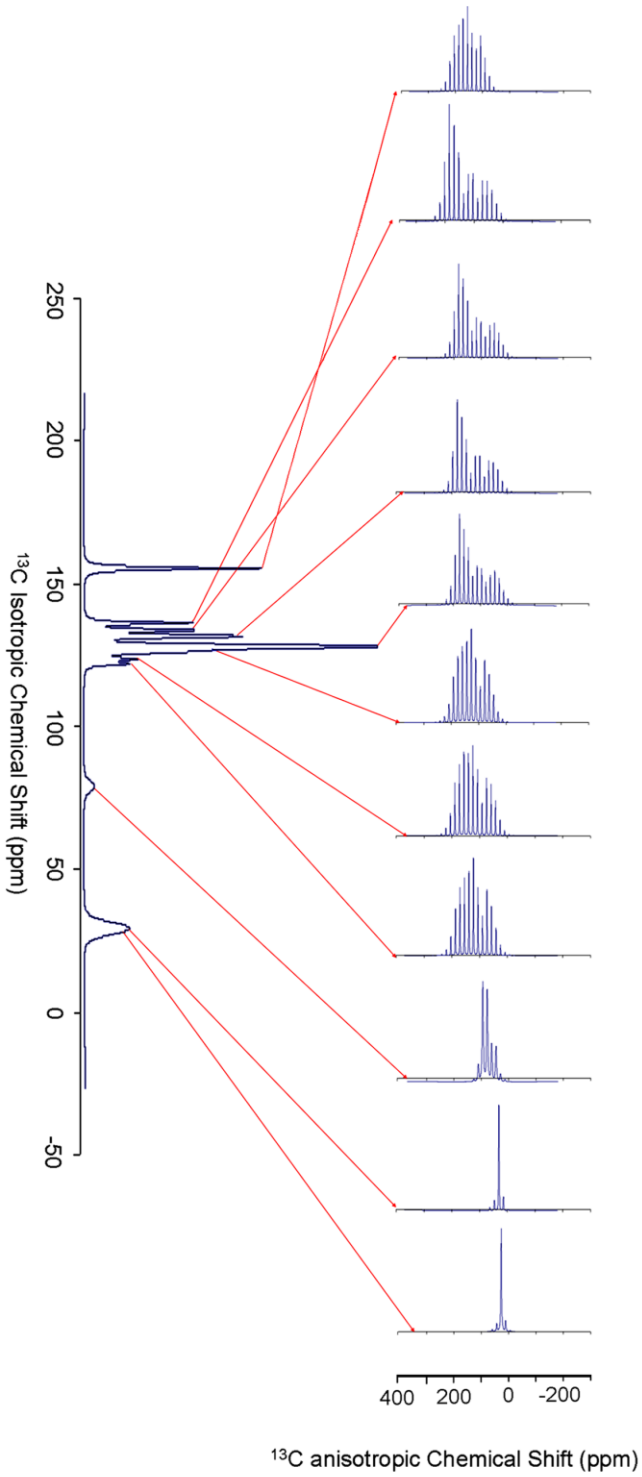

Figure 33. FIREMAT spectrum of 1,8-dioxa[8](2,7)pyrenophane. The isotropic guide spectrum and the spinning sidebands for each carbon atom are represented along the y- and x- axes, respectively.

Table 16. (2,2)Paracyclophane chemical shift tensor data.[a]

	Experimental Chemical Shift (ppm)			Theoretical Chemical Shift (ppm)		
Carbon	δ_{11}	δ_{22}	δ_{33}	δ_{11}	δ_{22}	δ_{33}
C	240.3	173.5	9.4	239.6	172.7	10.2
CH	231.6	148.2	23.4	234.8	143.4	22.5
CH2	52.0	35.6	23.3	55.2	39.1	22.3

[a]The RMS distance error between the experimental chemical shift and theoretical chemical shielding is ± 2.0 ppm.

Table 17. 1,8-Dioxa[8](2,7)pyrenophane chemical shift tensor data.[a]

	Experimental Chemical Shift (ppm)				Theoretical Chemical Shift (ppm)			
Carbon	δ_{11}	δ_{22}	δ_{33}	δ_{iso}	δ_{11}	δ_{22}	δ_{33}	δ_{iso}
C1	211.2	138.7	21.5	123.8	214.5	133.8	31.5	126.6
C2	233.4	163.0	69.6	155.3	231.3	164.0	68.1	154.4
C3	206.8	131.9	27.2	122.0	205.8	130.6	26.4	120.9
C3a	213.8	185.5	9.7	136.3	214.9	184.7	11.8	137.1
C4	211.7	138.0	31.1	126.9	216.4	126.4	31.1	124.6
C5	211.7	138.0	31.1	126.9	214.9	133.8	31.9	126.9
C5a	206.5	181.0	7.1	131.5	206.8	177.9	10.5	131.7
C6	211.2	138.7	21.5	123.8	215.9	135.7	32.6	128.1
C7	233.4	163.0	69.6	155.3	235.2	163.3	70.3	156.3
C8	206.8	131.9	27.2	122.0	201.6	125.1	25.4	117.3
C8a	213.9	178.2	9.1	133.7	209.7	180.9	4.6	131.7
C9	211.7	138.0	31.1	126.9	220.0	125.7	30.5	125.4
C10	211.7	138.0	31.1	126.9	219.3	127.7	30.8	125.9
C10a	206.5	181.0	7.1	131.5	207.2	182.2	6.7	132.0
C10b	211.9	171.6	0.8	128.1	202.8	190.8	-6.0	129.2
C10c	211.9	171.6	0.8	128.1	202.6	188.4	-5.6	128.5
C11	101.5	101.5	31.7	78.2	105.6	94.8	31.5	77.3
C12	45.0	21.3	15.3	27.2	43.1	30.5	10.8	28.1
C13	50.7	20.2	20.2	30.4	49.6	27.3	18.0	31.6
C14	50.7	20.2	20.2	30.4	46.9	25.8	12.4	28.4
C15	45.0	21.3	15.3	27.2	45.2	30.4	15.8	30.4
C16	101.5	101.5	31.7	78.2	109.4	93.2	32.1	78.2

[a] The RMS distance error between the experimental chemical shift and the theoretical chemical shielding is ± 4.2 ppm.

error values reported in this article are calculated using the RMS distance metric analysis approach introduced and discussed in detail by Alderman et al.[23] and Grant and Halling.[116] The error between experiment and theory for [2,2]paracyclophane is 2.0 ppm. The error between experiment and theory for 1,8-dioxa[8](2,7)pyrenophane is 4.2 ppm. The correlation between the experimental and theoretical data of [2,2]paracyclophane and 1,8-dioxa[8](2,7)pyrenophane is shown in Figure 34. These results show an excellent agreement between the theoretical and experimental data.[23,116] The NMR results for 1,8-dioxa[8](2,7)pyrenophane correlate well between experiment and theory. The model used for the hydrogen geometry optimization and the theoretical NMR chemical possess $P2_1/C$ space group symmetry.[172] One advantage of using solid-state NMR to analyze 1,8-dioxa[8](2,7)pyrenophane is that it provides more information regarding its three-dimensional structure than solution NMR. The FIREMAT experiment provides a means for obtaining three chemical shift principal values for each carbon atom position.[13] For both [2,2]paracyclophane and 1,8-dioxa[8](2,7)pyrenophane, the desire is to see how the chemical shift tensors compare to their planar PAH constituents, benzene and pyrene, respectively.[173] The depiction of the changes in each of the chemical shift principal components of the nonprotonated atoms for [2,2]paracyclophane and 1,8-dioxa[8](2,7)pyrenophane is given in Figure 35. The chemical shift principal components for benzene and pyrene are also included in Figure 35 for basis of comparison.[173]

The δ_{33} component of the chemical shift tensor has been observed to be the most sensitive to ring deformation in PAHs.[64] It has been reported that the greater the shift of

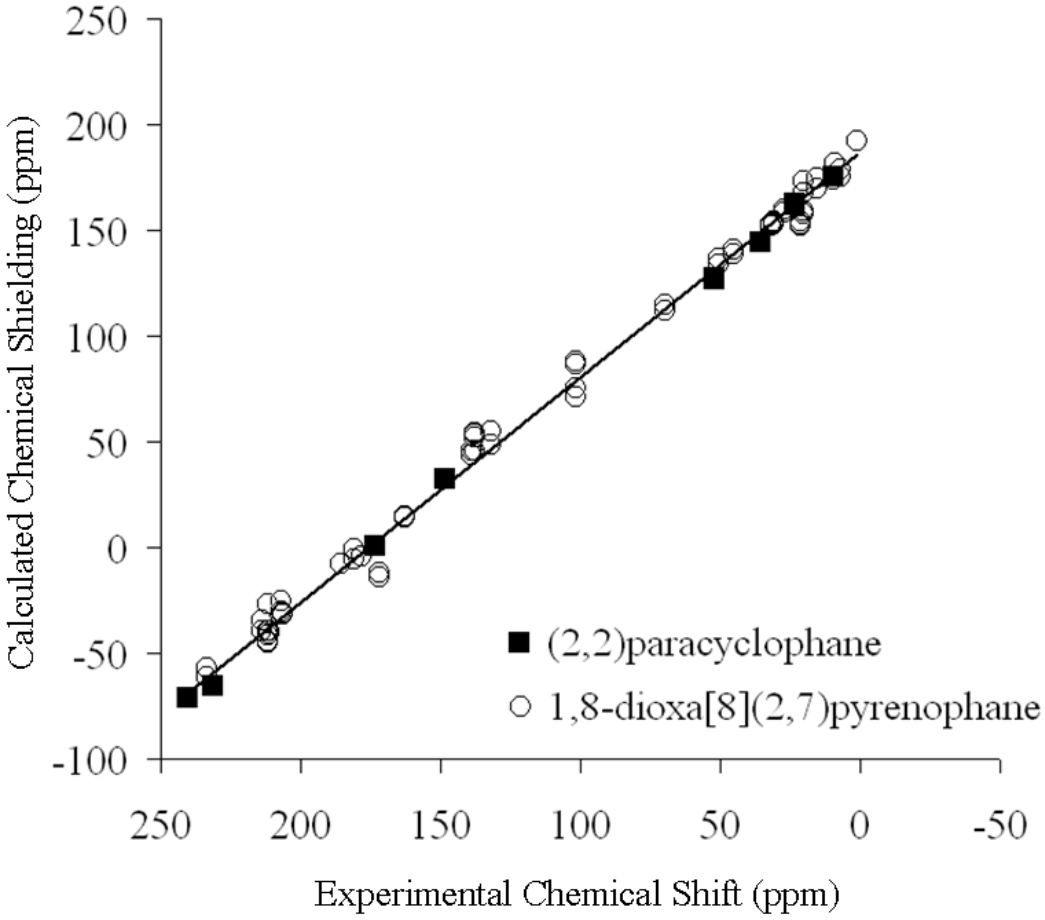

Figure 34. Correlation between theoretical chemical shielding and experimentally derived chemical shift for [2,2]paracyclophane and 1,8-dioxa[8](2,7)pyrenophane. The equation of the linear least-squares fit is $y = -1.06x + 186.4$. The R^2 value for the data is 0.996, indicating an excellent correlation between experiment and theory.

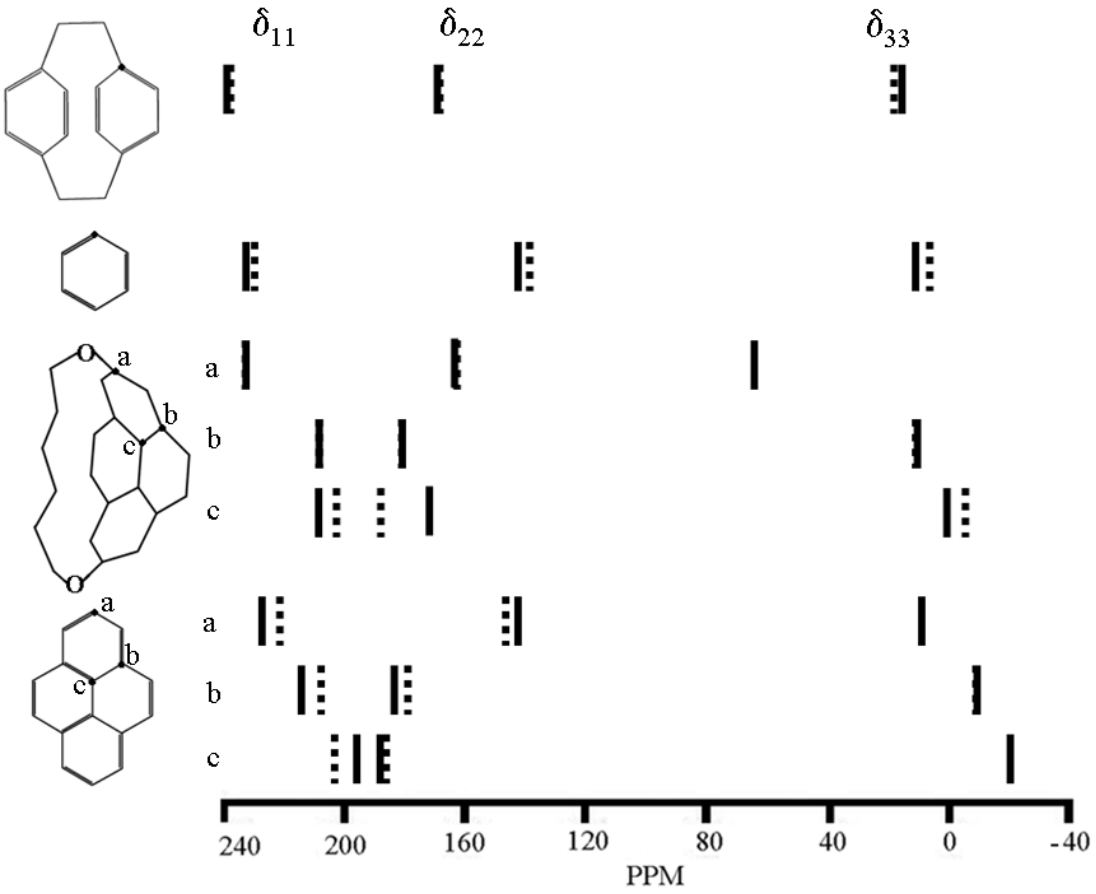

Figure 35. Experimental (—) and theoretical (----) ^{13}C chemical shift principal components for the nonprotonated carbon atoms in [2,2]paracyclophane and 1,8-dioxa[8](2,7)pyrenophane, as well as corresponding chemical shift components for benzene and pyrene given for a basis of comparison. The values for benzene and pyrene are reported by Facelli et al.[173]

the δ_{33} component signals the more curvature or strain.[165] These data show that the nonprotonated carbon atom in [2,2]paracyclophane is experiencing a larger amount of strain than the corresponding carbon atom in benzene. The C2 and C7 carbon atoms in 1,8-dioxa[8](2,7)pyrenophane are experiencing a δ_{33} shift of 69.6 ppm compared to a value shielding tensor calculations is that produced by X-ray crystallography and determined to of 4.0 ppm in pyrene for the corresponding carbon atom.[173] This indicates a large amount of strain in the pyrene aromatic ring constituent in 1,8-dioxa[8](2,7)pyrenophane caused by curvature. Theory also predicts ring strain with δ_{33} shift values of 68.1 and 70.3 ppm at the C2 and C7 positions of 1,8-dioxa[8](2,7)pyrenophane.

[2,2]Paracyclophane consists of slight curvature while 1,8-dioxa[8](2,7)pyrenophane consists of more pronounced curvature. The θ_p of the C2 and C7 carbon atoms in 1,8-dioxa[8](2,7)pyrenophane is 11.9°. The θ_p of the other nonprotonated carbon atoms in 1,8-dioxa[8](2,7)pyrenophane is approximately 5.4°. The curvature, θ_p, of C_{60} is 11.64°.[97] This indicates that the curvature of 1,8-dioxa[8](2,7)pyrenophane is approximately the same as that of C_{60} at the edges (C1-C3 and C6-C8). The center two aromatic rings of the pyrene constituent are nearly planar. The 69.6 ppm δ_{33} chemical shift principal component value of the C2 and C7 carbon atom positions is also considerably greater than the δ_{33} principal components in other strained carbon atoms in indenofluoranthene (40.9 ppm),[165] sumanene (32.8 ppm),[165] and C_{60} (41.8 ppm).[93,94] There is another contributing factor to such a high downfield shift, approximately 60 ppm, which is the adjacent oxygen atoms and their effect on the

chemical shift. Approximately 10 ppm of the downfield chemical shift in C2 and C7 can be attributed to ring strain due to curvature.

The crystal structure of pyrene shows that it is symmetrical while the crystal structure of 1,8-dioxa[8](2,7)pyrenophane shows a slight deviation from symmetry in the pyrene constituent. This is due to the lattice of the crystal structure which belongs to the $P2_1/C$ space group, indicating that the 22 carbon atoms are distinct and not related through symmetry. While each carbon atom is distinct, they are similar to one another, which is manifest in the closeness of the peaks in the FIREMAT guide spectrum. The crystal structure of 1,8-dioxa[8](2,7)pyrenophane also shows that the C1-C3 and C6-C8 carbon atom positions are the atoms with the most out of plain curvature. The NMR results also show that the C1-C3 and C6-C8 carbon atoms are undergoing a greater amount of strain than planar pyrene. The δ_{33} chemical shift component in the C1, C3, C6, and C8 protonated carbon atoms range from 21.5 and 27.2 ppm in experiment and range from 25.4 and 32.6 ppm in theory. The δ_{33} component of the chemical shift of the equivalent carbon atoms in pyrene is 19 ppm.[173] This downfield shift can be attributed to the strain associated with the curvature of 1,8-dioxa[8](2,7)pyrenophane.

The highly curved pyrene aromatic constituent of 1,8-dioxa[8](2,7)pyrenophane is created by the $O_2(CH_2)_6$ bridge that connects the pyrene at the C2 and C7 positions. This bridge is relatively short, which forces a large amount of curvature into the aromatic ring system at the edges. Since nearly all six-membered aromatic ring systems are planar, curvature introduces ring strain to the molecule. This dramatic effect can be seen clearly in the large difference in δ_{33} chemical shift tensors of 1,8-dioxa[8](2,7)pyrenophane and pyrene as shown in Figure 35. Because of the curvature in 1,8-dioxa[8](2,7)pyrenophane

and other pyrenophane molecules being similar to that found in C_{60}, the pyrenophanes have recently been proposed as a possible synthetic route for C_{60}.[169]

Conclusion

The SSNMR data for [2,2]parayclophane and 1,8-dioxa[8](2,7)pyrenophane provide structural information regarding three-dimensional shape and structure. This information includes chemical shift tensors, which give information about the three-dimensional chemical shift anisotropy of each carbon atom. The theoretical results aided in making experimental assignments of tensors. The substantially large downfield shift of the δ_{33} component of the chemical shift tensor for the C2 and C7 carbon atoms in 1,8-dioxa[8](2,7)pyrenophane indicates high ring deformation at that position. The 69.6 ppm δ_{33} shift is much farther downfield than the δ_{33} shift of indenofluoranthene, sumanene, and C_{60}. This indicates a great deal of ring strain at those positions. The POAV pyramidalization angles, θ_p, for the C2 and C7 carbon atoms in1,8-dioxa[8](2,7)pyrenophane also indicate a high amount of curvature. The SSNMR results for [2,2]parayclophane and 1,8-dioxa[8](2,7)pyrenophane reported in this paper are supported by excellent correlation with theoretical results.

REFERENCES

1 (a) Ramsey, N. F, *Phys. Rev.*, **1950**, *78*, 699-703; (b) Ramsey, N. F, *Phys. Rev.* **1952**, *86*, 243-246.

2 Brown, S. P.; Emsley, L. *Handbook of Spectroscopy*, Vo-Dinh, Gauglitz (eds); John Wiley & Sons: Chicester, U.K., **2003**; pp 269-326.

3 Grant, D. M. "Chemical Shift Tensors", D.M. Grant and R.K. Harris, Eds., *Encyclopedia of NMR*. **1996**, *2*, 1303. emrstm 0074

4 *Nuclear Magnetic Shieldings and Molecular Structure, NATO ASI Series C: Mathematical and Physical Sciences*, Vol. 386, Kluwer Academic Publishers, Dordrecht, The Netherlands, **1993**, edited by J.A. Tussell.

5 Gaussian03; Frisch, M. J.; Trucks, G. W.; Schlegel, H. B. *et al*. Gaussian, Inc.; Pittsburgh, PA, **1998** and **2003**.

6 Harris, R.K. *Solid State Nucl. Magn. Reson.* **1998**, *10(3)*, 177.

7 Bax, A.; Szeverenyi, N.M.; Maciel, G.E. *J. Magn. Reson*., **1983**, *52*, 147.

8 Grant, D.M. *Encyclopedia of NMR* eds. Grant, D.M.; Harris, R.K. John Wiley & Sons: Chichester, U.K.,**2002**; Vol. 9; pp 73-90.

9 Maricq, M.M.; Waugh, J.S. *J. Chem. Phys.* **1979**, *70*, 3300.

10 Herzfeld, J.; Berger; A.E. *J. Chem. Phys.* **1980**, *73*, 6021.

11 Bax, A.; Szeverenyi, N.M.; Maciel, G.E. *J. Magn. Reson.* **1983**, *51*, 400.

12 Gan, Z.; Grant, D.M.; Ernst, R.R. *Chem. Phys. Lett.* **1996**, *254*, 349.

13 Alderman, D.W.; McGeorge, G.; Hu, J.Z.; Pugmire, R.J.; Grant, D.M. *Mol. Phys.* **1998**, *95*, 1113.

14 Hu, J.Z.; Alderman, D.W.; Ye, C.; Pugmire, R.J.; Grant, D.M. *J. Magn. Reson. Ser. A.*, **1993**, *105*, 82.

15 (a) Gan, Z. *J. Am. Chem. Soc.* **1992**, *114*, 8307; (b) Gan, Z. *J. Magn. Reson*. **1994**, *109*, 253.

16 (a) McGeorge, G.; Hu, J.Z.; Mayne, C.L.; Alderman, D.W.; Pugmire, R.J.; Grant, D.M. *J. Magn. Reson.* **1997**, *129*, 134-144; (b) Manassen, Y.; Navon, G.; Moonen, C. T. W. *J. Magn. Reson*. **1987**, *72*, 551; (c) Manassen, Y.; Navon, G. *J. Magn. Reson*. **1988**, *79*, 291-298.

17 Ma, Z.; Halling, M.D.; Solum, M.S.; Harper, J.K.; Orendt, A.M.; Facelli, J.C.; Pugmire, R.J.; Grant, D.M.; Amick, A.W.; Scott, L.T. *J. Phys. Chem. A.* **2007**, *111*, 2020-2027.

18 Harper, J.K.; Barich, D.H.; Hu, J.Z.; Strobel, G.A.; Grant, D.M. *J. Org. Chem*., **2003**, *68*, 4609-4614.

19 Rienstra, C.M.; Tucker-Kellogg, L.; Jaroniec, C.P.; Hohwy, M.; Reif, B.; McMahon, M.T.; Tidor, B.; Lozano-Perez, T.; Gri¢ n, R.G. *Proc. Nat. Acad. Sci. U.S.A.*, **2002**, *99(16)*, 10260-10265.

20 Jaroniec, C.P.; MacPhee, C.E.; Bajaj, V.S.; McMahon, M.T.; Dobson, C.M.; Gri¢ n, R.G. *Proc. Natl. Acad. Sci. U.S.A.*, **2003**, *101*, 711-716.

21 Elena, B.; Pintacuda, G.; Mifsud, N.; Emsley, L. *J. Am. Chem. Soc*., **2006**, *128*, 9555-9560.

22 Harper, J.K.; Grant, D.M. *Crystal Growth & Design*, **2006**, *6(10)*, 2315-2321.

23 Alderman, D.W.; Sherwood, M.H.; Grant, D.M. *J. Magn. Reson. A.* **1993**, *101*, 188-197.

24 Dutour, J.; Guillou, N.; Huguenard, C.; Taulelle, F.; Mellot-Draznieks, C.; Férey, G. *Solid State Sci.* **2004**, *6(10)*, 1059.

25 Schmidt-Rohr, K.; Spiess, H. W. *Multidimensional Solid State NMR and Polymers*; Academic Press: San Diego, **1994**. HETCOR treatment

26 Lesage, A.; Auger, C.; Cadarelli, S.; Emsley, L. *J. Am. Chem. Soc*. **1997**, *119*, 7867.

27 Middleton, D. A.; Peng, X.; Saunders, D.; Shankland, K.; David, W. I. F.; Markvardsen, A. J. *Chem. Comm.* **2002**, 1976.

28 Pickard, C. J.; Salager, E.; Pintacuda, G.; Elena, B.; Emsley, L. *J. Am. Chem. Soc*., **2007**, *129(29)*, 8932.

29 Elena, B.; Emsley, L. *J. Am. Chem. Soc*. **2005**, *127(25)*, 9140.

30 Mifsud, N.; Elena, B.; Pickard, C. J.; Lesage, A.; Emsley, L. *Phys. Chem. Chem. Phys*. **2006**, *8(29)*, 3418

31 Harris, R. K.; Cadarelli, S.; Emsley, L.; Yates, J. R.; Pickard, C. J.; Jetti, R. K. R.; Greisser, U. J. *Phys. Chem. Chem. Phys.* **2007**, *9*, 360.

32 Heider, E. M.; Harper, J. K.; Grant, D. M. *Phys. Chem. Chem. Phys*. **2007**, *9*, 6083.

33 Harper, J. K.; Grant, D. M.; Zhang, Y.; Lee, P. L.; Von Dreele, R. *J. Am. Chem. Soc.* **2006**, *128(5)*, 1547.

34 Harper, J. K.; Mulgrew, A. E.; Li, J. Y.; Barich, D. H.; Strobel, G. A.; Grant, D. M. *J. Am. Chem. Soc*. **2001**, *123(40)*, 9837.

35 Harper, J. K.; Grant, D. M. *J. Am. Chem. Soc.* **2000**, *122(15)*, 3708.

36 Harper, J. K.; McGeorge, G.; Grant, D. M. *Magn. Reson. Chem.* **1998**, *36 (Spec. Issue)*, S135.

37 Harper, J. K.; Strohmeier, M.; Grant, D. M. *J. Magn. Reson*., **2007**, *189(1)*, 20.

38 Harper, J. K.; McGeorge, G.; Grant, D. M. *J. Am. Chem. Soc.* **1999** *121(27)*, 6488.

39 Harris, R. K. *Solid State Sciences*, **2004**, *6(10)*, 1025.

40 King, I. J.; Fayon, F.; Massiot, D.; Harris, R. K.; Evans, J. S. O. *Chem. Comm.*, **2001**, 1766.

41 Harris, R. K. "*Solid State Nucl. Magn*. *Reson.* **1998**, *10(3)*, 177.

42 Smith, E. D. L.; Hammond, R. B.; Jones, M. J.; Roberts, K. J.; Mitchell, J. B. O.; Price, S. L.; Harris, R. K.; Apperley, D. C.; Cherryman, J. C.; Docherty, R. *J. Chem. Phys. B*, **2001**, *105*, 5818.

43 Harris, R. K.; Ghi, P. Y.; Hammond, R. B.; Ma, C. Y.; Roberts, K. J.; Yates, J. R.; Pickard, C. J. *Magn. Reson. Chem.* **2006**, *44*, 325.

44 Yarim-Agaev, Y.; Tutunjian, P. M.; Waugh, J. S. *J. Magn. Reson.* **1982**, *47*, 51.

45 Tycko, R.; Dabbagh, G.; Mirau, P. *J. Magn. Reson.* **1989**, *85*, 265.

46 Gross, J. D.; Costa, P. R.; Griffin, R. G. *J. Chem. Phys.* **1998**, *108*, 7286.

47 Frydman, L.; Chingas, G. C.; Lee, Y. K.; Grandinetti, P. J.; Eastman, M. A.; Barrall, G. A.; Pines, A. *Isr. J. Chem.* **1992**, *32*, 161.

48 Frydman, L.; Chingas, G. C.; Lee, Y. K.; Grandinetti, P. J.; Eastman, M. A.; Barrall, G. A.; Pines, A. *J. Chem. Phys.* **1992**, *97*, 4800.

49 Hu, J. Z.; Wang, W.; Liu, F.; Solum, M. S.; DAlderman, D. W.; Pugmire, R. J.; Grant, D. M. *J. Magn. Reson. A* **1995**, *113*, 210.

50 Antzutkin, O. N.; Shekar, S. C.; Levitt, M. H. *J. Magn. Reson. A* **1995**, *115*, 7.

51 Liu, S. F.; Mao, J. D.; Schmidt-Rohr, K. *J. Magn. Reson*. **2002**, *155*, 15.

52 Chan, J. C. C.; Tycko, R. *J. Chem. Phys.* **2003**, *118*, 8378.

53 Hodgkinson, P.; Emsley, L. *J. Chem. Phys.* **1997**, *107*, 4808.

54 Sherwood, M. H.; Alderman, D. W.; Grant, D. M. *J. Magn. Reson*. **1989**, *84*, 466.

55 "Transformation matrix," Wikipedia, The Free Encyclopedia, http://en.wikipedia.org/w/index.php?title=Transformation_matrix&oldid=217772529

56 "Metric tensors," Wikipedia, The Free Encyclopedia, http://en.wikipedia.org/w/index.php?title=Metric_tensor&oldid=217103014

57 Griffin, R. G.; Ellett, Jr., J. D.; Mehring, M.; Bullitt, J. G.; Waugh, J. S. *J. Chem. Phys*., **1972**, *57*, 2147. This important reference treats *Directional Cosine Definition of Chemical Shift Tensors.*

58 Haeberlen, U. "*High Resolution NMR in Solids, Supplementa1"* in *Advances in Magnetic Resonance*, J. S. Waugh, Editor. Academic Press, New York, **1976**, pp 9.

59 Mehring, M., *Principles of High Resolution NMR Spectroscopy in Solids*, 2nd ed., Springer-Verlag, Berlin/New York, **1983**, pp 14

60 Rose, M.E. *Elementary Theory of Angular Momentum*, 5th ed.; John Wiley & Sons: Chicester, U.K., **1967**; p. 76.

61 Shönborn, F.; Schmitt, H.; Zimmerman, H.; Haeberlen, U.; Corminboeuf, C.; Groffmann, G.; Heine, T. *J. Magn. Reson.*, **2005**, *175*, 52.

62 (a) Sefzik, T.; Turco, D.; Iuliucci, R. J.; Facelli, J. C. *J. Phys. Chem. A*, **2005**, *109*, 1180-1187; (b) Sefzik, T. H.; Fidler, J. M.; Iuliucci, R. J.; Facelli, J. C. *Magn. Reson. Chem*. **2006**, *44*, 390-400.

63 Iuliucci, R. J.; Clawson, J.; Hu, J. Z.; Solum, M. S.; Barich, D. H.; Grant, D. M.; Taylor, C. M. *Solid State Nucl. Magn. Reson.* **2003**, *24*, 23-38.

64 Iuliucci, R. J.; Phung, C. G.; Facelli, J. C.; Grant, D. M. *J. Am. Chem. Soc*. **1998**, *120*, 9305.

65 Iuliucci, R. J.; Phung, C. G.; Facelli, J. C.; Grant, D. M. *J. Am. Chem. Soc.* **1996**, *118*, 4880.

66 Iuliucci, R. J.; Alderman, D. W.; Facelli, J. C.; Grant, D. M. *J. Am. Chem. Soc.* **1995**, *117*, 2336.

67 Cook, R. L.; de Lucia, F. C. *Amer. J. Phys.* **1971**, *39*, 1433.

68 Mason, J. *Solid State NMR* **1992**, *2*, 285-288.

69 Harris, R. K.; Becker, E. D.; Cabral de Menezes, S. M.; Granger, P.; Hoffman, R. E.; Zilm, K. W. *Pure Appl. Chem.* **2008**, *80*, 59.

70 Carter, C. M.; Facelli, J. C.; Alderman, D. W.; Grant, D. M.; Dalley, N. K.; Wilson, B. E. *J. Chem. Soc., Far. Trans. 1* **1988**, *84(11)*, 3673.

71 Liu, F.; Phung, C. G.; Alderman, D. W.; Grant, D. M. *J. Magn. Reson.* **1996** *A 120* , 231.

72 Harris, R. K.; Becker, E. D.; Cabral de Menezes, S.; Goodfellow, R.; Granger, P. *Pure Appl. Chem.* **2001**, *73*, 1795.

73 Christopher, E. A.; Harris, R. K.; Fletton, R. A. *Solid State NMR* **1992**, *1*, 93.

74 Osawa, E. *Kagaku*, **1970**, *25*, 854-863.

75 Kroto, H. W.; Heath, J. R.; O'Brien, S. C.; Curl, R. F.; Smalley, R. E. *Nature* **1985**, *318*, 162-163.

76 Rohlfing, E. A.; Cox, D. M.; Kaldor, A. *J. Chem. Phys*. **1984**, *81*, 3322-3330.

77 Krätschmer, W.; Lamb, L. D.; Fostiropoulos, K.; Huffman, D. *Nature* **1990**, *347*, 354-358.

78 (a) Daly, T. K.; Buseck, P. R.; Williams, P.; Lewis, C. F. *Science* **1993**, *259*, 1599-1601; (b) Buseck, P. R. *Earth and Planetary Science Letters* **2002**, *203*, 781-792.

79 (a) Heyman, D. *Carbon* **1995**, *33*, 237-239; (b) Gu, Y.; Wilson, M. A.; Fisher, K. J.; Dance, I. G.; Willett, G. D.; Ren, D.; Volkova, I. B. *Carbon* **1995**, *33*, 862-863.

80 Markovic, Z.; Trajkovic, V. *Biomaterials*. **2008**, *29*, 3561-3573.

81 Sathish, M.; Miyazawa, K.; Hill, J.; Ariga, K. *J. Am. Chem. Soc*. **2009**, *131*, 6372-6373.

82 Ma, H.; Liu, M. S.; Jen, A. K-Y. *Polym. Int*. **2009**, *58*, 594-619.

83 Grausova, L.; Vacik, J.; Vorlicek, V.; Svoricik, V.; Slepicka, P.; Bilkova, P.; Vandrovcova, M.; Lisa, V.; Bacakova, L. *Diamond and Related Materials*. **2009**, *18*, 578-586.

84 Levi, N.; Hantgan, R. R.; Lively, M. O.; Carroll, D. L.; Prasad, G. L. *J. Nanobiotechnology*. **2006**, *4*, 14.

85 Martin, R.; Wang, H-L.; Gao, J.; Iyer, S.; Montano, A. G.; Martinez, J.; Shreve, P. A.; Bao, Y.; Wang, C-C.; Chang, Z.; Gao, Y.; Iyer, R. *Tox. Appl. Pharmac*. **2009**, *234*, 58-67.

86 (a) Becker, L.; Poreda, R. J.; Bada, J. L. *Science* **1996**, *272*, 249-252; (b) Becker, L.; Poreda, R. J.; Hunt, A. G.; Bunch, T. E.; Rampino, M. *Science* **2001**, *291*, 1530-1533.

87 Kortan, A. R.; Kipylov, N.; Glarum, S. H.; Gyorgy, E. M.; Ramirez, A. P.; Fleming, R. M.; Thiel, F. M.; Hadden, R. C. *Nature* **1992**, *355*, 529-532.

88 Forro, L.; Mihaly, L. *Rep. Prog. Phys.* **2001**, *64*, 649-699.

89 Orendt, A. M. In *Encyclopedia of NMR*; D. M. Grant and R. K. Harris, Eds.; John Wiley & Sons: London, **2002**, pp 551-558.

90 (a) Carter, C. M.; Alderman, D. W.; Facelli, J. C.; Grant, D. M. *J. Am. Chem. Soc*. **1987**, *109*, 2639-2644; (b) Sherwood, M. H.; Facelli, J. C.; Alderman, D. W.; Grant, D. M. *J. Am. Chem. Soc*. **1991**, *113*, 750-753; (c) Iuliucci, R. J.; Facelli, J. C.; Alderman, D. W.; Grant, D. M. *J. Am. Chem. Soc*. **1995**, *117*, 2336-2343; (d) Iuliucci, R. J.; Phung, C. G.; Facelli, J. C.; Grant, D. M. *J. Am. Chem. Soc*. **1996**, *118*, 4880-4888; (e) Iuliucci, R. J.; Phung, C. G.; Facelli, J. C.; Grant, D. M. *J. Am. Chem. Soc*. **1998**, *120*, 9305-9311.

91 Orendt, A. M.; Facelli, J. C.; Bai, S.; Rai, A.; Gossett, M.; Scott, L. T.; Boerio-Goates, J.; Pugmire, R. J.; Grant, D. M. *J. Phys. Chem. A* **2000**, *104*, 149-155.

92 (a) Barich, D. H.; Orendt, A. M.; Pugmire, R. J.; Grant, D. M. *J. Phys. Chem. A* **2000**, *104*, 8290-8295; (b) Barich, D. H.; Hu, J. Z.; Pugmire, R. J.; Grant, D. M. *J. Phys. Chem. A* **2002**, *106*, 6477-6482.

93 Tycko, R.; Dabbagh, G.; Fleming, R. M.; Haddon, R. C.; Makhija, A. V.; Zahurak, S. M. *Phys. Rev. Lett*. **1991**, *67*, 1886-1889.

94 Yannoni, C. S.; Johnson, R. D.; Meijer, G.; Bethune, D. S.; Salem, J. R. *J. Phys. Chem*. **1991**, *95*, 9-10.

95 Haddon, R. C. *J. Am. Chem. Soc.* **1987**, *109*, 1676-1685.

96 Haddon, R. C.; Scott, L. T. *Pure & Appl. Chem*. **1986**, *58*, 137-142.

97 (a) Haddon, R. C. *Science* **1993**, *261*, 1545-1550; (b) Haddon, R. C. *J. Am. Chem. Soc.* **1997**, *119*, 1797-1798.

98 Haddon, R. C. *J. Am. Chem. Soc*. **1990**, *112*, 3385-3389.

99 Dinadayalane, T. C.; Sastry, G. N. *Tetrahedron* **2003**, *59*, 8347-8351.

100 (a) Hanson, J. C.; Nordman, C. E. *Acta Crystallogr. B*. **1976**, *32*, 1147-1153; (b) Petrukhina, M. A.; Andreini, K. W.; Mack, J.; Scott, L. T. *J. Org. Chem*. **2005**, *70*, 5713-5716.

101 Sakurai, H.; Daiko, T.; Hirao, T. *Science* **2003**, *301*, 1878.

102 Sakurai, H.; Daiko, T.; Sakane, H.; Amaya, T.; Hirao, T. *J. Am. Chem. Soc.* **2005**, *127*, 11580-11581.

103 Wegner, H. A.; Scott, L. T.; de Meijere, A. *J. Org. Chem.* **2003**, *68*, 883-887.

104 The X-ray crystal structure of indenofluoranthene has been deposited with the CCDC (number 760581).

105 Hartmann, S. R.; Hahn, E. L. *Phys. Rev*. **1962**, *128*, 2042-2053.

106 Grant, D. M.; Liu, F.; Iuliucci, R. J.; Phung, C. G.; Facelli, J. C.; Alderman, D. W. *Acta Crystallogr.* **1995**, *B51*, 540-546.

107 Facelli, J. C. *Concepts Magn. Reson.* **2004**, *20A*, 42-69.

108 Becke, A. D. *Phys. Re*v. *A* **1988**, *38*, 3098-3100.

109 Becke, A. D. *J. Chem. Phys.* **1993**, *98*, 5648-5652.

110 Cheeseman, J. R.; Trucks, G. W.; Keith, T. A.; Frisch, M. J. *J. Chem. Phys.* **1996**, *104*, 5497-5509.

111 Wiberg, K. B.; Hammer, J. D.; Zilm, K. W.; Cheeseman, J. R. *J. Org. Chem.* **1999**, *64*, 6394-6400.

112 McLean, A. D.; Chandler, G. S. *J. Chem. Phys.* **1980**, *72*, 5639-5648.

113 Krishnan, R.; Binkley, J. S.; Seeger, R.; Pople, J. A. *J. Chem. Phys.* **1980**, *72*, 650-654.

114 Ditchfield, R. *J. Chem. Phys.* **1972**, *56*, 5688-5691.

115 Pulay, P.; Hinton, J. F. In *Encyclopedia of NMR*; D. M. Grant and R. K. Harris, Eds.; John Wiley & Sons: London, **1996**, pp 4334-4339.

116 Grant, D. M.; Halling, M. D. *Concepts Magn. Reson. A*. **2009**, *34*, 217-237.

117 Wudl, F.; Smith, G. M.; Hufnagel, E. J. *J. Chem. Soc., Chem. Commun.* **1970**, 1453-1454.

118 Coffen, D. L.; Chambers, J. Q.; Williams, D. R.; Garrett, P. E.; Canfield, N. D. *J. Am. Chem. Soc.* **1971**, *93*, 2258-2268.

119 Wudl, F. *J. Am. Chem. Soc.* **1975**, *97*, 1962-1963.

120 Khodorkovsky, V.; Shapiro, L.; Krief, P.; Shames, A.; Mabon, G.; Gorgues, A.; Giffard, M. *Chem. Commun*., **2001**, *24*, 2736-2737.

121 Garcia-Yoldi, I.; Miller, J. S.; Novoa, J. J. *J. Phys. Chem. A,* **2009**, *113*, 484-492.

122 Benz, M. E.; Tabakovic, I.; Millar, L. L. *Chem. Mater*. **1994**, *6*, 351-352.

123 (a) Yakushi, K.; Nishimura, S.; Sugano, T.; Kuroda, H.; Ikemoto, I. *Acta Crystallogr. B* **1980**, *36*, 358-363. (b) Sugano, T.; Kuroda, H.; Yakushi, K. *Bull. Chem. Soc. Jpn*. **1978**, *51*, 1041-1046.

124 Bondi, A. *J. Phys. Chem.* **1964**, *68*, 441-451.

125 Dixon, D. A.; Miller, J. S. *J. Am. Chem. Soc.* **1987**, *109*, 3656-3664.

126 (a) Del Sesto, R. E.; Miller, J. S.; Novoa, J. J.; Lafuente, P. *Chem. Eur. J.* **2002**, *8*, 4894-4908 . (b) Miller, J. S.; Novoa, J. J. *Acc. Chem. Res* **2007**, *40*, 189-196.

127 Strohmeier, M.; Barich, D. H.; Grant, D. M.; Miller, J. S.; Pugmire, R. J.; Simons, J. *J. Phys. Chem. A* **2006**, *110*, 7962-7969.

128 *Modeling NMR Chemical-shifts*; Facelli, J. C., De Dios, A. C., Eds.; ACS symposium Series Vol 732; American Chemical Society: Washington, DC, 1999.

129 Havlin, R.; McMahon, M.; Srinivasan, R.; Le, H.; Oldfield, E. *J. Phys. Chem. A* **1997**, *101*, 8908-8913.

130 Wallraff, G. M. Disseration, University of Utah 1985.

131 Bernard, G. M.; Wasylishen, R. E.; Phillips, A. D. *J. Phys. Chem. A* **2000**, *104*, 8131-8141.

132 Miyajima, S.; Chiba, T.; Saito, G.; Inokuchi, H. *J. Phys. Chem*. **1995**, *99*, 1582-1586.

133 Duncan, T. M. *A Compilation of Chemical-shift Anisotropies*, 2nd ed.; The Farragut Press: Chicago, IL, **1997**.

134 Facelli, J. C.; Grant, D. M. *Theor. Chim. Acta* **1987**, *71*, 277-288.

135 Beeler, A. J.; Orendt, A. M.; Grant, D. M.; Cutts, P. W.; Michl, J.; Zilm, K. W.; Downing, J. W.; Facelli, J. C.; Schindler, M. S.; Kutzelnigg, W. *J. Am. Chem. Soc.* **1984**, *106*, 7672-7676.

136 Sherwood, M. H.; Facelli, J. C.; Alderman, D. W.; Grant, D. M. *J. Am. Chem. Soc.* **1991**, *113*, 750.

137 Augspurger, J.; Pearson, J. G.; Oldfield, E.; Dykstra, C. E.; Park, K. D.; Schwartz, D. *J. Magn. Reson.* **1992**, *100*, 342-357.

138 Asakawa, N.; Kuroki, S.; Kurosu, H.; Ando, I.; Shoji, A.; Ozaki, T. *J. Am. Chem. Soc.* **1992**, *114*, 3261-3265.

139 Gu, Z.; Zambrano, R.; McDermott, A. *J. Am. Chem. Soc.* **1994**, *116*, 6368-6372.

140 Soderquist, A.; Facelli, J. C.; Horton, W. J.; Grant, D. M. *J. Am. Chem. Soc.* **1995**, *117*, 8441-8446.

141 Stueber, D.; Guenneau, F. N.; Grant, D. M. *J. Chem. Phys*. **2001**, *114*, 9236-9243.

142 Reed, A. E.; Weinhold, F. *J. Chem. Phys*. **1983**, *78*, 4066-4073.

143 Reed, A. E.; Weinstock, R. B.; Weinhold, F. *J. Chem. Phys*. **1985**, *83*, 735-746.

144 Brandon, E. J.; Rittenberg, D. K.; Arif, A. M.; Miller, J. S. *Inorg. Chem.* **1998**, *37*, 3376-3384.

145 Pines, A.; Gibby, M. G.; and Waugh, J. S. *J. Chem. Phys.* **1973**, *59*, 569-590.

146 Schaefer, J.; Stejskal, E. O. *J. Am. Chem. Soc*. **1976**, *98*, 1031-1032.

147 Lee, C.; Yang, W.; Parr, R. G. *Phys. Rev. B* **1988**, *37*, 785–789.

148 Perdew, J. P. In *Electronic Structure of Solids '91*, Ziesche, P., Eschrig, H. Eds. Akademie Verlag: Berlin, GER, 1991; p. 11.

149 Dunning, T. H., Jr. *J. Chem. Phys.* **1989**, *90*, 1007–1023.

150 Wachters, A. J. H. *J. Chem. Phys.* **1970**, *52***,** 1033.

151 Hay, P. J. *J. Chem. Phys.* **1977**, *66***,** 4377-84.

152 London, F. *J. Phys. Radium* **1937**, *8*, 397.

153 Wolinski, K.; Hinton, J. F.; Pulay, P. *J. Am. Chem. Soc.* **1990**, *112*, 8251–8260.

154 NBO Version 3.1, E. D. Glendening, A. E. Reed, J. E. Carpenter, and F. Weinhold.

155 Garcia, P.; Dahaoui, S.; Katan, C.; Souhassou, M.; Lecomte, C. *Faraday Discuss*. **2007**, *135*, 217-235.

156 Stueber, D. *Concepts Magn. Reson*. **2006**, *28A*, 347-368.

157 Harper, J. K. In *Encyclopedia of NMR*; Grant, D. M., Harris, R. K., Eds.; John Wiley: Chichester, UK, **2002**; Vol. 9, pp 589-597.

158 Maruta, G.; Takeda, S.; Yamaguchi, K.; Ueda, K.; Sugimoto, T. *Synth. Met.* **1999**, *103*, 2333-2334.

159 Heise, H.; Köhler, F. H.; Herker, M.; Hiller, W. *J. Am. Chem. Soc.* **2002**, *124*, 10823-10832.

160 Facelli, J. C.; Grant, D. M. In *Topics in Stereochemistry*; Eliel, E. L., Wilen, S. H., Eds.; John Wiley & Sons: New York, 1989; Vol. 19, pp 1-61.

161 Wiberg, K. B. *Tetrahedron* **1968**, *24*, 1083-1096.

162 Buhl, M.; Hirsch, A. *Chem. Rev*. **2001**, *101*, 1153-1184.

163 Braun, T.; Schubert, A. P.; Kostoff, R. N. *Chem. Rev*. **2000**, *100*, 23-38.

164 Chen, Z.; King, R. B. *Chem. Rev*. **2005**, *105*, 3613-3642.

165 Halling, M. D.; Orendt, A. M.; Strohmeier, M.; Solum, M. S.; Tsefrikas, V. M.; Hirao, T.; Scott, L. T.; Pugmire, R. J.; Grant, D. M. *Phys. Chem. Chem. Phys.* **2010**, *12*, 7934-7941.

166 Dobrowolski, M. A.; Cyranski, M. K.; Merner, B. L.; Bodwell, G. J.; Wu, J. I.; Schleyer, P. v R. *J. Org. Chem*. **2008**, *73*, 8001-8009.

167 Bodwell, G. J.; Miller, D. O.; Vermeij, R. J. *Org. Lett*. **2001**, *3*, 2093-2096.

168 Aprahamian, I.; Bodwell, G. J.; Fleming, J. J.; Manning, G. P.; Mannion, M. R.; Merner, B. L.; Sheradsky, T.; Vermeij, R. J.; Rabinovitz, M. *J. Am. Chem. Soc*. **2004**, *126*, 6765-6775.

169 Bodwell, G. J.; Fleming, J. J.; Mannion, M. R.; Miller, D. O. *J. Org. Chem*. **2000**, *65*, 5360-5370.

170 Lonsdale, K.; Milledge, H. J.; Krishna Rao, K. V. *Proc. R. Soc. London, Ser. A*. **1960**, *255*, 82.

171 Caramori, G. F.; Galembeck, S. E.; Laali, K. K. *J. Org. Chem*. **2005**, *70*, 3242-3250.

172 Bodwell, G. J.; Bridson, J. N.; Houghton, T. J.; Kennedy, J. W. J.; Mannion, M. R. *Angew. Chem. Int. Ed. Engl*. **1996**, *35*, 1320-1321.

173 Facelli, J. C.; Nakagawa, B. K.; Orendt, A. M.; Pugmire, R. J. *J. Phys. Chem. A* **2001**, *105*, 7468-7472.